



HAVERFORD  
COLLEGE

DEPARTMENT OF PHYSICS AND ASTRONOMY

SENIOR THESIS

---

**A Spectral Analysis of Red and Blue  
Quasars and their Effect on Galactic  
Evolution**

---

*Author:*

Rachel Langgin

Advised by Eilat Glikman

4th May 2023

---

# Contents

<b>List of Figures</b>	<b>iii</b>
<b>List of Tables</b>	<b>viii</b>
<b>1 Introduction &amp; Motivation</b>	<b>2</b>
1.1 Background . . . . .	2
1.1.1 Redshift and the Expanding Universe . . . . .	2
1.1.2 Strange Nuclear Emission in Galaxies . . . . .	5
1.1.3 The Discovery of Quasars . . . . .	6
1.1.4 Accretion Properties . . . . .	9
1.1.5 Emission Properties . . . . .	12
1.1.6 Active Galactic Nuclei and Galaxy Formation in the Dusty Universe . . . . .	14
1.1.7 Quasar Demographics and Colors . . . . .	19
1.2 Plan For this Thesis . . . . .	24
<b>2 Sample Selection</b>	<b>25</b>
2.1 Radio Selection with FIRST . . . . .	27
2.2 Infrared Selection with WISE . . . . .	28
2.3 Near-Infrared Selection with UKIDSS . . . . .	29
2.4 Optical Selection with SDSS . . . . .	30
<b>3 QSOs in SDSS</b>	<b>31</b>
3.1 Erroneous Redshifts . . . . .	33
<b>4 Dust Reddening Investigation</b>	<b>34</b>
4.1 BADASS: Removal of Host-Galaxy Emission . . . . .	35
4.2 Red Quasars in the Blue Selected Sample . . . . .	41

---

<b>5 Discussion: Red Quasars in the Context of Blue Quasars</b>	<b>42</b>
5.1 Red and Blue Quasars as a Function of Luminosity . . . . .	42
5.2 Red and Blue Quasars as a Function of Redshift . . . . .	43
<b>6 Initial Results and Further Investigations</b>	<b>48</b>
<b>7 Acknowledgments</b>	<b>51</b>
<b>8 Facilities</b>	<b>52</b>
<b>A Matching in SDSS</b>	<b>53</b>
<b>B BADASS: Computationally Expensive</b>	<b>53</b>
<b>C K-Band Magnitude vs absolute <math>22\mu\text{m}</math> (W4) Magnitude</b>	<b>53</b>

---

## List of Figures

- 1 An illustration from Pettini (2011) of the quasar absorption line technique used to probe the distant Universe. Encoded in the absorption spectrum of a distant quasar is information on the physical properties of gas and galaxies located in the path of the light rays from the quasar to Earth. Shown is the emission lines from the quasar that are broadened and peak upwards. . . . . 4
- 2 Hubble’s Velocity vs. Distance figure of galaxies Hubble 1929. The correlation between faster moving galaxies (known as “extra-galactic nebulae” at-the-time) measured at a higher distances suggested all cosmological objects are constantly moving away from us—the expansion of the Universe. . . . . 5
- 3 This image from Hubble’s Wide Field and Planetary Camera 2 (WFPC2) is known as the best of ancient and brilliant quasar 3C 273, which resides in a giant elliptical galaxy in the constellation of Virgo. Its light has taken about 2.5 billion years to reach us. Despite this great distance, it is still one of the closest quasars to Earth. It was the first quasar ever to be identified by Schmidt, and was discovered in the early 1960s by astronomer Allan Sandage. Credit: ESA/Hubble & NASA . . . . . 7
- 4 Sloan Digital Sky Survey (SDSS) Spectra for a typical star (panel 1), galaxy (panel 2), and quasar (panel 3). The broad absorption lines have been analyzed to indicate the quasar spectrum to be different from the similar star spectrum. In panel 1, the stellar spectrum is filled with absorption lines at particular colors or wavelengths following a power-law continuum. The galactic spectrum in panel 2 displays a composite of absorption and emission lines, while the quasar spectrum in panel 3 shows classic broad emission lines that have been shifted due to the Doppler effect. These images are not shown to scale as the we are comparing the power-law continuum shape and differences in emission/absorption lines of each spectrum. . . . . 8
- 5 In this Hubble image, the blue jet contrasts with the yellow glow from the combined light of billions of unresolved stars and the center black hole, in M87. The jet is a black-hole-powered stream of material that is being ejected from M87’s BH core. Credits: NASA and the Hubble Heritage Team (STScI/AURA) . . . . . 14

---

6	The Unified AGN Model illustration created by Emma Alexander adapted from Becker et al. (1995). The black lines label different properties of the AGN previously discussed, while the thick arrows represent different viewing angles, and the observed object which results from them. Note the asymmetry of the diagram; this is to demonstrate the two different possibilities of radio loud/quiet and is not representative of a single object and further, AGN types depend largely on the viewing angle (Urry and Padovani 1995). . . . .	17
7	Distinction between Type 1 Red QSOs and Type 1 Blue QSOs following Figure 3. from Glikman et al. 2022. The Red Type-1 QSO has a ‘torus’ of dust surrounding that intrinsically reddens the underlying quasar. . . . .	20
8	An artist’s impression of the transition from red to blue quasars. Notice the heavy dust enshrouding the middle red quasar. Credits: Gemini Observatory, GMOS-South, NSF; <a href="https://www.pxwall.com/4k-high-definition-galaxy-wallpaper/">https://www.pxwall.com/4k-high-definition-galaxy-wallpaper/</a> ; Adapted by S. Munro . . . . .	20
9	Comparison of the best-fit star formation history (thick solid curve) with the massive black hole accretion history from X-ray [red curve (Madau and Dickinson 2014); light green shading (Aird et al. 2010)] and infrared (light blue shading) (Delvecchio et al. 2014) data. The shading indicates the $\pm 1\sigma$ uncertainty range on the total bolometric luminosity density. . . . .	21
10	Figure 15 from Glikman et al. (2012) showing the dereddened K-band absolute magnitude as a function of redshift. The colors of the circles correspond to the amount of extinction, ranging from low extinction (yellow) to heavily reddened (red). The dotted lines indicate the survey limit ( $K < 16$ ) for increasing amounts of extinction. The small dots are FBQS-II and FBQS-III quasars, which they assume are unabsorbed. At every redshift, red quasars are the most luminous. . . . .	22

---

11	<p>Figure 12 from Glikman et al. (2022) showing examples of two QSO spectra whose host galaxies were fitted with GANDALF (Graphical Astrophysics code for N-body Dynamics And Lagrangian Fluids; Hubber and Rosotti 2016) and subtracted to improve the QSO template fitting process and better estimate the reddening, parameterized by <math>E(B - V)</math>, experienced by the QSO. The top panel in each column is the original, poor, fit. The black line is the original spectrum. The red line is the best-fit, reddened QSO template and the cyan line is the unreddened QSO template. The middle row shows the fits produced by GANDALF, with the host-galaxy spectrum shown in green, atop the original spectrum in black. The bottom panel shows the galaxy-subtracted spectrum in black and the newly best-fitted reddened QSO template in red. In both examples host-galaxy emission results in artificially large extinctions. We expect similar results in our own sample since subtracting the host-galaxy empirically exposes predominantly unreddened QSOs. . . . .</p>	24
12	<p>Flowchart summarizing the sample selection for this thesis research project. . . . .</p>	27
13	<p>Glikman et al. (2022) reproduced Figure 12 from Wright et al. (2010) showing the location of various astrophysical objects in WISE color-color space. Over-plotted is a box that outlines the initial selection region with thick purple solid lines and plots within the box sources with SDSS spectra identified as QSO (blue circles) and GALAXY (orange circles). Also plotted are the selected red-quasar candidates with large outlined circles. Newly confirmed QSOs are filled red and sources that are not obviously QSOs are filled green. The black solid line shows our refined color cuts selection criterion that avoids significant contamination from non-QSOs (2). . . . .</p>	29
14	<p>The <math>v_{FWHM}</math> distribution of our sample sources. The red dashed line at <math>v_{FWHM} = 1000 \text{ km s}^{-1}</math> marks required criteria for a Type 1, broad line QSO. . . . .</p>	32
15	<p>Broad line (Type I) QSO sample selection process. . . . .</p>	33
16	<p>Redshift (<math>z</math>) Full Sample Distribution (blue) with Type I (red) sources we include and the narrow-line sources we eliminate from the sample (green). We implement our redshift cutoff, of <math>z &lt; 3.5</math>. . . . .</p>	34

---

---

17	Distribution of the initial $E(B-V)$ values for the SDSS QSOs, which we determined by fitting a QSO template to each spectrum are shown in the blue for the entire sample. The vertical red dashed line at $E(B-V) = 0.25$ is our defined limit for a QSO to be considered dust-reddened. As shown, there extends a significant tail of reddened QSOs which we investigate further in Section 4.2. The distribution of initial $E(B-V)$ values below this reddened limit is however already centered on $E(B-V) = 0$ shown in dark blue and fitted with a black Gaussian curve. The mean, centered at $E(B-V) = 0.109$ , is shown in the black dashed line. . . . .	35
18	Example SDSS spectra of a high redshift ( $z > 0.7$ ) source with $E(B-V) \sim 0.0$ . Each spectra is well-fit by a QSO template shown in red. . . . .	36
19	Distribution of the initial $E(B-V)$ values for the SDSS QSOs, which we determined by fitting a QSO template to each spectrum are shown in the red for the entire sample. We further split the sample by high and low redshift. The distribution of initial $E(B-V)$ values for high redshift SDSS QSOs is already centered on $E(B-V) = 0$ shown in blue and fitted with a gray Gaussian curve. The vertical red dashed line at $E(B-V) = 0.25$ is our defined limit for a QSO to be considered dust-reddened. As shown by the orange distribution and orange Gaussian curved fitted to the initial incorrect $E(B-V)$ values for low redshift SDSS QSOs they consist of much higher reddening values centered at $E(B-V) = 0.26$ . These sources are predominantly responsible for the excess reddening tail and require host-galaxy subtraction from their spectra. . . . .	37
20	This figure shows the data, model, residuals, and best-fit components, to visually ascertain the quality of the fit to SDSS object (0.6050577, 0.30628625) with a redshift, $z = 0.6050577$ . The red line shown is the model fit to the QSO spectrum, the green line is the host-galaxy/stellar component fit, and other line-fitting components can be seen in the legend. . . . .	39
21	We follow Section 2.3 from Glikman et al. (2022) and subtract the host-galaxy's fit (green) from the model fit (red) to remove the host-galaxy's emission from the spectra. The red highlight is the best-fit QSO template from which $E(B-V)$ is derived to both the SDSS data and the removed host-galaxy data fit. This leaves behind the sought-after unobscured blue QSO now that we have accounted for reddening.	40

---

---

22	Distribution of the initial $E(B-V)$ values for the SDSS QSOs, which we determined by fitting a QSO template to each spectrum are shown in the red for the entire sample. The vertical red dashed line at $E(B-V) = 0.25$ is our defined limit for a QSO to be considered dust-reddened. As shown by the orange distribution and orange Gaussian curved fitted to the initial incorrect $E(B-V)$ values for low redshift SDSS QSOs centered at $E(B-V) = 0.26$ is then shifted to the blue centered at $E(B-V) = 0.10$ . . . . .	41
23	Distribution of the initial $E(B-V)$ values for the SDSS QSOs, which we determined by fitting a QSO template to each spectrum are shown in the red for the entire sample. We further split the sample by high and low redshift. The distribution of initial $E(B-V)$ values for high redshift SDSS QSOs is already centered on $E(B-V) = 0$ shown in blue and fitted with a gray Gaussian curve. The vertical red dashed line at $E(B-V) = 0.25$ is our defined limit for a QSO to be considered dust-reddened. As shown by the orange distribution and orange Gaussian curved fitted to the initial incorrect $E(B-V)$ values for low redshift SDSS QSOs centered at $E(B-V) = 0.26$ is then shifted to the blue centered at $E(B-V) = 0.10$ . . . . .	42
24	We follow Section 2.3 from Glikman et al. (2022) and subtract the host-galaxy's fit (green) from the model fit (red) to remove the host-galaxy's emission from the spectra. The high reddening does not change after the host is subtracted from the data—leaving the dust-reddened quasar. We add these sources to the reddened QSO sample to investigate in Section 5. . . . .	44
25	Example SDSS spectra of a high redshift ( $z > 0.7$ ) source with $E(B-V) > 0.25$ , where the under each spectrum the $E(B-V)$ value measured from the data is shown on the left in red and the $E(B-V)$ value measured from the QSO template fit to the data is shown on the right in red. Since there is no galaxy subtraction, both values are inherently the same just cross-checked for sanity purposes. . . . .	45

---

26	Our entire sample’s optical-to-near-infrared colors used in the KX selection method defined by Warren et al. (2000) and re- fined by Maddox et al. (2008). The blue circles represent all blue sources with $E(B-V) < 0.25$ , while the red circles represent all reddened sources with $E(B - V) > 0.25$ . The sources marked with an ‘x’ have had their host-galaxy subtracted from them. The gray triangle represent spectra that were not able to have their extinction value measured. The red dashed line is our color cut we impose in Equation 29 in this space to separate the red QSOs from the blue QSOs. . . . .	46
27	Our Type 1 sample’s redshift distribution against K-magnitude where 12 is brighter and 17 is fainter. The blue circles represent all blue sources with $E(B - V) < 0.25$ , while the red circles represent all reddened sources with $E(B - V) > 0.25$ . The sources marked with an ‘x’ have had their host-galaxy subtracted from them. The gray triangle represent spectra that were not able to have their extinction value measured. Red QSOs that have had their host-galaxy subtracted (red circles with an ‘x’) require further investigation. . . . .	47
28	The absolute K-band magnitude from WISE versus absolute 22m (W4) magnitude from UKIDSS for the QSO sample. The blue circles represent the blue QSOs found in our sample, the red circles represent the reddened QSOs found in our sample, the ‘x’s mark sources which have had their host-galaxy subtracted, and the grey triangles represent sources that which the Extinction code failed on. A direct relationship is seen across the luminosity range, except at the highest luminosities where the K-band magnitudes are slightly enhanced compared with W4. Interestingly, the failed spectra are entirely offset from the rest of the sample. . . . .	54

## List of Tables

1	Fifteen low-redshift ( $z < 0.7$ ) QSOs for which we subtracted the host-galaxy’s light from the spectrum are shown in the Table. The name, redshift, RA, DEC, and E(B-V) Before and After values are shown in their respective columns. The change in E(B-V) values is given in the last column where the negative sign indicates that all of these QSOs E(B-V) values were unreddened and “blueshifted” towards the center at $E(B - V) \sim 0.1$ . This is only a portion of the table. A full version containing all 1179 sources is available upon request. . . . .	43
---	--	----

---

## Abstract

Growing supermassive black holes (SMBHs) are identified as active galactic nuclei (AGN) and, when most luminous, as quasi-stellar objects or quasars. Emanating from very compact regions at the center of galaxies, their spectra contains broad emission lines encoding information from the distant Universe. A relative newly discovered and largely unexplored population of sources that may help resolve the nature of SMBHs and galactic energy exchange, are dust-reddened quasars which appear to represent an important evolutionary phase linking galaxy mergers to black hole growth. Since red quasars can be elusive, early AGN works on red quasars had to construct surveys using advanced radio selection techniques to avoid contamination from other stars and galaxies. Through a spectroscopic analysis, this project probes a radio, mid-infrared, and optically selected sample of unobscured, blue quasars so that the dust-reddened, red quasars can be put in context. We find from a low redshift sample of AGN ( $z < 0.7$ ), removing the host-galaxy light from the spectra results in a spectrum with little reddening ( $E(B - V)_{After} < 0.25$ ) in 68% (N=211) of our sample and the red QSO fraction ( $E(B - V)_{After} > 0.25$ ) to be 32% (N=98). At lower redshifts, the effect of reddening is weaker and we identify heavily reddened sources with intrinsic luminosities consistent with their blue QSO counterparts. There are few, 3.6% (N=32), sources that are at high redshift ( $z > 0.7$ ) and have  $E(B - V) > 0.25$ , lying in the tail of the reddening distribution. There is a scarcity of red QSOs at high redshifts ( $z > 1.0$ ). With this in mind, we also consider comparisons between red and blue QSOs restricted to  $z > 1.0$ , which amounts to 98% (N=673) blue sources and 2% (N=15) red sources. This trend is well-explained by the fact that higher-redshift sources with even moderate amounts of reddening must be more luminous in order to pass the selection criteria. Although the red QSO sample is otherwise predominantly low redshift ( $z < 1.0$ ), higher-redshift red QSOs appear to make up a higher fraction of the red QSOs than in the blue population. This could point to a genuine evolutionary explanation.

---

# 1 Introduction & Motivation

Astrophysics is a dance between theoretical interpretations and observations. An arrangement of infinite possibilities of space, constrained by time, and limited by what we can physically see situates this scientific branch in a balancing act. Astrophysicists therefore must balance the realistic possibilities of our Universe to the unpredictability of nature. From the early histories of Australian Aborigines, to 1609 when Galileo Galilei pointed his telescope at the skies, to revolutionizing astronomers such as, Henrietta Swan Leavitt and Edwin Hubble, astrophysics has advanced in tandem with the human understanding of our world and cosmos. Technological advances in the early 21st century have placed this science in the midst of a renaissance. Terrestrial observatories such as the Event Horizon Telescope (EHT; Event Horizon Telescope Collaboration et al. 2019), a global network of synchronized radio observatories capturing images of black holes, and the Laser Interferometer Gravitational-Wave Observatory (LIGO; Abbott et al. 2016), consisting of two large facilities in two locations across the United States detecting Gravitational Waves, have provided astronomers with a glimpse into the previously unseen physics behind some of the most destructive objects in our universe. Furthermore, living in the era of the James Webb Space Telescope (JWST; Rigby et al. 2022) offers an improved window into the electromagnetic spectrum, revealing high-resolution images of the Universe in the infrared. Despite the large-scale research and increase in funding in Astrophysics over the past decades (Council 2000; Seth et al. 2009), our current understandings of the evolutionary relationship between the building blocks of our Universe, galaxies, and their nuclear SMBHs remains unsolved.

In this thesis we construct a rigorous sample of active SMBH to complete a spectroscopic analysis, to measure the characteristics of an unobscured, blue quasars so that the dust-reddened, red quasars can be put in context. We shed light on the evolutionary connection between the dust-reddened SMBHs and their host-galaxies. We also point to a follow-up investigation of the radio properties and morphologies of our selected sample to possibly account for the excess reddening.

## 1.1 Background

### 1.1.1 Redshift and the Expanding Universe

In the early twentieth century, American astronomer Henrietta Swan Leavitt discovered the period-luminosity law that enabled astronomers to estimate the distance from the Earth to stars based on their brightness (Leavitt and Pickering 1912). Leavitt is known for discovering 2,400 variable stars in her lifetime and for finding that some of these stars have a predictable brightness over

---

time. These so-called Cepheid variables are thus a good method for measuring astronomical distances. Later, in 1924 American astronomer Edwin Powell Hubble transformed astronomy through measuring a Cepheid variable star in what was known as a small fuzzy “spiral nebulae”. Hubble demonstrated this patch of light turned out to be an entire galaxy<sup>1</sup>, composed of hundreds of billions of stars like our own (Hubble 1925). With the largest telescope of the time, the 100-inch telescope at California’s Mount Wilson Observatory, Hubble was able to re-examine the relationship between distances and observed velocities of the most luminous types of stars that could be recognized in the distant galaxies (Hubble 1929).

Twelve years prior, in 1912 Vesto M. Slipher observed the emission or absorption features in a galaxy’s spectrum (Slipher 1913). An object’s spectrum can be observed by viewing the emitted light through a slit and a refractive medium, such that the light is split or dispersed into its component wavelengths so that it can be recorded and analysed. This phenomenon is similar to viewing a rainbow from light that has passed through a prism. When light from an astronomical object is recorded as a spectrum, a story can be told out of the unique characteristics of the light as it passes through its environment. Different features in the spectrum can be identified as the photons interacts with molecules or atoms in intervening gas clouds as they travel to the observer; these are called absorption or emission features (see Figure 1). The shape of an emission line on a plot of flux (how bright an object appears to an observer) versus wavelength is called the profile or spectrum. Slipher was the first to observe galaxy profiles were shifted mostly towards the longer, or red, wavelengths.

The term “redshift” is used to describe the astronomical phenomenon of typical absorption or emission features being shifted to longer wavelengths due to a physical phenomenon called the Doppler effect. A redshift is thus the increase in the measured wavelength of an object’s electromagnetic radiation as the object moves away from an observer. Denoted mathematically, redshift can be expressed by  $z$ , and is the ratio between an object’s observed ( $\lambda_0$ ) and rest wavelength ( $\lambda_R$ ) to its rest wavelength:

$$z = \frac{\lambda_0 - \lambda_R}{\lambda_R}. \quad (1)$$

If the value of  $z$  is known, we can rearrange Eq. 1 such that an object’s observed wavelength can be shifted back to the rest frame’s wavelength by

$$\lambda_R = \frac{\lambda_0}{1 + z} \quad (2)$$

---

<sup>1</sup>In fact, such “spiral nebulae” were already speculated to be larger systems; see Fath (1909) early work on the case of galaxy NGC 1068, where he observed a composite spectrum, showing both bright and absorption lines; the six bright lines were recognizable as ones seen in the spectra of gaseous nebulae.

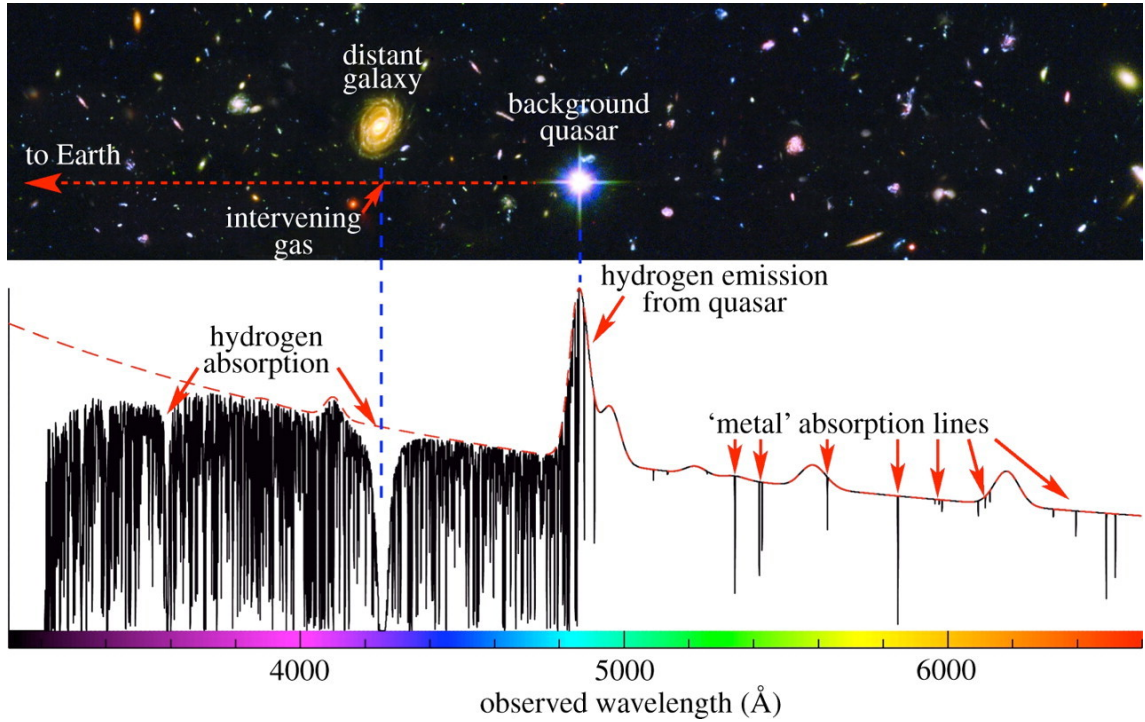


Figure 1: An illustration from Pettini (2011) of the quasar absorption line technique used to probe the distant Universe. Encoded in the absorption spectrum of a distant quasar is information on the physical properties of gas and galaxies located in the path of the light rays from the quasar to Earth. Shown is the emission lines from the quasar that are broadened and peak upwards.

At high redshifts, velocities are close to, or surpass the speed of light. Relativistic redshift then must be used near the speed of light (Einstein 1905), such that:

$$z = \frac{v}{c} \text{ for } z < 0.1 \quad (3)$$

$$\frac{v}{c} = \frac{(1+z)^2 - 1}{(1+z)^2 + 1} \text{ or } \frac{\lambda_0}{\lambda_R} = \sqrt{\frac{1 - \frac{v}{c}}{1 + \frac{v}{c}}} \quad (4)$$

where  $v$  is a galaxy's velocity,  $c$  is the speed of light ( $c = 3 \times 10^8$  m/s),  $\lambda_R$  is the rest wavelength of the radiation, and  $\lambda_0$  is the observed wavelength which has been shifted due to the radial motion between the object and the observer.<sup>2</sup>

Interestingly, when Hubble plotted the velocity vs. the distance of the galaxies (Figure 2), he found galaxies that were smaller, fainter, and more distant appeared to have a larger redshift.

Thus, the farther away a galaxy is, the faster it appears to be moving away from Earth. In fact, Hubble found almost all galaxies appeared to be moving away from us, with all of the galaxies moving away from one another – in other words, the universe appeared to be expanding. This can

<sup>2</sup>A slightly separate notion: the definition of redshift itself allows us to look back through time. Since light travels at a large but finite speed, it takes time for light to cover large distances. Thus, when we see the light of very distant objects in the Universe, we are actually seeing light emitted from them a long time ago: we see them literally as they were in the distant past.

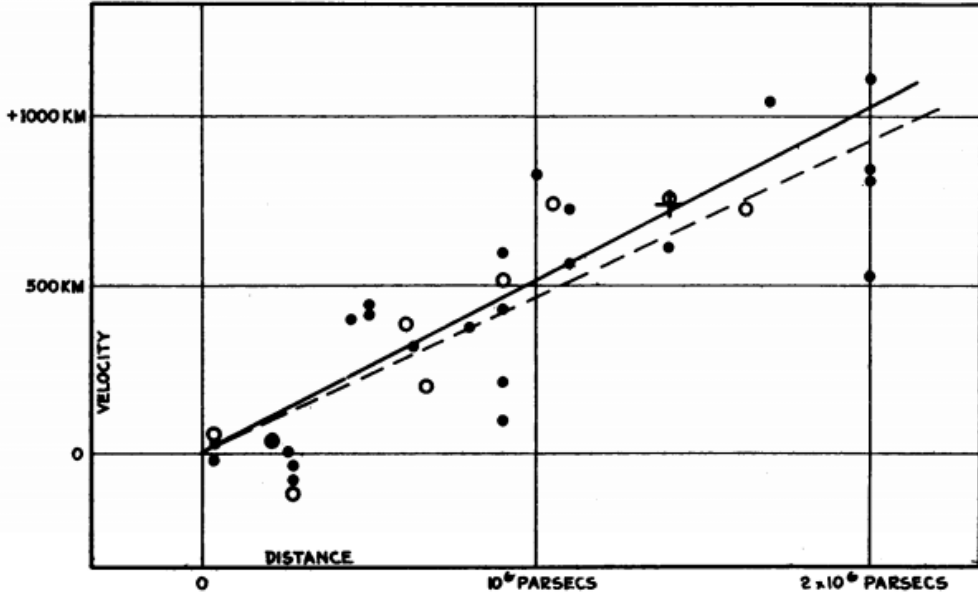


**FIGURE 1**  
**Velocity-Distance Relation among Extra-Galactic Nebulae.**

Figure 2: Hubble’s Velocity vs. Distance figure of galaxies Hubble 1929. The correlation between faster moving galaxies (known as “extra-galactic nebulae” at-the-time) measured at a higher distances suggested all cosmological objects are constantly moving away from us—the expansion of the Universe.

be expressed as the outward radial velocity,  $v$ , of the galaxy is proportional to its distance,  $d$ , from us:

$$v = H_0 d, \quad (5)$$

where  $H_0$  is the Hubble constant describing the rate at which the local Universe is expanding. Since  $H_0$  is constant in space only at a fixed time, it varies with time in nearly all cosmological models, and all observations of far distant objects are also observations into the distant past, when the “constant” had a different value. Thus, the “Hubble parameter” becomes important at higher redshifts and is described as,

$$H(z) = \frac{\dot{a}(t)}{a(t)}, \quad (6)$$

where  $a(t)$  is a scale factor which describes the expansion of the Universe, often the  $H_0$  value is expressed in the unit of  $\text{km s}^{-1} \text{Mpc}^{-1}$ , to describe the expansion of our universe (Wu et al. 2020; Zhang et al. 2010).

### 1.1.2 Strange Nuclear Emission in Galaxies

Around a decade after Hubble’s discovery of the expanding Universe, the systematic study of galaxies with nuclear emission lines began by the work of Seyfert (1943). Seyfert obtained spectrograms

---

of six galaxies with nearly stellar nuclei showing emission lines superimposed on a normal G-type (solar type) spectrum : NGC 1068, 1275, 3516, 4051, 4151, and 7469 from the New General Catalogue of Nebulae, Clusters of Stars, and Galaxies (NGC; Dreyer 1888). The two brightest (NGC 1068 and 4151) showed the stronger emission lines typically found in planetary nebulae, like NGC 7027. Seyfert attributed the large widths of the lines to Doppler shifts, reaching up to  $8500 \text{ km s}^{-1}$  for the hydrogen lines of NGC 3516 and 7469. The emission-line profiles differed from line to line and from object to object, but two patterns proved typical of these bright galaxies: the forbidden and permitted lines in NGC 1068 had similar profiles with widths of  $\sim 3000 \text{ km s}^{-1}$ . In contrast, NGC 4151 showed relatively narrow forbidden lines and corresponding narrow cores of the permitted lines but the hydrogen lines had very broad ( $7500 \text{ km s}^{-1}$ ) wings that were absent from the profiles of the forbidden lines. Seyfert contrasted these spectra with the narrow emission lines of the diffuse nebulae (H II regions) seen in irregular galaxies and in the arms of spiral galaxies. Thus, galaxies with high-excitation *nuclear* emission lines are now called “Seyfert” galaxies and are a type of Active Galactic Nuclei (AGN) (see Section 1.1.3). However, the discovery of Seyfert galaxies was not enough to require accretion onto SMBHs as the origin for the emission—that came from the development of radio astronomy.

### 1.1.3 The Discovery of Quasars

Nearly forty years after Hubble’s discovery and twenty years after Seyfert’s, in 1963, Maarten Schmidt (1929-2022) was studying radio Source 3C 273, in the Third Cambridge (3C) radio catalog observing the strongest radio sources (i.e. radio-loud; Kellermann et al. 1969), with the Hale 200 in telescope at Mount Palomar Observatory operated by Caltech Institute of Technology (Schmidt 1963). The source, as seen in Figure 3, was unusual because the radio signals appeared to be coming from a star, which do not usually produce strong radio-emission.

The spectrum of the star was further puzzling; it had three very broad emission lines that, at the time, they had no explanation for. Schmidt could not figure out what elements produced the bright spectral lines. Then he realized that the unfamiliar lines were simply hydrogen Balmer lines that had been shifted to very different wavelengths. The unidentified stellar object was at the center of the nuclear region of the galaxy with a cosmological redshift of  $z = 0.159$ , however corrected from  $z = 0.229$  through spectroscopic analysis (Schmidt and Matthews 1964). According to Hubble’s Law (Eq. 5), an object with an extreme radial velocity would be located at a very large distance. By assuming a cosmological origin for the redshift, this meant the distance would be around 1635 Mpc, with an absolute magnitude of  $-26^3$ ; this object is extremely luminous especially for how

---

<sup>3</sup>Please recall that the star, Vega, is the reference point for the magnitude system and that astronomers now use

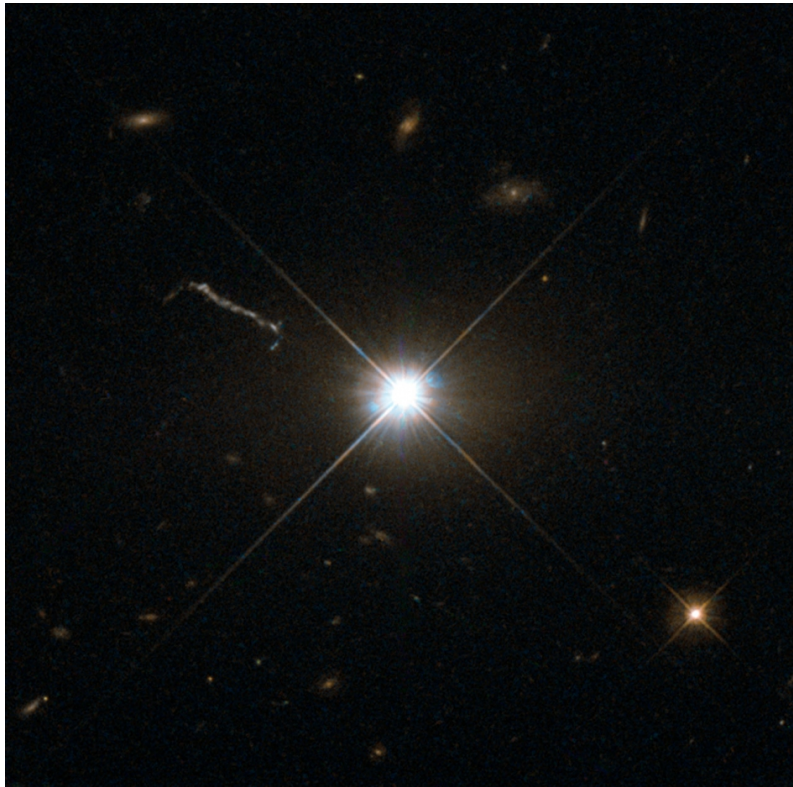


Figure 3: This image from Hubble’s Wide Field and Planetary Camera 2 (WFPC2) is known as the best of ancient and brilliant quasar 3C 273, which resides in a giant elliptical galaxy in the constellation of Virgo. Its light has taken about 2.5 billion years to reach us. Despite this great distance, it is still one of the closest quasars to Earth. It was the first quasar ever to be identified by Schmidt, and was discovered in the early 1960s by astronomer Allan Sandage. Credit: ESA/Hubble & NASA

distant the object is. This nuclear region would be about 100 times brighter optically than the most luminous galaxies which had been identified with radio sources, thus far, and it was decided the explanation in terms of an extragalactic origin would be most direct and placed this object in the classification of *quasi-stellar objects* (QSOs), meaning “star-like”. Figure 4 depicts different Sloan Digital Sky Survey (SDSS) spectra for a star, galaxy, and quasi-stellar object. Carefully differentiating between these spectra was part of the revolutionizing work Schmidt accomplished.

Furthermore, all of these radio-loud QSO sources had the same characteristics: high redshifts, broad emission lines, and extremely large luminosities emanating from very compact regions. Looking back at Figure 1 (Pettini 2011), different classes of emission lines are indicated in the spectrum. Most of the ‘hydrogen emission’ is produced by diffuse intergalactic gas, while the ‘metal emission lines’ and the strongest hydrogen lines are thought to be associated with galaxies. In the spectrum of a given quasar, there are normally many sets of emission lines that are broadened due to the high speeds at which the atoms in the gas clouds surrounding the nuclear region are moving.

---

56 magnitudes where the brightest thing we can see (the Sun, -26) to the faintest (faint objects in Hubble Space Telescope images, +30).

# Sloan Digital Sky Survey Spectra

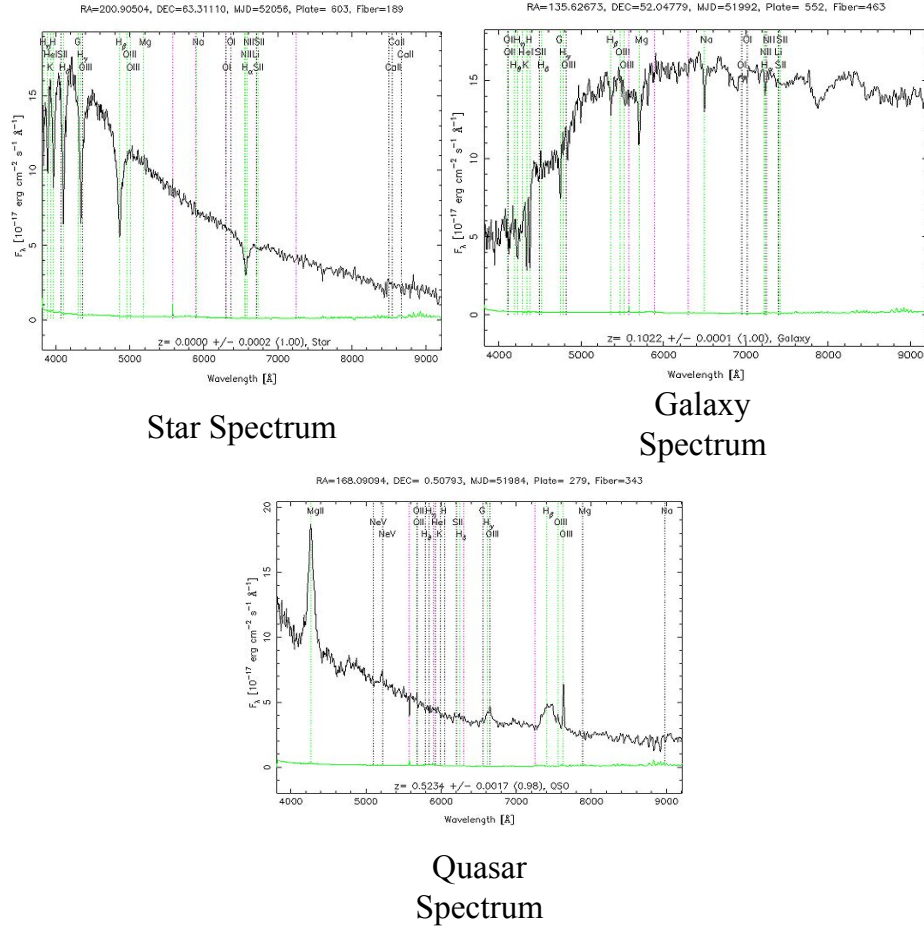


Figure 4: Sloan Digital Sky Survey (SDSS) Spectra for a typical star (panel 1), galaxy (panel 2), and quasar (panel 3). The broad absorption lines have been analyzed to indicate the quasar spectrum to be different from the similar star spectrum. In panel 1, the stellar spectrum is filled with absorption lines at particular colors or wavelengths following a power-law continuum. The galactic spectrum in panel 2 displays a composite of absorption and emission lines, while the quasar spectrum in panel 3 shows classic broad emission lines that have been shifted due to the Doppler effect. These images are not shown to scale as we are comparing the power-law continuum shape and differences in emission/absorption lines of each spectrum.

To further probe the understanding of these new objects, the First Texas Symposium on Relativistic Astrophysics: Quasi-Stellar Sources and Gravitational Collapse, was held in December of 1963. The meeting attempted to explain the immense energy output at both optical and radio wavelengths from these QSOs. While these huge sources were first detected in the radio, over time the number of identified radio-loud (quasars) and radio-quiet (QSOs) objects grew and the distinction in nomenclature blurred, such that all luminous objects with broad emission lines and cosmological distances are now both called quasars and QSOs, interchangeably. The same year, Hoyle and Fowler (1963) presented the first—ultimately incorrect—theoretical model that could account for these extreme observed phenomena: gravitational collapse of a supermassive ( $\sim 10^8 M_\odot$ )

---

star in the center of a galaxy. Instead, we now understand accretion onto a SMBH is what fuels active galactic nuclei.

#### 1.1.4 Accretion Properties

An accretion model was first proposed by Otto Schmidt in 1944 for the study of protoplanetary clouds (Schmidt and Lebedinsky 2001), but was further developed in a quantitative way in 1969 by Viktor Safronov (Safronov 1972). Specifically, Safronov calculated the different stages of terrestrial planet formation and his model was originally developed to explain the mechanism of accretion by stars (Bondi and Hoyle 1944). We now understand accretion, overall, as the extraction of gravitational potential energy from material that is infalling onto a gravitating body. For example, when atoms in a gas cloud collapse onto a gravitating body, they lose potential energy, then heating up, gaining kinetic energy, and the conservation of angular momentum ensures that the cloud forms a flattened disk—the accretion disk. To express mathematically, for stars or planets, it is simple: the energy stored in the rest mass of the object is defined as,

$$E = mc^2 \tag{7}$$

where  $E$  is energy,  $m$  is the mass of the object, and  $c$  is the speed of light (Einstein 1905).

It is now known that ultra-massive, ultra-luminous, short-lived stars will leave behind black holes as their remnants (Ryden and Peterson 2020). The stars supernova and under the effect of gravity turn into an eventual black hole, containing a point of singularity at its center. General relativity, Einstein’s theory of space, time, and gravity (Einstein 1915), allows for the existence of singularities. Once the body has collapsed down to the point where its escape velocity is the speed of light, the body will get ever smaller, more and more dense, without limit. It has formed a relativistic black hole where a spacetime singularity will form from the collapsing matter once the critical point of black-hole formation is reached.

Now moving further out from the black hole’s singularity, the event horizon is the location where the kinetic energy of light escaping equals the potential energy of the black hole. The event horizon’s distance from the singularity is called the Schwarzschild radius ( $r_{Sch}$ ), after the physicist Karl Schwarzschild, who first calculated it in a relativistically correct manner. However as matter falls toward a black hole, a large amount of energy can, theoretically, be extracted from it—the accretion. If we suppose a mass  $m$  falls from a large distance  $r \gg r_{Sch}$  towards the Schwarzschild

---

radius (Eq. 10), then its loss of gravitational potential energy will be,

$$\Delta E = \frac{GM_{bh}m}{r_{Sch}} \quad (8)$$

where again  $M_{bh}$  is the mass of the black hole,  $G$  is Newton's gravitational constant ( $6.67 \times 10^{-11} \text{ kg}^{-2}\text{m}^2$ ),  $r_{Sch}$  is the Schwarzschild Radius. For a spherical body, we have the escape velocity,  $v_{esc}$  defined as,

$$v_{esc} = \left( \frac{2GM_{bh}}{r} \right)^{1/2} \quad (9)$$

such that when  $v_{esc} = c$  for a body of mass,  $M$ , the radius,  $r$ , is,

$$r = \frac{2GM_{bh}}{c^2} \equiv r_{Sch} \sim \frac{1}{2}mc^2 \quad (10)$$

where  $G$  is Newton's gravitational constant ( $6.67 \times 10^{-11} \text{ Newtons kg}^{-2}\text{m}^2$ ) and  $M_{bh}$  is the mass of the black hole.

Even the mass is torn apart by the intense gravitational pull near the speed of light, it will pass the event horizon with a speed  $v \sim c/\sqrt{2}$ , and its kinetic energy will swell the mass of the black hole. If the mass is decelerated by slamming into an accretion disk, its kinetic energy will be converted to thermal energy, and ultimately photon energy. However, the conversion here from gravitational potential energy to photon energy is not exact.

Now, asking how much of the rest mass is converted to energy using Eqs. 7 and 8 we express the efficiency,  $\eta$ , by the energy carried away by photons as,

$$\Delta E_{phot} = \eta mc^2. \quad (11)$$

Fusion will power a star for up to 90% of its lifetime (Ryden and Peterson 2020), however the energy conversion from accretion onto black holes is inefficient. For reference, the efficiency at the innermost stable circular orbit for a non-rotating black hole is reported as  $\eta = 0.0572$ , which is 5.72% of the rest mass converted to energy. Increasingly, at an innermost stable circular orbit for a maximally rotating prograde orbit the efficiency is reported as  $\eta = 0.423$ , having a much high percentage of rest mass converted to energy, 42.3%. Observations of AGN and quasars have shown that  $\eta = 0.1 - 0.15$  (Tremaine et al. 2002), which means that a single gram of matter falling toward the central SMBH yields  $9 \times 10^{12}$  Joules of radiation energy.

It is naive to assume that by feeding matter to a black hole at higher and higher rates, that one can make an AGN have an extreme luminosity, or measured brightness. However, even supermassive

---

black holes have their limits. Sir Arthur Eddington showed that the inward gravitational pressure of a star must maintain the outward radiation and gas pressure to remain in equilibrium is called the Eddington Luminosity Limit. In fact, for a given black hole mass  $M_{bh}$  if we require too high of a luminosity, then the gas surrounding the black hole will be blown away by radiation pressure. We can take the energy output from accretion to find the growth rate by accretion by taking the energy output time derivative as,

$$L = \eta \dot{M} c^2. \quad (12)$$

Then suppose at a distance  $r$  from the active black hole, the photons have an energy flux

$$F = \frac{L}{4\pi r^2} \quad (13)$$

where the flux is described as the amount of energy from a luminous object that reaches a given surface or location. Flux is given by the luminosity,  $L$ , in  $erg\ s^{-1}$  over  $4\pi r^2$  in  $cm^2$ , and is defined as how bright an object appears to the observer measured in  $erg\ s^{-1}\ cm^{-2}$ .

In addition to flux, each photon has a momentum,  $p = E/c$ , and thus the outward flow of photons creates a momentum flux building from Eq. 13,

$$F_p = \frac{F}{c} = \frac{1}{c} \frac{L}{4\pi r^2}. \quad (14)$$

Since the photons carry momentum, they can exert a force on the free electrons and protons and the ionized gas surrounding the black hole. The electrons experience an outward force due to radiation pressure in which the amplitude of the force is equal to the momentum flux times the electron's cross-section (utilizing the Thomson cross-section for electrons:  $\sigma_e = 6.65 \times 10^{-29} m^2$ ):

$$F_{rad} = \sigma_e F_p = \frac{\sigma_e L}{4\pi c r^2}. \quad (15)$$

Thus, as the electron is accelerated, so too is the nearest proton along with it, which maintains charge neutrality.

On the other hand, the inward force on the electron-proton pair is provided by gravity where,

$$F_{grav} = -\frac{GM_{bh}(m_p + m_e)}{r^2} \sim -\frac{GM_{bh}m_p}{r^2}, \quad (16)$$

and the electron mass  $m_e$  is insignificant as compared to the proton mass  $m_p$ . The photons escape a gravitational potential if it has a sufficient escape velocity. In terms of energy, a photon's kinetic energy must then exceed the gravitational potential energy of the black hole in order to escape.

---

Such that, accretion can only take place so long as the gravitational force remains larger than the radiation force:  $F_{grav} > F_{rad}$ .

Thus for a black hole, the luminosity beyond which accretion is impossible (or maximum luminosity) we follow the derivation from Willott et al. (2010) where,

$$L_{Edd} = \frac{4\pi GMcm_p}{\sigma_e} \cong 1.3 \times 10^{39} W \left( \frac{M_{bh}}{10^8 M_\odot} \right) \quad (17)$$

When a black hole accretes at the Eddington Luminosity,  $L = L_{Edd}$ , then the proportion of potential energy that gets changed to radiation, or the efficiency,  $\eta$ , by  $\sim 0.1$  or 10% (Tremaine et al. 2002). Further, the Eddington Ratio of an accreting SMBH is defined relative to its Bolometric Luminosity,  $L$ ,

$$\lambda_{Edd} = L/L_{Edd} \quad (18)$$

which describes the total amount of energy across the electromagnetic spectrum radiated by an object.

If the luminosity is greater than  $L_{Edd}$ , then the ionized gas surrounding the black hole will be accelerated outward and accretion will cease. Thus, the maximum accretion rate for black holes is,

$$\dot{M}_E = \frac{L_{Edd}}{\eta c^2} = 2M_\odot \text{yr}^{-1} \left( \frac{M_{bh}}{10^8 M_\odot} \right) \left( \frac{\eta}{0.1} \right)^{-1}. \quad (19)$$

If one were to simulate a black hole accreting more rapidly than described by Eq. 19, it must eject the gas back out. It is then useful to express the accretion rate in terms of the Eddington rate,

$$\dot{m} = \frac{\dot{M}}{\dot{M}_E} \quad (20)$$

which we refer to as the Eddington ratio throughout this work.

### 1.1.5 Emission Properties

The radiation we receive from a supermassive black hole comes not from the black hole itself, but instead originates in the accretion disk surrounding it: the mechanisms by which angular momentum is lost as matter spirals in via the accretion disk. Gas has to lose angular momentum for accretion to occur (i.e. for material to move inward in radius); friction between gas facilitates this process by causing gas to lose angular momentum and slowly spiral inwards. Viscosity of the rapidly accelerating gas in the accretion disk, as it moves from large radius to a smaller radius, converts kinetic energy to heat and radiation while losing gravitational potential energy at the

---

rate,

$$dL_{potential} = \frac{GMdM}{r^2} \frac{dr}{dt} = \frac{GMdM}{r^2} v, \quad (21)$$

where  $v$  is the radial speed of which a patch of the accretion disk, with area  $dA$  and the mass of the patch is  $dM = \Sigma dA$  (where  $\Sigma$  is the mass surface density) at a distance  $r$  from the black hole, moves toward the black hole.

Particle collisions of the gas that do not provide enough friction to cause loss of angular momentum instead cause magnetic fields. The radio emission of jets in radio AGN is explained as the magnetic fields are twisted into helical shapes by the rotation of a spinning black hole or the accretion disk itself (Lister et al. 2003; Pasetto et al. 2021; Perucho et al. 2012). Electrons are then accelerated by these magnetic fields, causing them to radiate with synchrotron emission. When the magnetic fields are twisted up by the black hole spin, the rotational energy of the black hole is the ultimate source of energy for the jet. Otherwise, the potential energy loss by matter moving inwards is proportional to the mass it is falling onto and inversely proportional to the final radius. The radiation subsequently leaks through the disk, escapes from its surface, and travels along trajectories curved (in space) by the strong gravity of the black hole, eventually reaching our telescopes as such luminous sources for their mass in the universe. The strongest radio galaxies have  $L_{radio} > 10^{38} W \sim 3 \times 10^{11} L_{\odot}$  with jets measuring over a megaparsec long, in extreme cases (see Figure 5).

As mentioned in Section 1.1.1, Slipher, Hubble and Seyfert all used the emission-line profiles from their measured spectra to derive astrophysical parameters, just as we will do in this work. If all the emitting gas were quiescent (i.e. no relative motion), then the line would look like a narrow spike. However for a broad line quasar spectrum, in which the light passes through gas accreting around a SMBH, we can analyze the profile to give us the velocity distribution of the emitting gas. The velocity distribution of the emitting gas in a circular orbit around a mass  $M$  at radius  $R$  would have a velocity  $v^2 = \frac{GM}{R}$ , where  $G$  is Newton's gravitation constant.

Analyzing the quasar profile, the Full Width at Half Maximum (FWHM) is the width measured at half level between the continuum and the peak of the line. The FWHM is expressed either in wavelength unit or in speed unit when the objective is to measure expansion or disk speeds (if FWHM is in unit of wavelength, the width in km/sec is given by  $v_{FWHM} = \frac{cFWHM}{\lambda}$ , with  $c$  being the speed of the light ( $3 \times 10^5$  km/s). For our purposes, velocity at FWHM ( $v_{FWHM}$ ) expresses the velocity recorded as the photoionized gas clouds are moving around the black hole at great speeds, approximately  $10^3 - 10^4$  km/s, causing the emission lines to be Doppler broadened due to their high velocity.

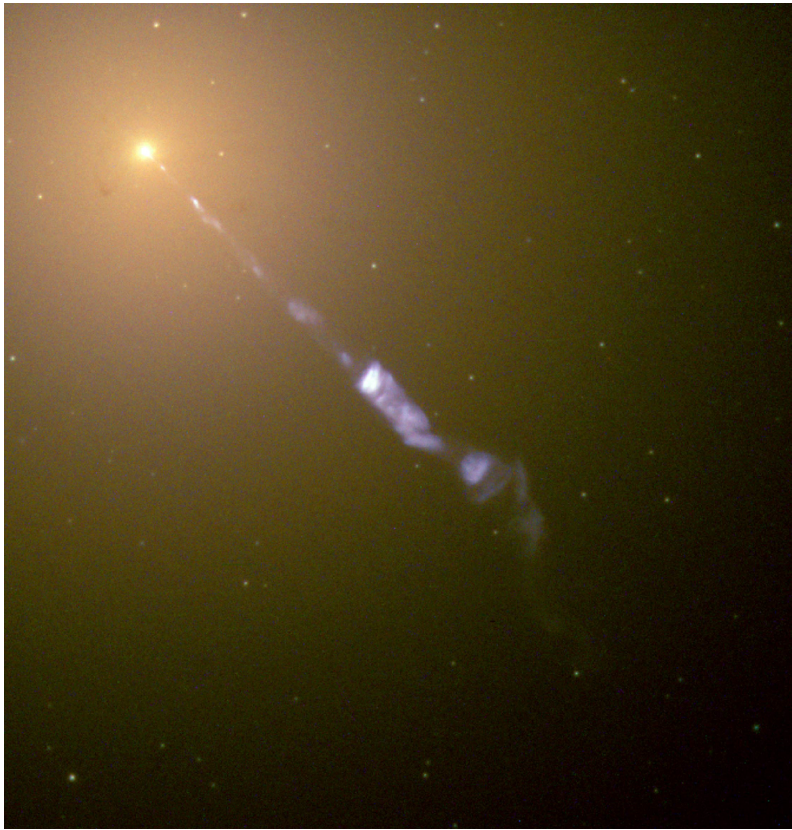


Figure 5: In this Hubble image, the blue jet contrasts with the yellow glow from the combined light of billions of unresolved stars and the center black hole, in M87. The jet is a black-hole-powered stream of material that is being ejected from M87’s BH core. Credits: NASA and the Hubble Heritage Team (STScI/AURA)

While we have a thorough understanding of the physics surrounding the accretion process onto SMBH, the question as to why some galaxies have active nuclei and why others lack any accretion is not fully understood, though the intrinsic relationship with the SMBH’s host-galaxy may be a fruitful source to search.

### 1.1.6 Active Galactic Nuclei and Galaxy Formation in the Dusty Universe

The center component in the anatomy of every galaxy, its SMBH, appears to have an overreaching influence on its host, despite its small sphere of gravitational influence (Ferrarese and Merritt 2000; Marconi and Hunt 2003; Reines and Volonteri 2015). With recorded SMBH masses ( $M_{BH}$ ) of  $\sim 10^6-10^9 M_{\odot}$ , the black hole’s gravity affects a region that is, at the largest, a few tens of parsecs in size, minuscule compared to its host-galaxy, and yet there appears to be an evolutionary connection between the two (Magorrian et al. 1998; Smethurst et al. 2022). Observations have established correlations between SMBH mass and host-galaxy properties, such as luminosity (Becker et al. 1995; McLure and Dunlop 2002), and stellar velocity dispersion  $\sigma$ , in the ( $M_{BH} - \sigma$ ) relationship (Ferrarese and Merritt 2000; Gebhardt et al. 2000; Tremaine et al. 2002). Further, the energy

---

output from these AGN likely couples to their host galaxies, heating interstellar gas, perhaps inducing (positive feedback; Silk and Rees 1998) - star formation and likely suppressing (negative feedback; Schawinski et al. 2007). This feedback may also grow the SMBH until the feedback energy from the SMBH expels gas which may effectively turn off the accretion process (Silk and Rees 1998). Broadly, the growth of supermassive black holes appears to be driven by galaxy mergers, violent merger-free processes and/or so-called ‘secular’ processes.

Quasars and other similar active SMBHs, which are collectively known as AGN, have masses in the range  $10^6 M_\odot < M < 10^{10} M_\odot$  that reside at the center of galaxies, like our own. The “active” SMBHs at the center of their host-galaxy are the most powerful steady energy sources known in the Universe. Many have luminosity,  $L$ , in excess of their corresponding Eddington luminosities. The high efficiency of quasars,  $\eta = \frac{L}{Mc^2} > 0.1$ , where  $M$  is the mass supply rate from accretion (“the accretion rate”), is puzzling (Abramowicz and Fragile 2013). Black hole accretion disk theory predicts that  $L > L_{Edd}$  would imply a small accretion efficiency  $\eta \ll 0.1$ . However, the famous “Soltan argument,” based on quasar counts (Soltan 1982), shows that on a long time average,  $t \sim t_{Hubble}$ , quasars can have both  $L > L_{Edd}$  and  $\eta \sim 0.1$ , making them the most luminous sources in the Universe throughout time. However, the driving force of this luminosity and power has been long debated over the past decades.

QSOs with moderate-luminosity at  $z \sim 1.0$  are typically in a slow-growth phase, where  $L/L_{Edd} \leq 0.01$ , and are hosted in galaxies with strong disk components, implying the black holes are not fed by major mergers (Simmons et al. 2011). Moving further out to  $z = 2.7$ , the fraction of disk-dominated AGN is even higher: more than half the galaxies hosting moderate-luminosity AGN at  $z \sim 2$  (cosmic noon) are unambiguously disk-dominated, and they seem to be found in a variety of growth phases. In order to quantify the effects of secular evolution on black hole growth, a population of bulgeless galaxies – lacking the classical bulges believed to result from mergers – is presented by Simmons et al. (2013) and selected from the Sloan Digital Sky Survey using visual classifications from Galaxy Zoo (Masters 2013). From the bulgeless sample they find indications are consistent with the relation between black hole mass and total galaxy mass, a relation derived from elliptical galaxies with a history including strong mergers. This implies that the search for the fundamental cause of the galaxy-black hole connection may be in isolation from merger-driven processes. More recent observational and theoretical studies (Smethurst et al. 2022) have suggested that SMBHs grow mostly through these non-merger/secular processes.

Much of the debate in what drives an AGN is due to the fact in the standard picture only the approximate structure of AGN is known, but much of the detailed physics is literally hidden from view. Dusty molecular clouds, often modeled as a ‘torus’ co-planar with the accretion disk, obscure

---

the broad emission lines along certain lines of sight. Beyond the obscuring clouds lies the narrow emission line region where photoionized gas is extending out either end of the dusty torus. The dense photoionized gas in between the dusty torus and the central engine is the broad line region (BLR). Like the BLR, the narrow line region (NLR) is also Doppler broadened, but the velocities of the clouds in this region are much smaller, approximately  $10^2 - 10^3$  km/s, since they are further away from the BH. Since an important feature of the NLR is that it is orientation-independent, we can observe it in all objects, even if we are within the plane of the dusty torus. This contrasts the BLR, which is only visible when we are looking down towards the ionization cone. This inherently axisymmetric model of AGN implies a radically different AGN appearance at different aspect angles. In practice, AGN of different orientations will therefore be assigned to different classes. In an effort to cohesively explain the multiple quasar phenomena observed, Urry and Padovani (1995) invoked orientation-based arguments to include narrow emission line spectra of AGN (e.g., Seyfert 2 and narrow-line radio galaxies), as well as highly variable featureless spectra (e.g., BL Lac objects<sup>4</sup>). Such unified orientation models depict an axisymmetric geometry with an accretion disk at the center surrounded by broad emission line clouds.

The AGN unification model developed by Urry and Padovani (1995) is successful at explaining the different varieties of AGN spectra: whether broad lines are seen depends on our viewing angle toward the AGN. A unified AGN model is shown in Figure 6 depicting a comprehensive view of observational AGN theories and standard nomenclature (Becker et al. 1995). In other words, the unification model for AGN states that the difference in viewing angle to the central engine of the accreting-black-hole system determines the observed spectral shape, including emission line widths. Type 1 (broad-line) sources are understood through this model to be seen at orientation angles nearer to the pole. Beyond a certain range of viewing angles, the line-of-sight to the broad line region is blocked by close-in high-column-density gas and dust (i.e., the so-called ‘torus’).

This dust enshrouding the nucleus along the line-of-sight intrinsically reddens the spectra of the quasar through a process known as extinction. Interstellar extinction occurs when dust molecules along the line of sight scatter and absorb light coming from distant objects. We therefore see these objects as dimmer and redder than they really are. This is similar to the effect seen when dust particles in the Earth’s atmosphere create red sunsets. Discovered by Robert Trumpler<sup>5</sup> in 1940 (Trumpler 1940), who viewed distant star clusters appearing dimmer than expected based on their measured distance, he found the dimming occurs because the typical size of interstellar dust grains

---

<sup>4</sup>BL Lac objects are named after their archetype, BL Lacertae. Originally mistaken as a star due to its bright unresolved nucleus that diffuses starlight surrounding it, however the radio emission from BL Lacertae was too much to be a star and was concluded to be a distant elliptical galaxy. The nuclei of BL Lac objects are then rapidly variable and do not show any emission lines making it difficult to determine the distance to a BL Lac object.

<sup>5</sup>See Weaver and Weaver (1957) for more historical details. Note, previous astronomers also observed stellar reddening though did not attribute its effect to dust.

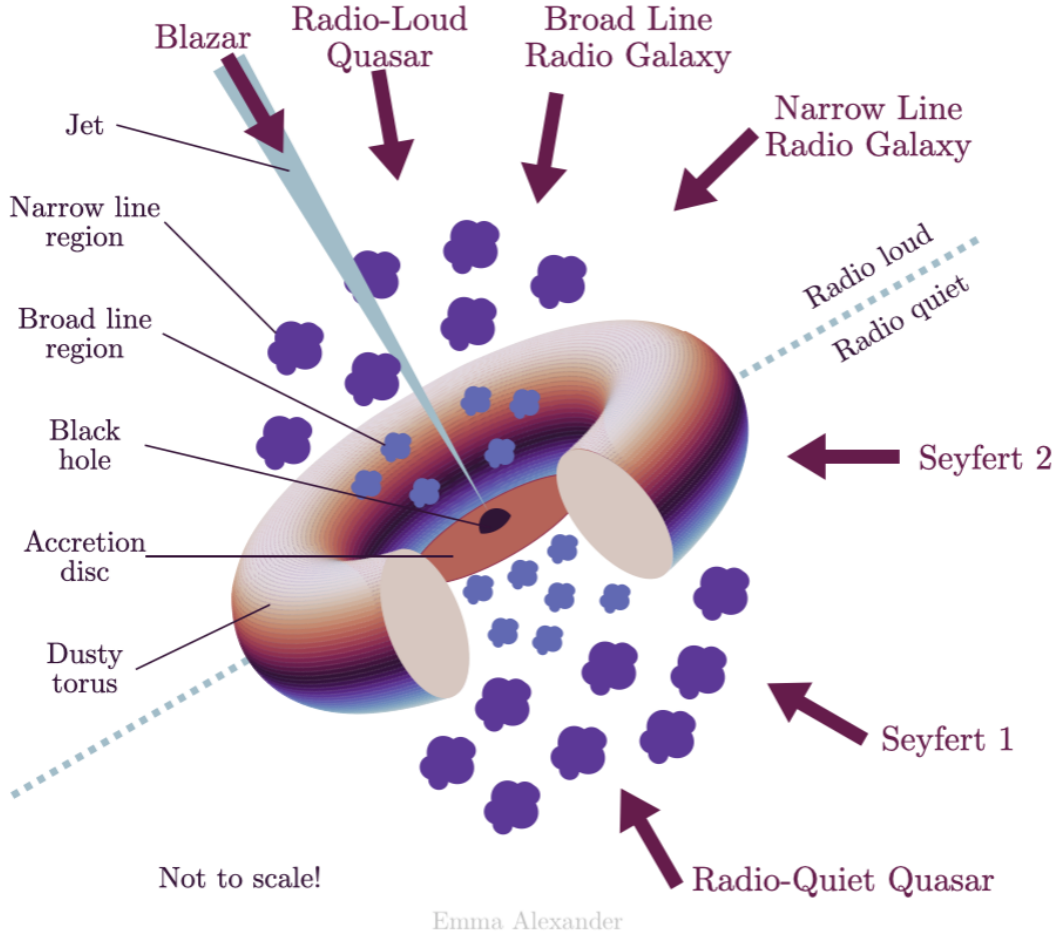


Figure 6: The Unified AGN Model illustration created by Emma Alexander adapted from Becker et al. (1995). The black lines label different properties of the AGN previously discussed, while the thick arrows represent different viewing angles, and the observed object which results from them. Note the asymmetry of the diagram; this is to demonstrate the two different possibilities of radio loud/quiet and is not representative of a single object and further, AGN types depend largely on the viewing angle (Urry and Padovani 1995).

is similar to the wavelength of blue light. Thus blue light is either scattered or absorbed by the dust grains, essentially removing the shorter wavelengths from the light reaching our telescopes and making objects appear dimmer (extinction) and redder (interstellar reddening) than they really are. When scattering occurs, the change in flux can be characterized by,

$$F(\lambda) = F_0(\lambda)10^{-A\lambda}, \quad (22)$$

where  $A(\lambda)$  is the amount of extinction that occurs in magnitudes,

$$A(\lambda) = -2.5\log_{10} \left( \frac{F(\lambda)}{F_0(\lambda)} \right), \quad (23)$$

such that,  $F(\lambda)$  is the measured flux and  $F_0(\lambda)$  is what the flux would be with no dust. However,

---

due to the way magnitudes are defined in Eq. 22, we express the optical depth of the dust as:

$$\tau(\lambda) = -\ln\left(\frac{F(\lambda)}{F_0(\lambda)}\right). \quad (24)$$

Optical depth,  $\tau(\lambda)$ , is the unitless quantity that we use to describe the optical depth of a gas for a photon of wavelength  $\lambda$ . However, we cannot directly compute  $\tau(\lambda)$  since not enough is known about the nature of the dust that causes scattering. All dust relations must still be taken into account while taking astronomical observations of the dusty Universe, thus, the dust relations must be computed empirically. The current dust relation standard was calculated by Fitzpatrick (1999), in which he observed the flux,  $F(\lambda)$ , from objects with a known intrinsic flux,  $F_0(\lambda)$ , to derive  $\tau(\lambda)$  in the form of color excess,  $E(B - V)$ .

Here, Fitzpatrick (Fitzpatrick 1999) quantifies interstellar reddening as the “color excess”, defined as the difference between an object’s observed color index and its intrinsic color index (sometimes referred to as its normal color index). The latter is the theoretical value which it would have if unaffected by extinction. In the first UBV photometric system devised in the 1950s and subsequent systems, the object’s color excess  $E(B - V)$  is related to the object’s B-V color (calibrated blue B band ( $\sim 4500\text{\AA}$ ) minus calibrated visible V band,  $\sim 5500\text{\AA}$ ) by:

$$E(B - V) = (B - V)_{observed} - (B - V)_{intrinsic}. \quad (25)$$

Then the ratio between total extinction and color excess is usually expressed as,

$$k(\lambda) = \frac{A(\lambda)}{E(B - V)}, \quad (26)$$

and we can solve for the optical depth as:

$$\tau(\lambda) = \frac{k(\lambda)E(B - V)}{\log_{10}(e)} \ln(10). \quad (27)$$

Finally, we define the ratio between the total extinction in the visible band (the human eye) to the color excess as,

$$R_v \equiv \frac{A(V)}{E(B - V)} \quad (28)$$

Hence we will reference this measurable quantity,  $E(B - V)$ , as the amount of dust that causes reddening or extinction. It is important to note the distinction between interstellar reddening as a different phenomenon from redshift, which is the proportional frequency shifts of spectra without distortion as discussed previously (see Section 1.1.1).

---

It is known that as we move to longer wavelengths, the photons do not interact as strongly with the dust grains, some fraction of the red light will make it through to our detectors. For this reason astronomers generally use infrared wavelengths to probe the dusty regions of our universe, as shown by the recent heralding of the JWST which uses infrared to peek through the distant dusty Universe (Rigby et al. 2022). In relation to this study, mid-infrared selection successfully identified broader populations of QSOs that were less affected by the amount of dust causing reddening (Donley et al. 2012; Jarrett et al. 2011; Lacy et al. 2005; Stern et al. 2005). However, the amount of extinction can still be significantly higher in specific directions, such as along the line-of-sight to the center of galaxies, including extinction from the host-galaxy itself and the intrinsic reddening from the dusty torus surrounding the AGN. The amount of extinction along the line-of-sight to the center of an AGN host-galaxy will intrinsically redden the spectrum of the quasar. Effectively, this reddening further blocks from view of the physics taking place surrounding the QSO and distorts the data. As such, rigorous studies of QSOs must take into account the host-galaxy spectrum and subtract from the QSO spectrum to ascertain the true data.

### 1.1.7 Quasar Demographics and Colors

A relatively newly discovered and largely unexplored population of sources that may help resolve the nature of SMBH and galactic energy exchange are dust-reddened quasars which appear to represent an important evolutionary phase linking galaxy mergers to black hole growth (Glikman et al. 2012, 2013, 2015; Urrutia et al. 2009). As mentioned, one way luminous quasars are thought to be triggered by major mergers (Sanders et al. 1988), during which some gas loses angular momentum and feeds the black hole while shocks trigger a starburst. As the SMBH grows, it begins in a heavily obscured, reddened state from dust and gas followed by a relatively brief transitional phase during which the dust is cleared via feedback mechanisms. Subsequently, an unobscured, blue quasar emerges and dominates the radiation output for the system (Figure 7).

As shown quasars trace galaxy evolution, theorized to be occurring in all galaxies during the early formation of their SMBH or at a later stage. As such, the quasar phenomenon may be short-lived and may occur in most galaxies, or it could be a rare long-lived phase. The physical details of so-called feedback mechanisms as well as AGN models are still not well understood due to heterogeneous search parameters and definitions. Thus, the identification of a population of quasars that are actively influencing their hosts are *highly desirable* as test beds for observing feedback in action.

Red, and the unobscured blue, quasars may be related within an evolutionary sequence that

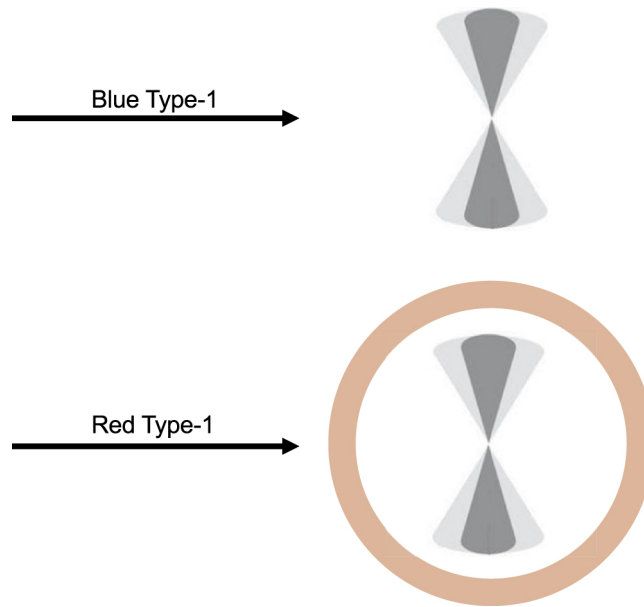


Figure 7: Distinction between Type 1 Red QSOs and Type 1 Blue QSOs following Figure 3. from Glikman et al. 2022. The Red Type-1 QSO has a ‘torus’ of dust surrounding that intrinsically reddens the underlying quasar.

connects dust-obscured star formation with quasar activity through gas inflow via merging galaxies/and outflows from the quasar (Gillette et al. 2023; Glikman et al. 2012; Hopkins et al. 2005; Sanders et al. 1988; Yi et al. 2022). Red quasars can be found in the brief transitional phase between the starburst and the blue quasar phase, during which winds and/or jets drive away the obscuring dust to reveal an unobscured blue quasar, and ultimately shuts down the star formation to form a dormant early-type galaxy. An artist’s rendition of this evolutionary scenario invoked by a galactic merger is shown in Figure 8 adapted by S. Munro. Most importantly, red quasars serve as the sought after test beds for studying how quasars impacts their host galaxies (Glikman et al. 2022).

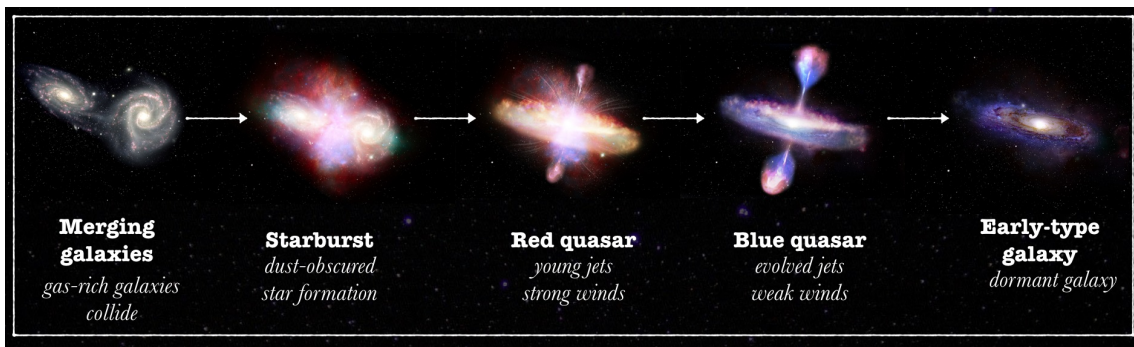


Figure 8: An artist’s impression of the transition from red to blue quasars. Notice the heavy dust enshrouding the middle red quasar. Credits: Gemini Observatory, GMOS-South, NSF; <https://www.pxwall.com/4k-high-definition-galaxy-wallpaper/>; Adapted by S. Munro

Once large radio, mid-IR, and optical samples of QSO’s were gathered, it became apparent that their co-moving space density evolved with redshift, reaching a peak around  $z \sim 2$  (Figure 9;

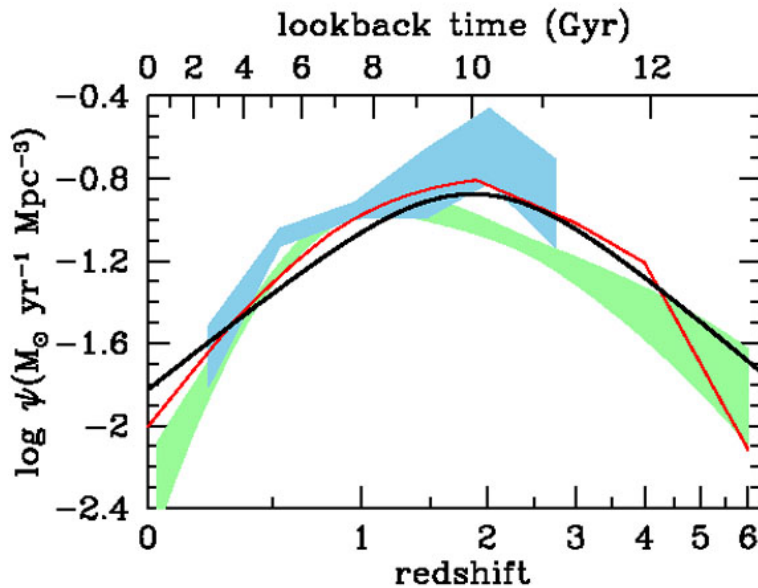


Figure 9: Comparison of the best-fit star formation history (thick solid curve) with the massive black hole accretion history from X-ray [red curve (Madau and Dickinson 2014); light green shading (Aird et al. 2010)] and infrared (light blue shading) (Delvecchio et al. 2014) data. The shading indicates the  $\pm 1\sigma$  uncertainty range on the total bolometric luminosity density.

Glikman et al. 2013; Madau 2014). This motivated the collection of statistically complete samples of quasars which allow the construction of luminosity functions that trace the evolution of the quasar population as a function of luminosity and redshift (Glikman et al. 2018, 2022). Further, to compare between the red and blue quasars statistically complete samples only require samples to  $z \sim 3.5$  (Figure 10), as the K-magnitude is not sensitive to reddened quasars beyond this cutoff. Therefore, a complete census of the space distribution of quasars over a large range in redshift and luminosity can distinguish between these aforementioned models and provide insight into the origin of quasars and their connection to galaxies.

Using the definition of quasars as an unresolved optical source with broad emission lines and blue UV-optical colors, many surveys have been initiated to determine quasar space distributions and demographics. The most fruitful surveys for quasars have been in the optical (Irwin et al. 1991; Pâris et al. 2017). The characteristic blue spectral energy distribution (SED) and stellar morphology allows for efficient selection of quasar candidates, distinguishing them from stars and galaxies (Richards et al. 2006).

Optical surveys for quasars have often exploited the ultraviolet excess (UVX) and power-law nature

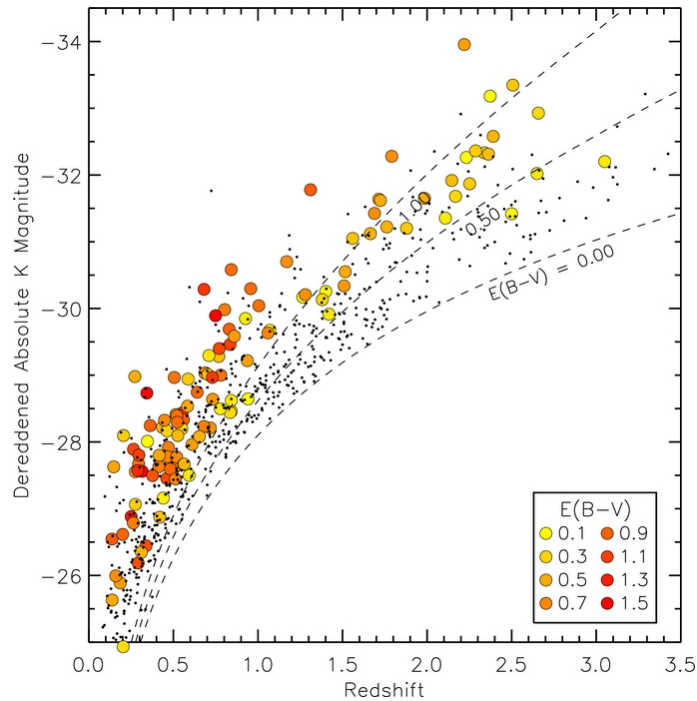


Figure 10: Figure 15 from Glikman et al. (2012) showing the dereddened K-band absolute magnitude as a function of redshift. The colors of the circles correspond to the amount of extinction, ranging from low extinction (yellow) to heavily reddened (red). The dotted lines indicate the survey limit ( $K < 16$ ) for increasing amounts of extinction. The small dots are FBQS-II and FBQS-III quasars, which they assume are unabsorbed. At every redshift, red quasars are the most luminous.

of the typical quasar spectrum (Meyer et al. 2001). Although this UVX method fails for  $z > 2.2$  when  $\text{Ly}\alpha$  shifts into the  $\text{Ly}\alpha$ -band, reddening the observed U - B color, thousands of quasars have been identified with this technique (Rhoads 2001). While all quasars may be intrinsically blue in color (Richards et al. 2003), the presence of dust along the line of sight to a quasar’s central engine will redden the observed spectrum (Glikman et al. 2007; Klindt et al. 2019; Serjeant 1996; Webster et al. 1995). This bias ultimately left out an entire population of dust-reddened QSOs that were seemingly missing.

The highly sought-after red quasars can be elusive because their optical and near-infrared colors resemble those of very abundant low-mass red stars, which are weak radio sources. Thus early works had to construct surveys using radio selection to avoid contamination from other stars (Webster et al. 1995). Results from these studies suggested that red quasars make up a large fraction (up to 80%) of the overall quasar population but had been missed by optical selection methods. Furthermore, quasars that are dimmed because of extinction will drop out of the selection in magnitude-limited optical surveys, further biasing quasar number counts and affecting both the observed quasar luminosity function and its apparent evolution over cosmic time (Glikman et al. 2004).

Speculation has arisen over the years as to the source of the reddening in red quasars. Webster et al.

---

(1995) argued that the reddening in their flat-spectrum quasar sample is due to dust obscuration. However, the case has also been made for a red synchrotron component contributing to the near-infrared flux and causing the red colors in flat-spectrum radio-selected quasars that Webster et al. (1995) studied (Magorrian et al. 1998; Whiting et al. 2001). Other contributions to the spread in colors may come from contamination by host-galaxy starlight (Masci et al. 1998) and/or an intrinsic spread in the optical continuum slope (Richards et al. 2003). All of the previous listed speculations will be put into context in this study.

Part of the reason that these issues are not better understood may be the heterogeneous definitions that have been used to classify quasars as “red.” Traditional samples of red quasars that impose cuts on observed colors or spectral index (e.g. Gregg et al. 1996; Webster et al. 1995) are too heterogeneous with redshift to yield physically homogeneous samples of red quasars. Spectral indexes are sensitive to the choice of continuum windows, and simple color cuts ignore the significant contribution that emission and absorption lines make to the colors of quasars as a function of redshift (Richards et al. 2003). That is not to say that in previous works such red quasar criteria are not reasonable, but rather that care must be taken in the interpretation of such samples after the fact.

In a sample of extremely red quasars (ERQs) found in the Sloan Digital Sky Survey (SDSS; York et al. 2000) without a radio criterion, all of the mid-infrared-brightest and reddest sources are detected in the Faint Images of the Radio Sky at Twenty-Centimeters (FIRST; Becker et al. 1995) survey (Hamann et al. 2017; Ross et al. 2015). More recently, Klindt et al. (2019) and Fawcett (2022) found distinct differences between the radio properties of blue and red SDSS quasars. They find that the redder quasars have a significantly higher detection fraction in FIRST and when stacked, radio quiet red quasars have higher median radio fluxes than an unreddened sample. In addition, red quasars’ radio morphologies are more compact compared with blue quasars. Glikman et al. (2022) also showed that infrared-selected red quasars have different radio properties from blue quasars that are selected in the same way, using a radio-independent selection method that is minimally affected by dust reddening. They remove host-galaxy emission from the spectra (seen in Figure 11) and fit for excess reddening in the residual QSOs, resulting in a Gaussian distribution of colors for unreddened (blue) QSOs, with a tail extending toward heavily reddened (red) QSOs, defined as having  $E(B - V) > 0.25$ . In this thesis, I follow the same procedure to explore the reddening in blue quasars whose selection is described in Section 3.

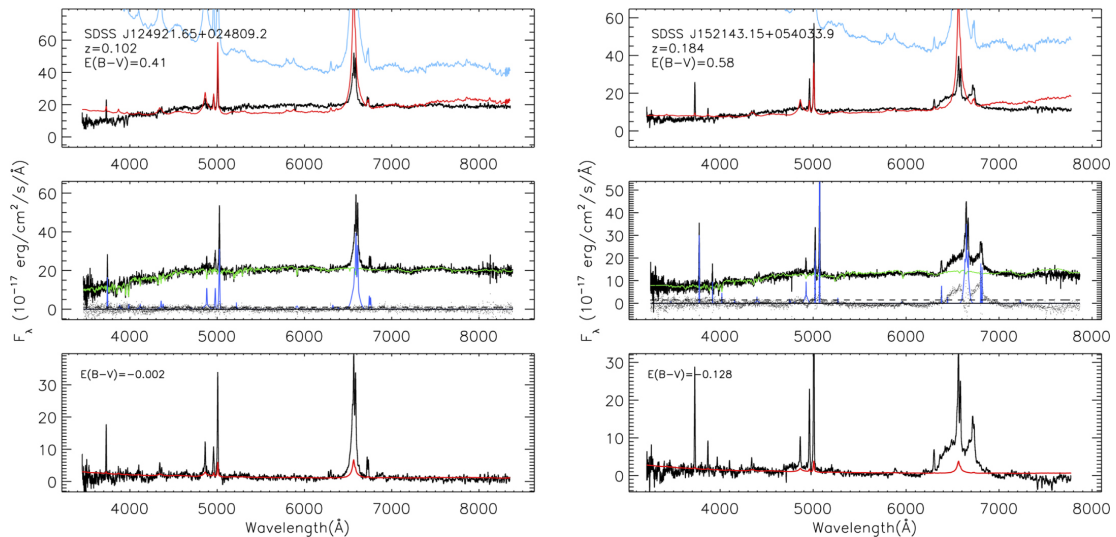


Figure 11: Figure 12 from Glikman et al. (2022) showing examples of two QSO spectra whose host galaxies were fitted with GANDALF (Graphical Astrophysics code for N-body Dynamics And Lagrangian Fluids; Hubber and Rosotti 2016) and subtracted to improve the QSO template fitting process and better estimate the reddening, parameterized by  $E(B - V)$ , experienced by the QSO. The top panel in each column is the original, poor, fit. The black line is the original spectrum. The red line is the best-fit, reddened QSO template and the cyan line is the unreddened QSO template. The middle row shows the fits produced by GANDALF, with the host-galaxy spectrum shown in green, atop the original spectrum in black. The bottom panel shows the galaxy-subtracted spectrum in black and the newly best-fitted reddened QSO template in red. In both examples host-galaxy emission results in artificially large extinctions. We expect similar results in our own sample since subtracting the host-galaxy empirically exposes predominantly unreddened QSOs.

## 1.2 Plan For this Thesis

This thesis focuses on constructing a sample of blue quasars. This will comprise the rigorous construction of an appropriate, well-matched comparison sample to study in relation to the work started by Professor Eilat Glikman and her team in the early 2000s (Glikman et al. 2004, 2007, 2012, 2013) which discovered large numbers of elusive red and blue quasars, using a radio selection requirement. Our aim is to understand the nature of normal, blue quasars so that the dust-reddened, red quasars can be put in context. In this study, we focus on Type 1 sources in both the blue and red samples so as to compare sources with the same approximate distribution of viewing angles, knowing that our line-of-sight is not intersecting the dense clouds of the torus (recall Figures 6 and 7). Here, we aim to construct well-defined red and blue QSO subsamples whose properties can be measured and compared. With a comparable sample of red and blue QSOs, we obtain the fraction of red quasars to give the duration of the overall red quasar phase. Then in the red quasar evolutionary-phase scenario, we want to understand: its duration, the mechanisms of dust-clearing, and radio emission properties. We study the reddening properties of the QSOs and use that information to determine the sample's de-reddened absolute magnitudes to ensure the two samples are intrinsically similar. Furthermore, we compare the radio properties

---

of the fraction of QSOs which may lead to an evolutionary explanation.

Luminosity functions derived for previous optical quasar surveys show a steep increase in the number of quasars with increasing magnitude. For  $M_B \leq -23$  the shape of the luminosity function is best approximated by a power law,  $\Phi(L, z) \propto L^\alpha$ , where the slope,  $\alpha$ , ranges between -3 and -4 depending on the survey (Boyle et al. 1988). This implied a factor of 4 to 6 increase in the number of quasars per cubic megaparsec per half-magnitude (Croom et al. 2004). Thus, by increasing the magnitude limit of our sample to include fainter objects we will be able to find more quasars to study. Utilizing a combination of radio, optical, and mid-infrared surveys, to attempt to avoid the blue-color biases of UVX surveys, we employ a multi-color selection technique allowing for the detection of red and blue objects to  $z \sim 3$ .

In the following Section 2, we explain our sample selection search parameters utilizing radio, infrared, and optical wavelengths. In Section 3 we explain our data matching and eliminate all narrow-line sources which will form the blue comparison sample. In Section 4.1 we fit our sample's spectra to complete a spectroscopic analysis of 1403 blue quasars with the Bayesian AGN Decomposition Analysis for SDSS Spectra (BADASS; Sexton et al. 2020). In Sections 5.1 and 5.2 we study the fraction of red quasars as a function of luminosity and redshift, and lastly we begin in Section 5 discussing the radio emitting properties and accretion properties of our sample in the context of previous works. We conclude our study's investigation in Section 6.

## 2 Sample Selection

Glikman et al. (2004) combined the Faint Images of the Radio Sky at Twenty-centimeters (FIRST; Becker et al. 1995) radio survey and 2 Micron All Sky Survey (2MASS; Skrutskie et al. (2006)) to develop an efficient selection method for finding the previously missed red quasars. The combined survey (F2M) found large numbers of red quasars, but was very shallow, reaching only the 2MASS limit of  $K \approx 15.5$  magnitude. Additionally, because the F2M survey used radio selection, those red quasars belong to the rarer radio-loud and radio-intermediate populations that only make up  $\sim 10\%$  of the overall quasar population. Assuming that radio emission from these quasars is unrelated to their surrounding dust, one could extend the F2M results to the entire quasar population. However, if the radio emission and reddening are not independent, then any conclusions about the red quasar population derived from the F2M sample, such as the duration of the transitional phase, could be biased and does not apply to the full quasar population.

Due to this potential radio bias, Glikman et al. (2013) chose to search for faint red quasars in

---

an equatorial region of sky spanning  $9\text{h} < \alpha < 15\text{h } 40\text{m}$  in right ascension, and  $-5 < \delta < 15$  in declination, where known low-redshift, high luminosity quasars have been studied (Karhunen et al. 2014). The area covered by this region amounts to  $190 \text{ deg}^2$ . Following Glikman et al. (2013) we utilize all FIRST sources spanning  $9\text{h} < \alpha < 15\text{h } 40\text{m}$  in right ascension, and  $-5 < \delta < 15$  in declination. There are 172,980 FIRST sources in the 2012 February 16 catalog that lay within the survey boundaries described above.

As discussed, mid-infrared and infrared wavelengths allow astronomers to peer through dusty regions of space. As such, we include the Wide-Field Infrared Space Explorer (WISE; Wright et al. 2010), providing the infrared fluxes needed for identifying reddened luminous QSOs. Many other studies (Assef et al. 2013, 2018; Jarrett et al. 2011; Mateos et al. 2012; Stern et al. 2012) have made use of mid-IR used by WISE as the survey is an excellent wavelength region of constraining QSOs, thus we follow similarly.

Glikman et al. (2013) found that reddened quasars exist in the same region of infrared color-color space as normal, unreddened quasars. We follow the formalism from Glikman et al. (2013) matching FIRST sources in the survey area outlined previously to the AllWISE Catalog<sup>6</sup>.

However, another limiting factor to our search is at higher redshifts ( $z > 1.5$ ), only the most intrinsically luminous objects are seen. To reach the heavily reddened higher-redshift analogs to the F2M quasars, a more sensitive near-IR survey is needed to tease out the luminosity and redshift dependencies of red quasars. The ideal survey for extending the F2M red quasar survey naturally was the UKIRT Infrared Deep Sky Survey (UKIDSS; Lawrence et al. (2007)). Therefore, we also impose K-band magnitude flux limit of  $K < 17$ . This results in 25,619 sources.

To create a robust sample containing our source’s optical magnitudes, we then matched these objects, using the FIRST position, SDSS DR18 catalog with a search radius of  $2''$ . Using this sample (as seen in Figure 12), we present a UVX-bias-independent selection criterion for red quasars that allows for better classification of the types (and causes) of red quasars, which, in turn, will lead to a better census of the quasar population in the future. The purpose of this project is to measure the characteristics of a sample of unreddened quasars in the SDSS that serve as the comparison sample to red quasars found in the same region. In this study, we will investigate the fraction between the red and blue quasars to constrain the duration of the red quasar phase.

---

<sup>6</sup>The AllWISE Catalog (Cutri et al. 2021) is an extension of WISE matching within  $2''$  and imposing the color cuts  $0.5 < [3.4] - [4.6] <$  and  $2 < [4.6] - [12] < 4.5$  (on the Vega photometric system) to probe low-redshift, luminous quasars 13.

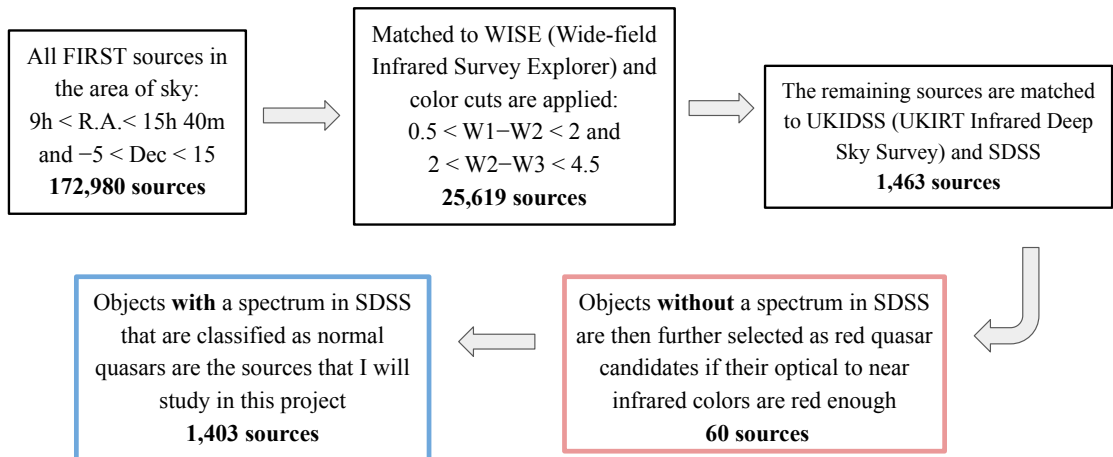


Figure 12: Flowchart summarizing the sample selection for this thesis research project.

## 2.1 Radio Selection with FIRST

Given new methods of detecting quasars, constructing statistically complete samples over the years provided better estimates of the percentage between quasars that are radio-loud and quasars that are radio-quiet. The FIRST survey (Becker et al. 1995) mapped 9000 deg<sup>2</sup> of the sky at 20 cm using the Very Large Array (VLA) in the B configuration. Coverage includes 8400 deg<sup>2</sup> in the north Galactic cap and 600 deg<sup>2</sup> in the south Galactic cap. With the array in this configuration, the survey is roughly analogous to all-sky optical surveys, with 5" resolution and 0.500" sub-arcsecond positional accuracy. Requiring a FIRST detection in our quasar selection minimizes contamination from low mass stars whose optical-to-near-infrared colors overlap those of reddened quasars. Additionally, the FIRST survey reaches a flux density limit of 1 mJy over a quarter of the sky and provides a means of eliminating nearly all Galactic sources from the candidate list.

Glikman et al. (2004) combined FIRST and an all-sky near-infrared (NIR) survey (2MASS; Skrutskie et al. 2006) to develop an efficient selection method for finding these missed red quasars. Subsequent work identified  $\sim 130$  dust-reddened quasars via the same method (hereafter referred to as F2M quasars; Glikman et al. 2004, 2007, 2012; Urrutia et al. 2009) that have broad emission lines and are moderately obscured by reddening ( $0.1 < E(B - V) < 1.5$ ) spanning a broad range of redshifts ( $0.1 < z < 3$ ). Follow up studies of F2M quasars showed that they are accreting with very high Eddington rates (Kim et al. 2015; Urrutia et al. 2012), are overwhelmingly in merger-dominated systems (Glikman et al. 2015; Urrutia et al. 2008), and often have broad absorption lines that are typically associated with outflows and feedback (Glikman et al. 2012; Urrutia et al. 2009).

---

This body of evidence suggests that red quasars are merger-induced systems, in a transitional phase, emerging from their shrouded environments, as predicted by the galaxy merger simulations (refer to Figure 8). Based on the initial statistical frequency of F2M red sources, compared with optically selected, blue quasars, Glikman et al. (2012) estimates that the duration of the red phase is  $\sim 20\%$  the length of the unobscured quasar lifetime, further situating the red population as the perfect test-bed to capture galactic evolution in-action.

## 2.2 Infrared Selection with WISE

As Glikman et al. (2012) and others established, we continue our survey selection process from the radio to the infrared building a robust comparison sample. We utilize the Wide-Field Infrared Space Explorer (WISE; Wright et al. 2010), which scanned the entire sky at 3.4, 4.6, 12, and 22  $\mu\text{m}$  down to flux densities of 0.08, 0.11, 1, and 6 mJy, respectively, providing the wide-area coverage needed for identifying large numbers of luminous QSOs. The angular resolution is 6.1", 6.4", 6.5", and 12.0" at 3.4, 4.6, 12, and 22 $\mu\text{m}$ , and the astrometric precision for high signal-to-noise sources is better than 0.15". The most extensive searches for red AGNs had been based on the 2MASS survey (Skrutskie et al. 2006), using either near-infrared color selection or combination with mid- and far-infrared and radio measurements (Glikman et al. 2004, 2007, 2012). WISE goes a magnitude deeper than the 2MASS Ks data in 3.4  $\mu\text{m}$  for sources with spectra close to that of an A0 star, and even deeper for moderately red sources like K stars or galaxies with old stellar populations. Many classes of extragalactic objects will be quite red in the WISE colors, as will brown dwarf stars which are among the Sun's closest neighbors. Furthermore, WISE characterized and probed fully the extent of the population of obscured AGNs and provided a highly uniform set of mid-infrared photometry for virtually all known AGNs and QSOs at the time.

In 2010, most of what was known about the properties and evolution of AGNs and QSOs had been deduced from studies of objects discovered in ultraviolet-excess and optical emission line surveys creating a steep bias towards this selection method. However both infrared and radio surveys, as previously discussed, reveal that many AGNs in the universe have remained hidden from short-wavelength surveys because of reddening and obscuration by dust in and around their nuclei (Webster et al. 1995). But in WISE color-color space, QSOs can be isolated from stars and other extragalactic sources (see Figure 13), making the mid-IR an excellent wavelength region for our search purposes (Assef et al. 2013, 2018; Jarrett et al. 2011; Mateos et al. 2012; Stern et al. 2012). As in Glikman et al. (2012), we combine the FIRST survey with WISE to discard any reddened brown dwarf stars, low-mass stars, and non-AGN galaxies.

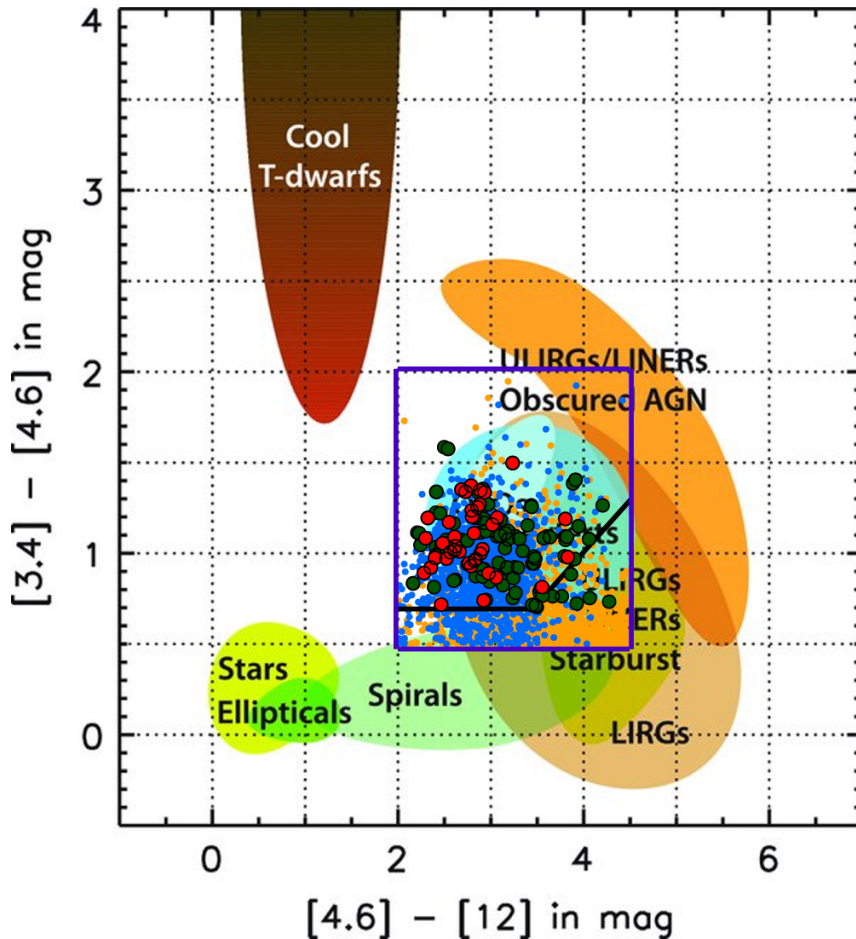


Figure 13: Glikman et al. (2022) reproduced Figure 12 from Wright et al. (2010) showing the location of various astrophysical objects in WISE color-color space. Over-plotted is a box that outlines the initial selection region with thick purple solid lines and plots within the box sources with SDSS spectra identified as QSO (blue circles) and GALAXY (orange circles). Also plotted are the selected red-quasar candidates with large outlined circles. Newly confirmed QSOs are filled red and sources that are not obviously QSOs are filled green. The black solid line shows our refined color cuts selection criterion that avoids significant contamination from non-QSOs (2).

### 2.3 Near-Infrared Selection with UKIDSS

The UKIRT Infrared Deep Sky Survey (UKIDSS; Lawrence et al. 2007) does not cover the whole sky, but is significantly deeper than the Two-Micron All-Sky Survey (2MASS; Skrutskie et al. 2006). It is in fact not a single survey but a survey program combining a set of five survey components of complementary combinations of various depths and cover area. The largest of these, the Large Area Survey (LAS), covered  $\sim 3000 \text{ deg}^2$  in the Y, J, H, and K bands down to  $K \sim 18 \text{ mag}$ , which is approximately 2.5 mag deeper than 2MASS. The deep K-band limit provided by UKIDSS allows for finding more heavily reddened quasars at higher redshifts as compared with previous work using FIRST and 2MASS (Glikman et al. 2004, 2007, 2012). The survey uses the Wide Field Camera (WFCAM) on the 3.8-m United Kingdom Infrared Telescope (UKIRT). WFCAM has an instantaneous field of view of  $0.21 \text{ deg}^2$ , considerably larger than any previous IR camera on a

---

4-m class telescope, along with a pixel size of 0.4 arcsec. The combination of large telescope, large field of view, and good image quality, makes possible a survey of considerably greater scope than that of 2MASS. In addition, the image quality of UKIDSS is comparable to optical CCD-based surveys, with a typical FWHM of the point-spread function (PSF) below an arcsecond (compared with FWHM of 2 for 2MASS point sources). Thus, utilizing UKIDSS in our selection offers a powerful mid-IR search method extending beyond 2MASS and F2M combined. Such that, there were 15,954 FIRST+WISE+UKIDSS sources, of which 5403 have  $K < 17.3$  mag.

## 2.4 Optical Selection with SDSS

We continue our survey matching such that the entirety of the blue quasar spectroscopic sample can be found from the Sloan Digital Sky Survey (SDSS, York et al. 2000), an all-sky spectroscopic and imaging observation program. The SDSS is one of the largest, most-cited astronomical surveys that comprehensively maps over a third of the sky (Frogel 2010). Over the past 25 years the SDSS has contributed to expanding our understanding of the large-scale evolution and structure of the universe, the formation of stars and galaxies, the history of the Milky Way, the nature of SMBH, and the science behind dark energy. The first rounds of operation began in 2000 until 2008 (SDSS-I, 2000-2005<sup>7</sup>; SDSS-II, 2005-2008<sup>8</sup>), it obtained deep, multi-color images covering more than a quarter of the sky containing more than 930,000 galaxies and more than 120,000 quasars. SDSS data has been continuously released to the scientific community as well as to the public through annual data releases. The first rounds of SDSS public data release papers (Abazajian et al. 2003, 2004, 2005; Abazajian et al. 2009; Adelman-McCarthy et al. 2006, 2007, 2008; Stoughton et al. 2002), hereafter DR1, DR2, DR3, DR4, DR5, DR6, DR7, respectively, have been cited in well-over ten thousand referred papers for studies ranging from galactic dynamics to the discovery of the most distant quasars at the time using spectroscopy. Most importantly, the advent of the CCD-based SDSS extended wide-area surveys to longer wavelengths with the inclusion of the i- and z-bands, enabling searches for quasars based on i - z colour and extended redshifts of  $z \sim 6$  were reached (Stoughton et al. 2002; Venemans et al. 2007). This was especially important to the study of QSOs in relation to this study because redshifts in which the host-galaxy light no longer interacted with the quasar spectrum were abundant.

We match the FIRST+WISE+UKIDSS sources to the SDSS catalog (UKFS+W; see Appendix Section A and Section 3 for more details). Objects without a spectrum in SDSS are then further selected as red quasar candidates if their optical to near infrared colors are red enough, these

---

<sup>7</sup>Abazajian et al. 2003

<sup>8</sup>Abazajian et al. 2009

---

sources are being followed up by Eilat Glikman and her team. Objects with a spectrum in SDSS that are classified as quasars are the blue-selected sample that I study in this thesis.

### 3 QSOs in SDSS

We employ the SDSS Science Archive Server (SAS) DR18 (Almeida et al. 2023) to download the spectra associated with our sample’s right ascension and declination values. We employ the SDSS Sky Server Cross Match Tool and run a spectroscopic cross-match SQL query on the data list of RA/Dec. Refer to the Appendix Section A for cross-matching details. All spectroscopic sources that have been matched in the SDSS are added to our full sample,  $UKFS + W$ .

As noted in Glikman et al. (2018), among the spectra that SDSS classifies as **QSO** there are sources that only show narrow emission lines (Type 2). If we include Type 2 sources in the sample, it becomes more challenging to determine the location and nature of the obscuring material (recall Figure 6). Therefore, focusing exclusively on broad-line sources (Type 1) allows us to directly compare the blue and red populations. As the canonical definition of a broad-line quasar requires having line widths  $> 1000 \text{ km s}^{-1}$  (Glikman et al. 2004, 2012; Gregg et al. 1996; Schneider et al. 2003), our sample will focus on all objects with line widths broader than  $1000 \text{ km s}^{-1}$ .

To eliminate the Type 2 QSOs, we first utilize the AGN Line Profile And Kinematics Archive (ALPAKA) catalog (Mullaney et al. 2013) which provides detailed line analysis for 25,670 AGN with spectra in SDSS DR7. The spectra of these sources were fitted with multi-component Gaussians to study their kinematics and Eddington ratios. Line fitting was performed on [O III] 4959 Å, [O III] 5007 Å, [N II] 6548 Å,  $H\alpha$ , and [N II] 6584 Å, including a broad component for forbidden species and an additional broad component for permitted species, if warranted. The ALPAKA sample is limited to  $z \leq 0.4$  in order not to lose  $H\alpha$  beyond the SDSS spectroscopic wavelength limit of 9000 Å. We matched our QSO sample to the ALPAKA catalog and found 112 matches within 2 arcseconds which we use to examine line-widths and select broad-line sources.

The ALPAKA catalog classifies sources as Type 1 when the broad component of their  $H\alpha$  and  $H\beta$  line constitutes  $\geq 50\%$  of the total line flux and a  $600 \text{ km s}^{-1}$  threshold (Mullaney et al. 2013). However, we impose an additional requirement that the broad component have a Full Width at Half Maximum (FWHM) velocity,  $v_{FWHM} \geq 1000 \text{ km s}^{-1}$ ; 33 sources obey this criteria. Additionally, we also exclude any source not classified as a Type 1 in the ALPAKA catalog; 27 sources obey this criteria. We call these 27 sources Type 1 broad line AGN matches from ALPAKA.

For the 1291 remaining AGN without line analysis in ALPAKA, we utilize the batch-downloaded

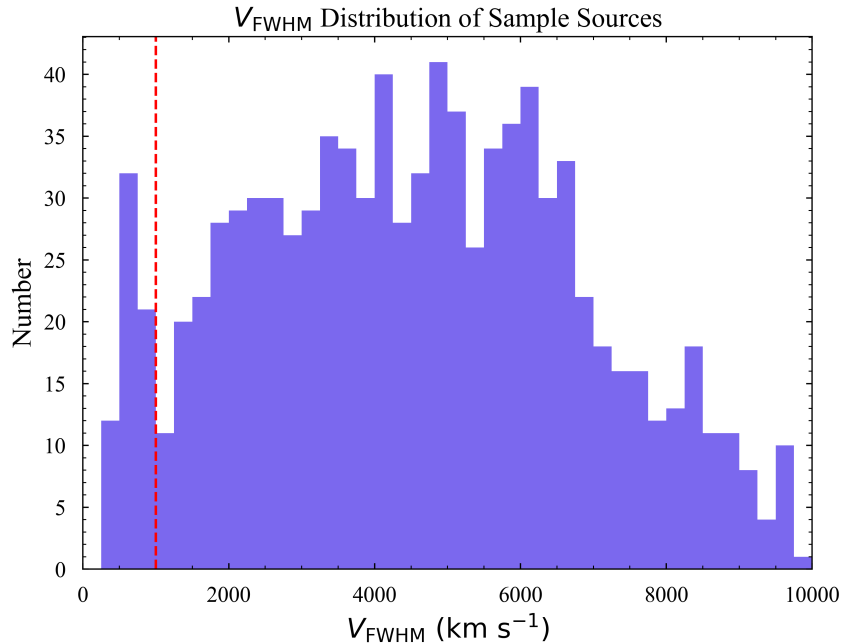


Figure 14: The  $v_{FWHM}$  distribution of our sample sources. The red dashed line at  $v_{FWHM} = 1000$   $\text{km s}^{-1}$  marks required criteria for a Type 1, broad line QSO.

spectra via SAS web interface and used the value-added measurements provided in their multi extension FITS headers to further reduce the size of the SDSS QSO sample by examining the distribution of their maximum emission-line-width. We examined the emission-line fits performed on the SDSS spectra through DR18 (Bolton et al. 2012). Single-component Gaussians were fitted to common UV and optical emission lines for all the spectra, tying the Balmer line widths to each other. Forbidden line widths are also tied to each other and fitted with a separate Gaussian. These are provided in the third extension of the FITS tables (Bolton et al. 2012, for details). The line widths are reported in terms of the Gaussian  $\sigma$  parameter, which we convert to a FWHM velocity,  $v_{FWHM} = 2.355\sigma$ . Figure 14 shows the FWHM distribution of the broadest line component in each spectrum (blue line) where  $v_{FWHM} = 1000$   $\text{km s}^{-1}$  is shown with a vertical red line. Seventy-five sources fail this criterion, seen in Figure 14 below the red-dashed line. All sources QSO sources above this requirement satisfy the broad line (Type 1) quasar definition (Shen and Kelly 2012). Thus, we find 1216 objects with  $v_{FWHM}$  greater than  $1000$   $\text{km s}^{-1}$  and call this the broad line QSO sample.

Therefore, together with the ALPAKA-line-width-selected sources, our QSO sample contains 1,243 (27 + 1216) broad-line QSOs with SDSS spectra. Figure 15 shows a flowchart of the process. All sources selected as Type 1 QSOs are further investigated by their SDSS assigned redshift.

---

Type I Selection Flowchart:

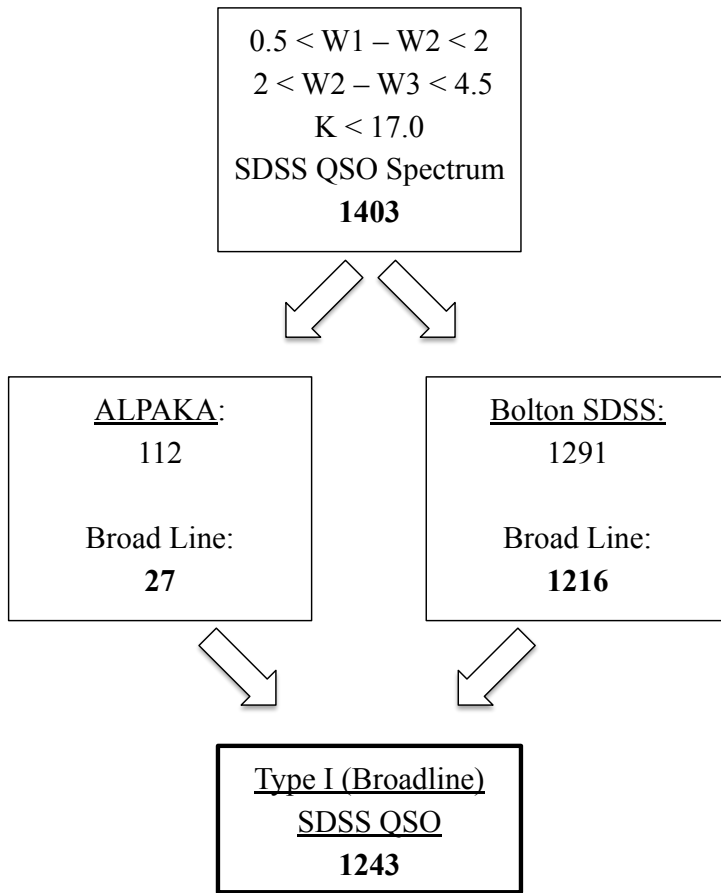


Figure 15: Broad line (Type I) QSO sample selection process.

### 3.1 Erroneous Redshifts

We visually examined all the spectra that obeyed the broad-line criterion and identified three sources with erroneous redshifts. We also identified and removed another five sources whose spectra were featureless, with no discernible emission lines, suggesting an error in the automated line analysis for these spectra and one spectrum that was identified as a star.

The remaining sources with erroneous redshifts need a “by hand” adjustment, because the SDSS pipeline often thinks that [OIII] at  $5007\text{\AA}$  is  $\text{Ly}\alpha$  at  $1216\text{\AA}$  thus giving moderate redshift sources way-too-large redshifts. We further limit our sample based upon the QSO K-magnitude-Redshift relation, as mentioned in Section 1.1.7 and shown in Figure 8, by requiring  $z < 3.5$ .

This leaves 1179 broad-line QSOs that we use to complete our QSO sample. The entire full-sample redshift distribution can be seen in Figure 16.

Lastly, we divide the Type 1 QSO sample by high and low redshift such that we have 309 sources

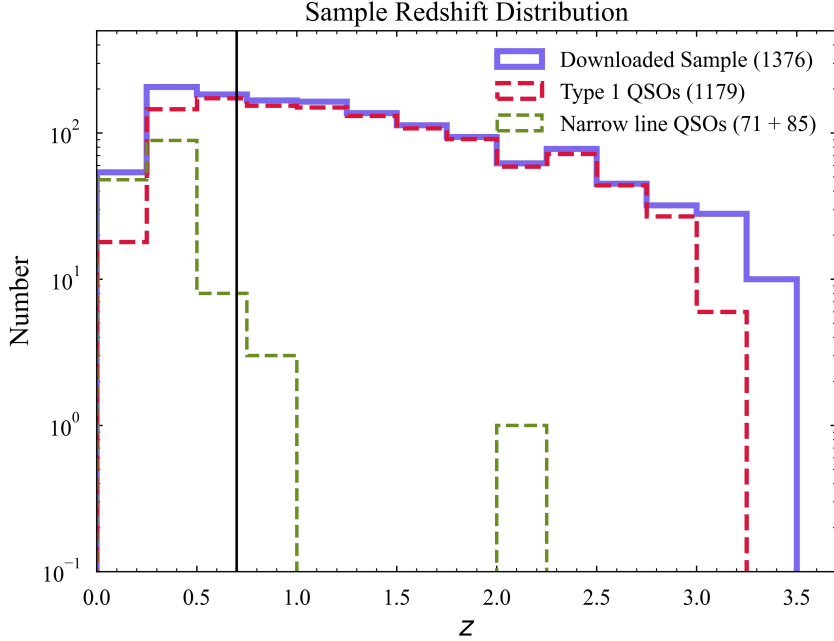


Figure 16: Redshift ( $z$ ) Full Sample Distribution (blue) with Type I (red) sources we include and the narrow-line sources we eliminate from the sample (green). We implement our redshift cutoff, of  $z < 3.5$ .

with redshift  $> 0.7$  and 870 sources with redshift  $< 0.7$ , as represented by the solid black line at  $z = 0.7$  in Figure 16. We implement this cut at  $z = 0.7$  since above this limit SDSS becomes insensitive to most galaxies, such that when an AGN spectrum is recorded the host-galaxy light is insignificant. Further, at high redshifts when  $H\alpha$  is shifted beyond observable wavelengths of the spectrum, line fitting procedures do not run as successfully. Since we are interested in quantifying how the host-galaxy light affects the QSO spectra, we thus complete a spectroscopic analysis on the 309 sources with redshift  $z \leq 0.7$ . We then separately consider these 870 sources with  $z \geq 0.7$  and directly analyze the SDSS QSO spectrum.

## 4 Dust Reddening Investigation

We obtain Initial (“Before”)  $E(B - V)$  values from the reddening code produced by Jack Klawitter at Middlebury College for his senior project (Klawitter 2023). We fit a QSO template to each SDSS spectrum, following the formalism described in Glikman et al. (2007) using equation 22 and plot the distribution of Initial  $E(B - V)$  values for our total sample in Figure 17.

The distributions overall appears as a Gaussian (black curve; fitted to the data with  $E(B - V) < 0.1$ ), peaked at  $E(B - V) \sim 0$  with a broad tail extending toward redder colors (example spectra is shown in Figure 18). The Gaussian distribution is attributed to an intrinsic spread of the power-law

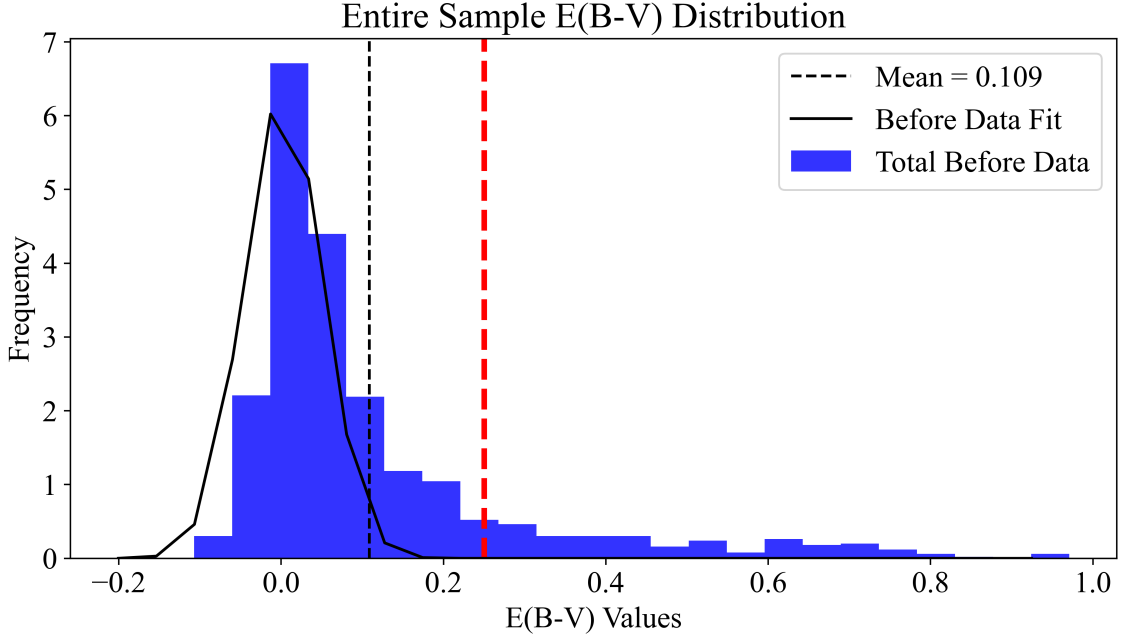


Figure 17: Distribution of the initial  $E(B - V)$  values for the SDSS QSOs, which we determined by fitting a QSO template to each spectrum are shown in the blue for the entire sample. The vertical red dashed line at  $E(B - V) = 0.25$  is our defined limit for a QSO to be considered dust-reddened. As shown, there extends a significant tail of reddened QSOs which we investigate further in Section 4.2. The distribution of initial  $E(B - V)$  values below this reddened limit is however already centered on  $E(B - V) = 0$  shown in dark blue and fitted with a black Gaussian curve. The mean, centered at  $E(B - V) = 0.109$ , is shown in the black dashed line.

continuum slope of un-reddened quasars. The distribution of  $E(B - V)$  for low redshift SDSS QSOs is skewed towards  $E(B - V) = 0.26$  shown as the orange distribution in 19. The tail extending to higher  $E(B - V)$  values is partially due to dust-reddening, but predominantly due to host-galaxy contamination for the low-redshift sample. This was pointed out earlier by Richards et al. (2002) when examining the relative  $(g - i)$  colors of SDSS QSOs in an early data release of the SDSS survey. Hence, the distribution of  $E(B - V)$  for the SDSS QSOs after subtracting host-galaxy light will subsequently shift to be well-fit by a Gaussian distribution centered on  $E(B - V) = 0$ . In this study, since our aim is to quantify how the host-galaxy’s light is affecting that of the quasar, we require the host-galaxy’s emission model fit, as well as the AGN continuum. We discuss the removal of host-galaxy emission in the following Section 4.1 and investigate the high-redshift, highly-reddened sources in Section 4.2.

#### 4.1 BADASS: Removal of Host-Galaxy Emission

Lower luminosity AGN may have redder colors as a result of added light from a host-galaxy rather than reddening of the AGN continuum, so we model the host-galaxy simultaneously with Gaussian profiles fitted to specified emission lines to the  $z < 0.7$  objects with SDSS spectra. We do not take

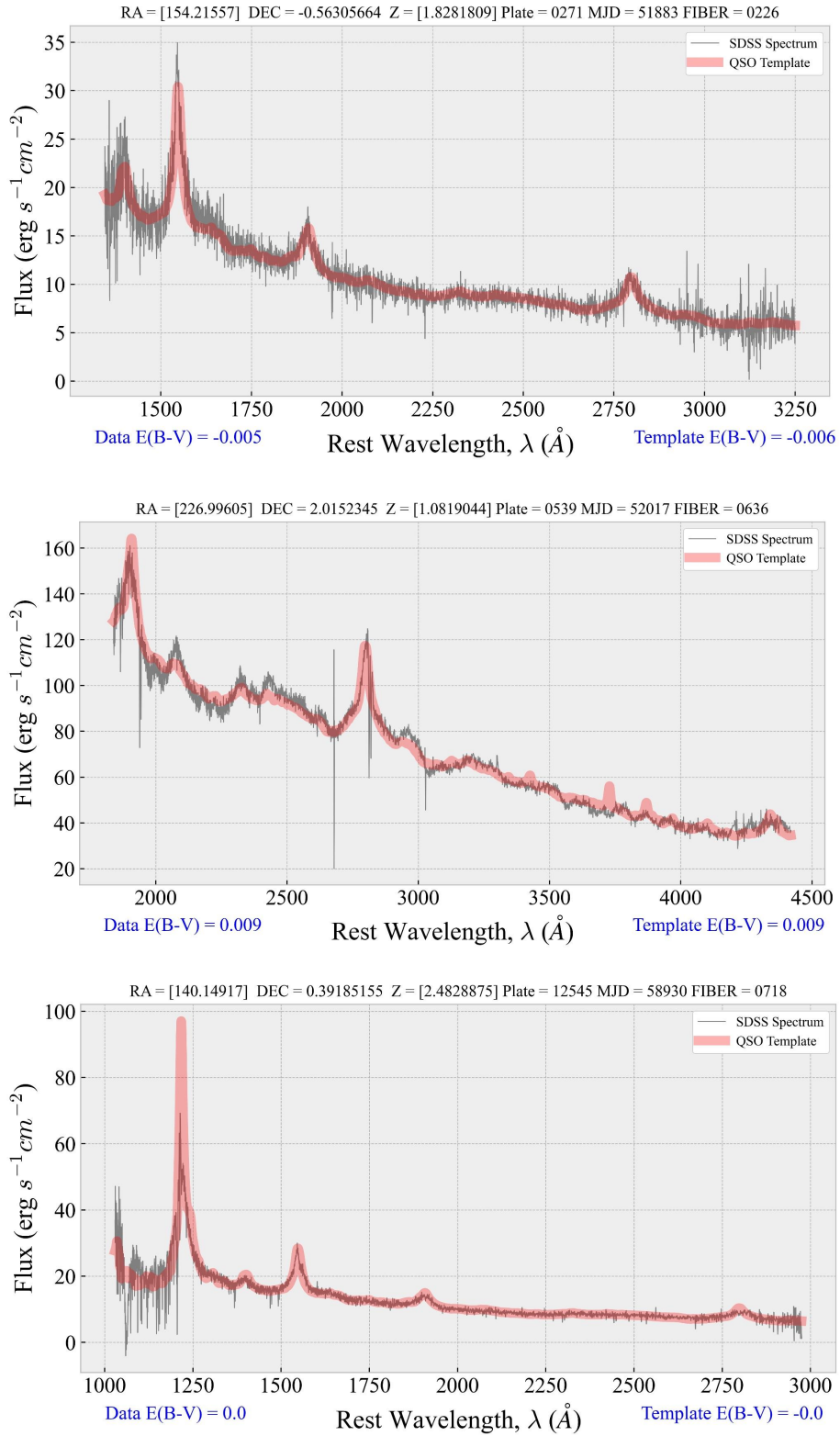


Figure 18: Example SDSS spectra of a high redshift ( $z > 0.7$ ) source with  $E(B - V) \sim 0.0$ . Each spectra is well-fit by a QSO template shown in red.

into account the host-galaxy light from sources with  $z > 0.7$ , primarily due to the fact that at such far distances the host galaxy light in comparison to the quasar spectrum will be dim. Also, since

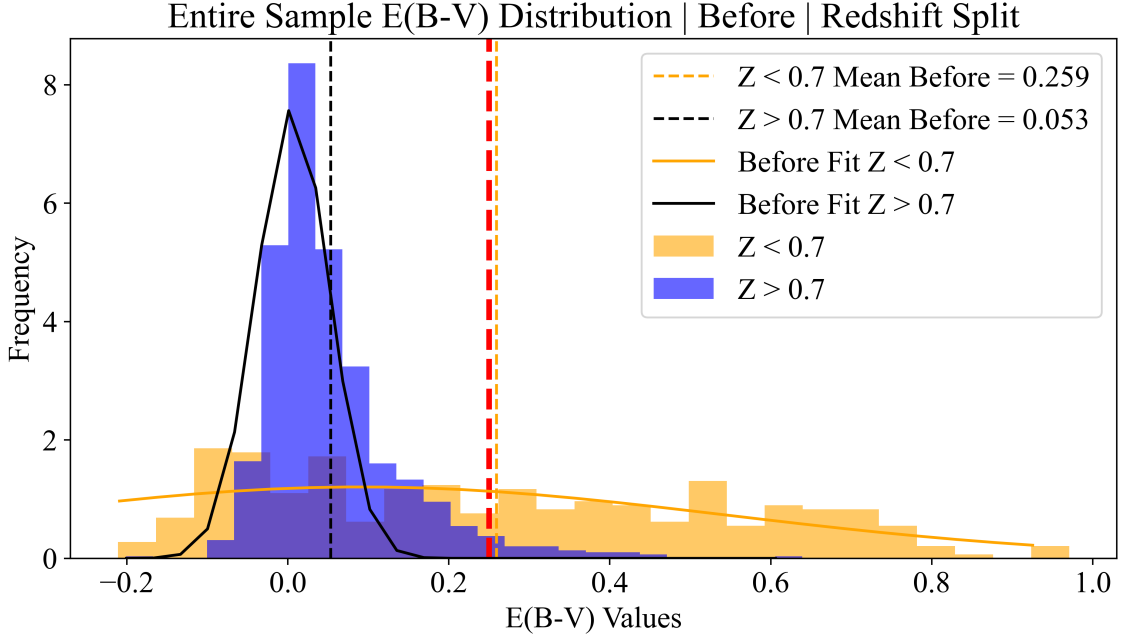


Figure 19: Distribution of the initial  $E(B - V)$  values for the SDSS QSOs, which we determined by fitting a QSO template to each spectrum are shown in the red for the entire sample. We further split the sample by high and low redshift. The distribution of initial  $E(B - V)$  values for high redshift SDSS QSOs is already centered on  $E(B - V) = 0$  shown in blue and fitted with a gray Gaussian curve. The vertical red dashed line at  $E(B - V) = 0.25$  is our defined limit for a QSO to be considered dust-reddened. As shown by the orange distribution and orange Gaussian curve fitted to the initial incorrect  $E(B - V)$  values for low redshift SDSS QSOs they consist of much higher reddening values centered at  $E(B - V) = 0.26$ . These sources are predominantly responsible for the excess reddening tail and require host-galaxy subtraction from their spectra.

the  $H\alpha$  emission line from the galaxy will be shifted beyond observation in optical spectra and line-fitting codes have a hard time with these sources.

We fit the optical lines in each SDSS spectrum by using Bayesian AGN Decomposition Analysis for SDSS Spectra (BADASS; Sexton et al. 2021), a spectral analysis tool designed for detailed decomposition of SDSS spectra, and specifically designed for the fitting of Type 1 (“broad line”) AGN in the optical. We choose BADASS over BADASS’s predecessor: the Gas AND Absorption Line Fitting code (GANDALF; Hamann et al. 2017) which was an IDL based code that was the basis to PyQSOFit which is a relatively new Python code to fit the spectrum of a quasar, and was originally translated from Yue Shen’s IDL code (Guo et al. 2018). We move forward with using BADASS to fit the QSO sample because BADASS produces a number of different outputs for the user at the end of the fitting process—making the output files accessible and manageable. Additionally, as a Python based code we easily implement BADASS’s fitting procedure and modify its outputs for our desires, whereas PyQSOFit was found to be more difficult at the user-interface when modifying the back-end for required outputs. BADASS also allows for a number of model fit components that we implement in our study.

---

In fact, BADASS fits the following spectral features:

- Stellar line-of-sight velocity distribution (LOSVD) using Penalized Pixel-Fitting (pPXF, Cappellari 2017) using templates from the Indo-U.S. Library of Coudé Feed Stellar Spectra (Valdes et al. 2004) in the optical region 3460 Å - 9464 Å. The code uses this data to fit a host-galaxy template using single-stellar population templates from the EMILES library.
- Broad and Narrow FeII emission features using the FeII templates from Valdes et al. (2004) or Kovačević et al. (2010).
- UV iron template from Vestergaard and Wilkes (2001).
- Individual narrow, broad, and/or absorption line features.
- AGN power-law continuum and Balmer pseudo-continuum.
- “Blue-wing” outflow emission components found in narrow-line emission.

All spectral components can be turned off and on via the Jupyter Notebook interface, from which all fitting options can be easily changed to fit non-AGN-host galaxies, or even stars. BADASS uses multiprocessing to fit multiple spectra simultaneously depending on the computer’s hardware configuration. The code was originally written in Python 2.7 to fit Keck Low-Resolution Imaging Spectrometer (LRIS) data, but because BADASS is open-source and not written in an expensive proprietary language, one can easily contribute to or modify the code to fit data from other instruments. Out of the box, BADASS fits SDSS spectra, MANGA IFU cube data, and examples are provided for fitting user-input spectra of any instrument (Sexton 2021), as well as a case-study of ionized gas outflows, is given in Sexton et al. (2023).

We implement the BADASS code with the fitting options set to the default, except turning on the host-galaxy fit and turning off Markov-Chain Monte Carlo (MCMC) sampler, due to time constraints. We examined the fits and subtract the best-fit host-galaxy model from the spectra when a good fit is achieved (i.e., the galaxy continuum traces stellar absorption features around 4000Å). We include the maximum likelihood fitting region output plot produced by BADASS, with moderate plot display style modifications for the purpose of this thesis, shown by an example in Figure 20 for SDSS object with RA, Dec: (0.6050577, 0.30628625) and a redshift,  $z = 0.6050577$ .

We utilize BADASS’s `fit host` feature to remove host-galaxy emission from the spectra and fit for excess reddening in the residual QSOs. Figure 21 shows representative examples of a host-galaxy spectrum interacting with the QSO model spectrum and thus require host-galaxy subtraction to reveal an intrinsically blue quasar which had previously appeared red due to contamination from

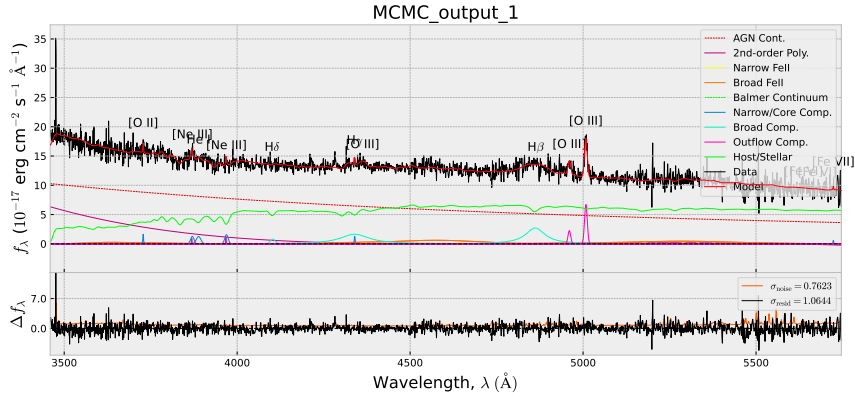


Figure 20: This figure shows the data, model, residuals, and best-fit components, to visually ascertain the quality of the fit to SDSS object (0.6050577, 0.30628625) with a redshift,  $z = 0.6050577$ . The red line shown is the model fit to the QSO spectrum, the green line is the host-galaxy/stellar component fit, and other line-fitting components can be seen in the legend.

the host-galaxy’s emission. The initial reddening code was run on the SDSS recorded wavelength and flux values, this  $\langle E(B - V) \rangle_{Before}$  value is shown on the left side of Figure 21, shown in red if  $\langle E(B - V) \rangle_{Before} > 0.25$ , and blue otherwise. Then, the reddening code was run on the **Data - Host** fits to obtain the value of  $\langle E(B - V) \rangle_{After}$  as shown on the right side of Figure 21, in blue if  $\langle E(B - V) \rangle_{After} < 0.25$ , and red otherwise.

We re-fit all galaxy-subtracted AGN spectra with the QSO template to minimize host-galaxy effects on our  $E(B - V)$  estimates. Figure 22 shows this improved distribution in blue for the entire sample. From the total low redshift subsample of AGN ( $z < 0.7$ ), removing the host-galaxy light from the spectra results in an AGN spectrum with little reddening ( $E(B - V)_{After} < 0.25$ , i.e. defined as blue quasars still with moderate reddening) in 68% (211) of our sample and low-to-zero ( $E(B - V)_{After} < 0.1$ , i.e. defined as blue with nearly no reddening) reddening in 58% (178) of our sample. The galaxy-subtracted AGN reddening distribution is now symmetric and well-fit by a slightly broader Gaussian, however still centered at  $E(B - V)_{After} \sim 0.1$  leading to reason that these low redshift QSOs are still moderately-reddened. We investigate the source of this reddening as caused by the radio-selection bias of our sample in Section 5.

The fact that host-galaxy removal shifts the QSO subsample to agree with the full sample (including  $z > 0.7$ ) provides reassurance that the excess red color in that subsample was indeed due to host-galaxy light and that the blue QSOs are otherwise similar to the high redshift sample. The  $E(B - V)$  values obtained for the low-redshift QSOs for which we were able to subtract the host-galaxy from are shown in Table 1<sup>9</sup>. Overall, the removal of the host-galaxy results in a reddening estimate that is lower by a mean of -0.12 mag. Interestingly, our sample contains 31 sources in which removing

<sup>9</sup>Only a portion of this table is shown here to demonstrate its form and content. A machine-readable version of the full table is available upon request.

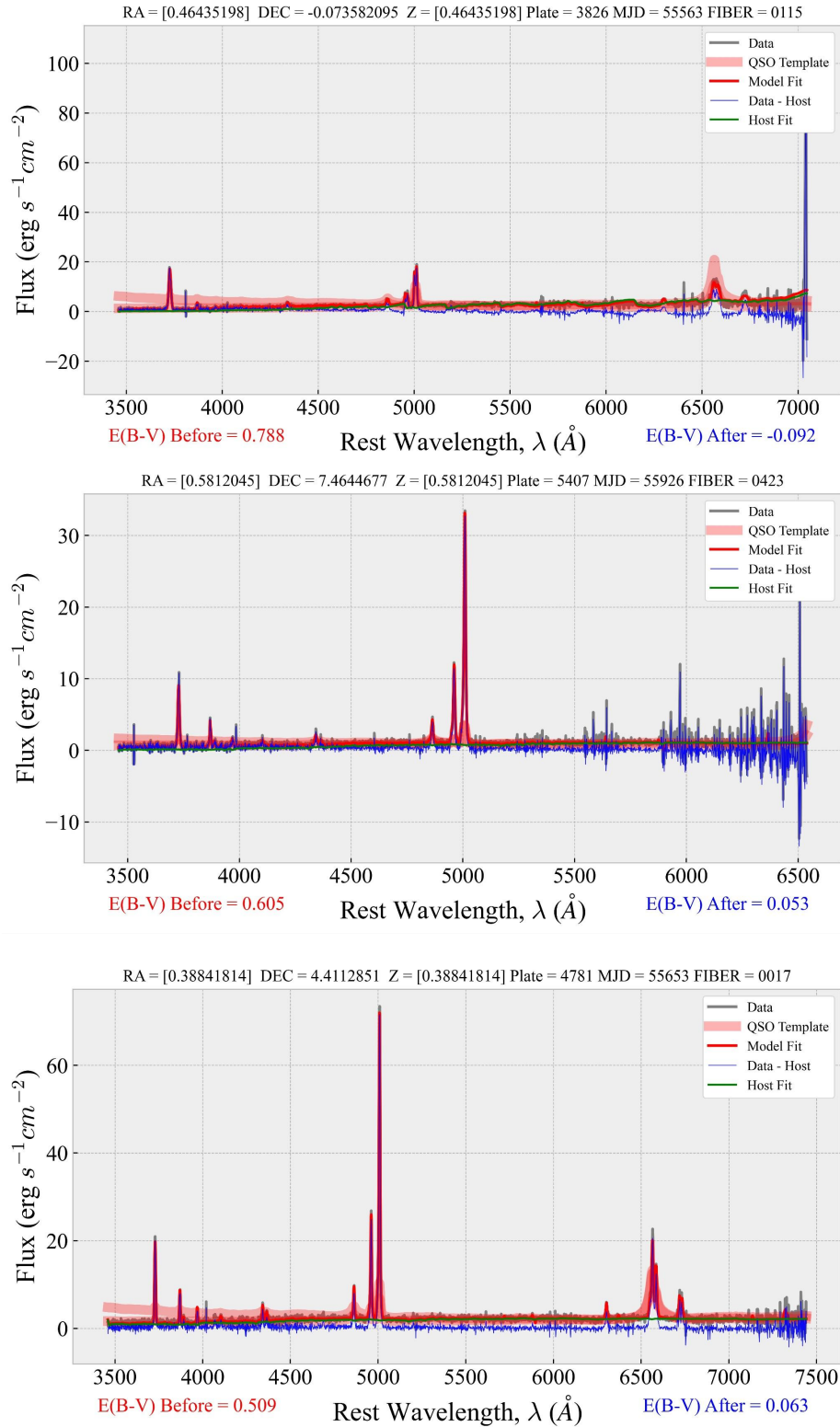


Figure 21: We follow Section 2.3 from Glikman et al. (2022) and subtract the host-galaxy’s fit (green) from the model fit (red) to remove the host-galaxy’s emission from the spectra. The red highlight is the best-fit QSO template from which  $E(B - V)$  is derived to both the SDSS data and the removed host-galaxy data fit. This leaves behind the sought-after unobscured blue QSO now that we have accounted for reddening.

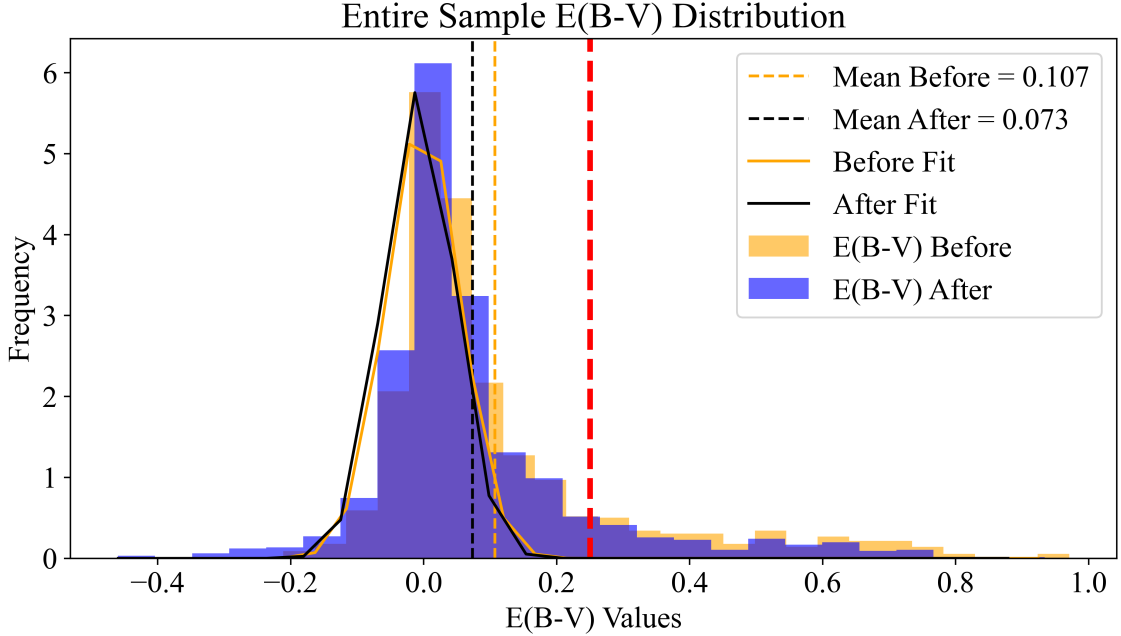


Figure 22: Distribution of the initial  $E(B - V)$  values for the SDSS QSOs, which we determined by fitting a QSO template to each spectrum are shown in the red for the entire sample. The vertical red dashed line at  $E(B - V) = 0.25$  is our defined limit for a QSO to be considered dust-reddened. As shown by the orange distribution and orange Gaussian curve fitted to the initial incorrect  $E(B - V)$  values for low redshift SDSS QSOs centered at  $E(B - V) = 0.26$  is then shifted to the blue centered at  $E(B - V) = 0.10$ .

the galaxy results in an unchanged AGN spectrum with moderate-to-high reddening ( $0.1 < E(B - V)$  “After”  $< 0.25$ ).

## 4.2 Red Quasars in the Blue Selected Sample

Red QSOs also exist among our sources with SDSS spectra and we wish to identify them and combine them with newly-identified red QSOs samples. After correcting for the host-galaxy, many our low redshift sample recover their blue colors, but 31% (98) of these sources have  $E(B - V)_{After} > 0.25$ , meeting our red QSO definition (shown in Figure 24).

Interestingly, there is an additional 3.6% (32) sources that are at high redshift ( $z > 0.7$ ) and have  $E(B - V) > 0.25$ , lying in the tail of the reddening distribution. We plot the  $E(B - V)$  values for sources as filled blue above the red line (at 0.25), thus defined as red quasars even after host-galaxy subtraction, in the histogram shown originally in Figure 19. Visual inspection of these spectra confirm their spectra are well fit by a QSO template, with an example SDSS spectrum shown in Figure 25.

To quantify the source of this reddening, we now investigate the quasars as a function of both luminosity and redshift in the following Section 5.

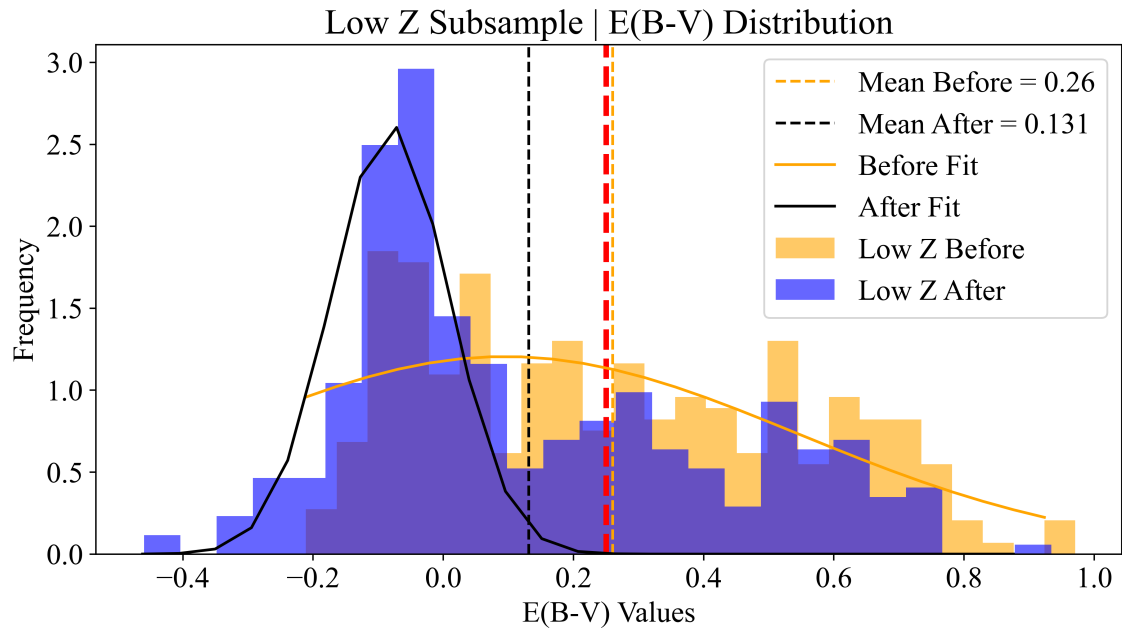


Figure 23: Distribution of the initial  $E(B - V)$  values for the SDSS QSOs, which we determined by fitting a QSO template to each spectrum are shown in the red for the entire sample. We further split the sample by high and low redshift. The distribution of initial  $E(B - V)$  values for high redshift SDSS QSOs is already centered on  $E(B - V) = 0$  shown in blue and fitted with a gray Gaussian curve. The vertical red dashed line at  $E(B - V) = 0.25$  is our defined limit for a QSO to be considered dust-reddened. As shown by the orange distribution and orange Gaussian curved fitted to the initial incorrect  $E(B - V)$  values for low redshift SDSS QSOs centered at  $E(B - V) = 0.26$  is then shifted to the blue centered at  $E(B - V) = 0.10$ .

## 5 Discussion: Red Quasars in the Context of Blue Quasars

### 5.1 Red and Blue Quasars as a Function of Luminosity

The host-galaxy subtraction (Section 4.1) allowed us to compute the reddening experienced by the QSOs without contamination from stellar light. We used the distribution of those reddenings (Figure 19) to define two samples: a sample of unobscured blue QSOs with  $E(B - V) < 0.25$  and a sample of reddened QSOs with  $E(B - V) > 0.25$ .

In Figure 26, we plot the  $(g - j)$  and  $(j - k)$  colors in AB magnitudes to compare the red and blue quasars in color space. We apply the following optical-to-near-infrared color cuts (in AB magnitudes),

$$J_{AB} - K_{AB} > 0.5 \text{ and } g_{AB} - J_{AB} > 2.0, \quad (29)$$

to the the total sample sources using their UKIDSS J and K magnitudes combined with their SDSS g magnitude, shown as the red dashed lines. These color cuts correspond to  $J_V - K_V > 1.462$  and  $g_{AB} - J_V > 2.938$ , which are in line with the cuts used by Urrutia et al. (2009) ( $J_V - K_V > 1.3$ ) and Glikman et al. (2012) ( $J_V - K_V > 1.5$ ). The red quasars are located in the upper right panel,

PlateMjdFiber	Z	RA	DEC	E(B-V) Before	E(B-V) After	$\Delta E(B-V)$
spec-3826-55563-0115	0.46435198	145.83016	-0.0735821	0.78778336	-0.0917823	-0.8795656
spec-0528-52022-0242	0.2170588	203.30178	1.5065855	0.31727555	-0.2923704	-0.609646
spec-4757-55653-0301	0.5956792	193.30953	3.595936	0.78053181	0.21978216	-0.5607497
spec-0573-52325-0143	0.3975244	152.12403	3.4197444	0.47920723	-0.0749615	-0.5541687
spec-5407-55926-0423	0.5812045	189.484	7.4644677	0.6051143	0.05301744	-0.5520969
spec-5318-55983-0153	0.6139008	146.56052	12.599819	0.72976709	0.18938437	-0.5403827
spec-0912-52427-0234	0.451109	203.97453	-2.4433708	0.39141435	-0.108852	-0.5002664
spec-0481-51908-0475	0.6052751	147.94945	2.0431794	0.02911605	-0.4597163	-0.4888323
spec-1193-52652-0554	0.6173753	138.92754	5.5340743	0.03716345	-0.4497828	-0.4869463
spec-4030-55634-0809	0.5825197	214.0801	2.2331432	0.75459093	0.28642739	-0.4681635
spec-0282-51658-0142	0.38586634	174.06285	-0.3873154	0.26159745	-0.190046	-0.4516434
spec-4781-55653-0017	0.38841814	217.88558	4.4112851	0.50850896	0.0632999	-0.4452091
spec-1815-53884-0196	0.49128503	225.0928	7.5170308	0.20760452	-0.2359934	-0.4435979
spec-1001-52670-0223	0.43509325	161.88268	6.6010304	0.36354209	-0.0798346	-0.4433767

Table 1: Fifteen low-redshift ( $z < 0.7$ ) QSOs for which we subtracted the host-galaxy’s light from the spectrum are shown in the Table. The name, redshift, RA, DEC, and E(B-V) Before and After values are shown in their respective columns. The change in E(B-V) values is given in the last column where the negative sign indicates that all of these QSOs E(B-V) values were unreddened and “blueshifted” towards the center at  $E(B - V) \sim 0.1$ . This is only a portion of the table. A full version containing all 1179 sources is available upon request.

indicating the identified reddened QSOs are indeed redder than the identified blue quasars. Our candidate blue sources appear to complete the cloud of points around  $g - J \simeq 2$  but also extend to very red tails in both  $g - J$  and  $J - K$ , which is expected as the same color distribution can be found in Figure 8 of Glikman et al. (2022). Though, the spread of red quasars outside of the filtration cuts used by Urrutia et al. (2009) and Glikman et al. (2012) gives reason to expand these color-selection method.

Although our use of WISE colors to select QSOs avoids the color bias experienced by optically selected QSO samples that miss most reddened QSOs, the imposition of the infrared  $K < 17$  mag limit still introduces a luminosity bias because, even at ( $2.2\mu m$ ), moderately reddened QSOs will be dimmed below the flux limit and therefore missed unless they are intrinsically more luminous. The bias has a strong redshift dependence because, at higher redshifts, ( $2.2\mu m$ ) represents rest-frame optical emission, which is more sensitive to the effects of dust-extinction. Therefore, to conduct a valid comparison between blue and red populations, we must compare objects with similar intrinsic absolute magnitude thresholds at all redshifts which would require a spectral energy distribution analysis that is outside the scope of this project.

## 5.2 Red and Blue Quasars as a Function of Redshift

We plot the absolute K-band magnitudes from UKIDSS for our sample in Figure 27, where the red QSOs are de-reddened and colored by their  $E(B - V)$  values versus redshift. Here, the luminosity bias becomes obvious with an absence of red QSOs near the flux limit especially toward increasing

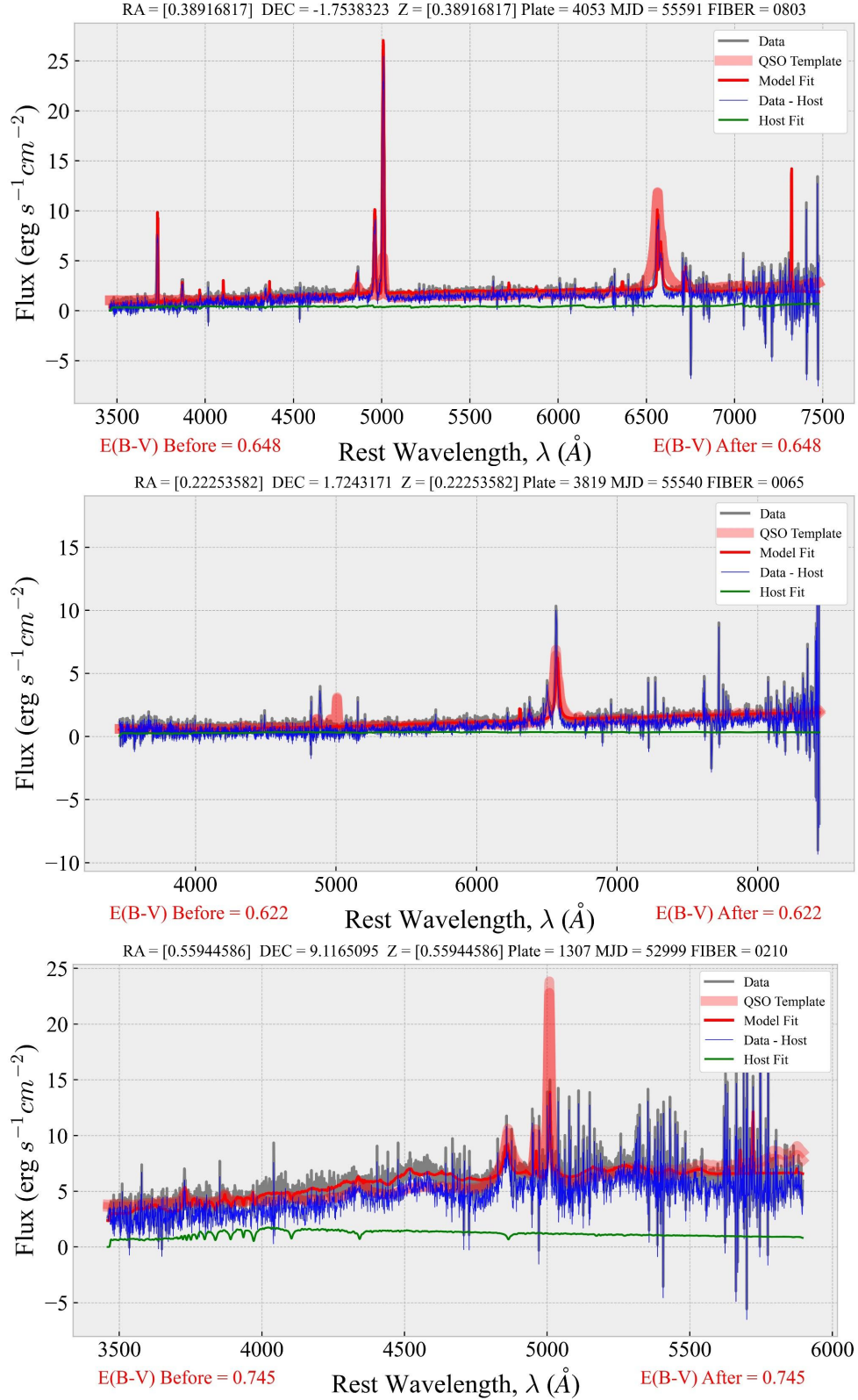


Figure 24: We follow Section 2.3 from Glikman et al. (2022) and subtract the host-galaxy’s fit (green) from the model fit (red) to remove the host-galaxy’s emission from the spectra. The high reddening does not change after the host is subtracted from the data—leaving the dust-reddened quasar. We add these sources to the reddened QSO sample to investigate in Section 5.

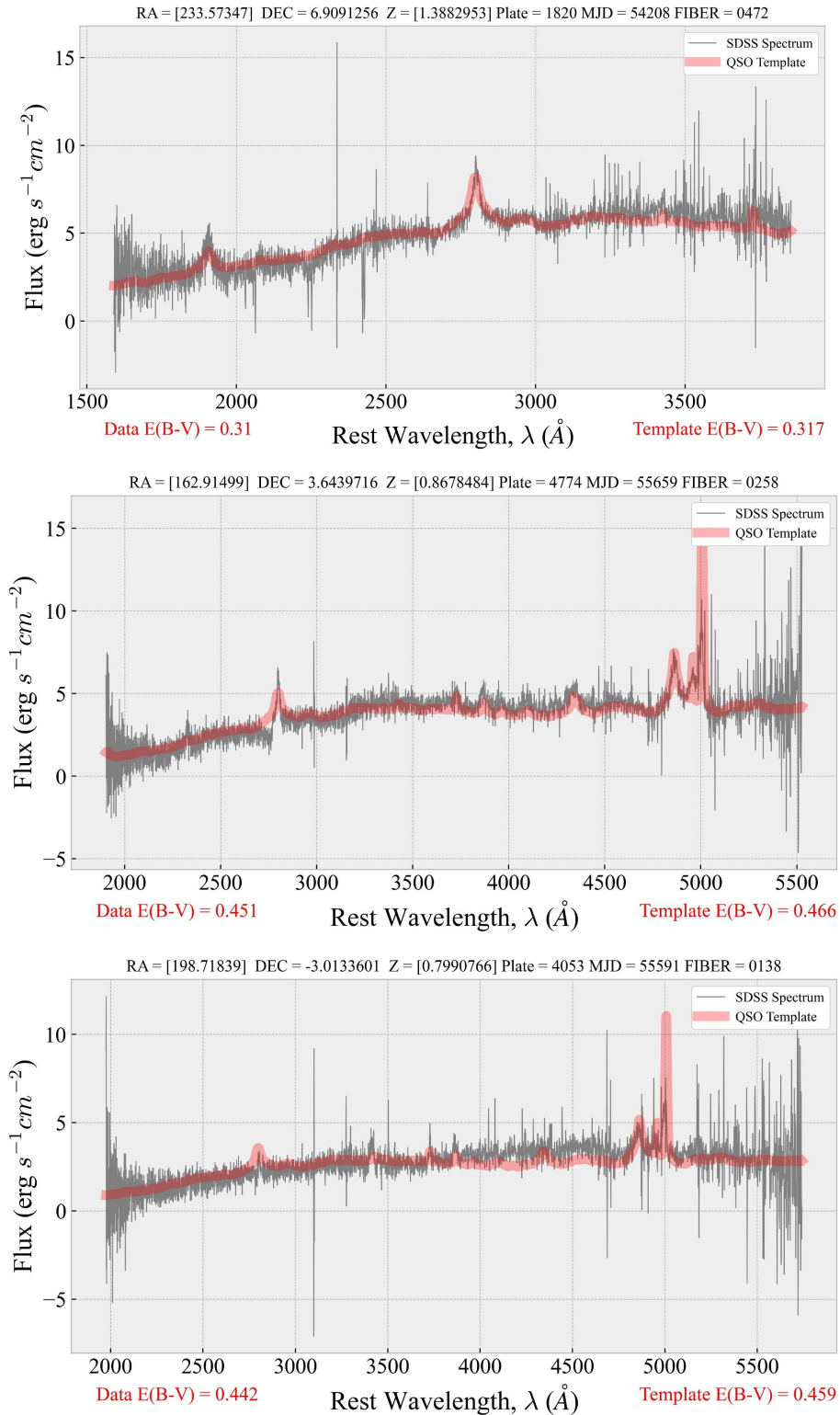


Figure 25: Example SDSS spectra of a high redshift ( $z > 0.7$ ) source with  $E(B - V) > 0.25$ , where the under each spectrum the  $E(B - V)$  value measured from the data is shown on the left in red and the  $E(B - V)$  value measured from the QSO template fit to the data is shown on the right in red. Since there is no galaxy subtraction, both values are inherently the same just cross-checked for sanity purposes.

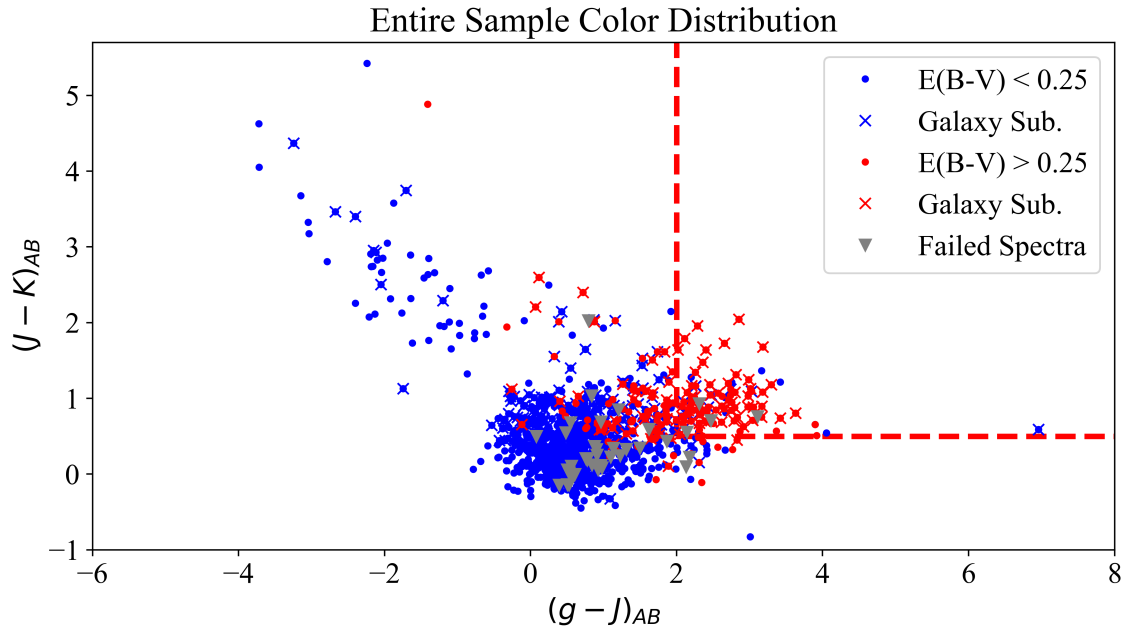


Figure 26: Our entire sample’s optical-to-near-infrared colors used in the KX selection method defined by Warren et al. (2000) and re- fined by Maddox et al. (2008). The blue circles represent all blue sources with  $E(B - V) < 0.25$ , while the red circles represent all reddened sources with  $E(B - V) > 0.25$ . The sources marked with an ‘x’ have had their host-galaxy subtracted from them. The gray triangle represent spectra that were not able to have their extinction value measured. The red dashed line is our color cut we impose in Equation 29 in this space to separate the red QSOs from the blue QSOs.

redshifts. In our sample, we see that at lower redshifts ( $z < 1.0$ ) the red and blue QSOs occupy similar luminosities, while at higher redshifts ( $z > 1.0$ ) there appear to be more high luminosity red QSOs compared with blue QSOs. This trend is well-explained by the fact that higher-redshift sources with even moderate amounts of reddening must be more luminous in order to pass the selection criteria. At lower redshifts, the effect of reddening is thus weaker and we identify heavily reddened sources with intrinsic luminosities consistent with their blue QSO counterparts. A similar analysis on the F2M red quasars in Glikman et al. (2007, 2012) revealed that they are more luminous than their unobscured counterparts, when corrected for extinction.

There is a scarcity of red QSOs at high redshifts ( $z > 1.0$ ). A similar observation was made in Glikman et al. (2018) for the pilot sample of luminous infrared selected red and blue QSOs in Stripe 82 where it was shown that Type 2 (narrow line) QSOs dominated the obscured QSO population at low redshifts, while the numbers of red QSOs increased at higher redshifts. This behavior is also seen in X-ray selected red QSOs, suggesting an evolutionary explanation (LaMassa et al. 2017).

The absence of large numbers of  $z > 1.0$  red QSOs may be a selection effect, as these will be lower luminosity AGN such that, when further reddened, will have their mid-infrared fluxes contaminated by host-galaxy light, potentially shifting them out of the selection criteria. Furthermore, as in

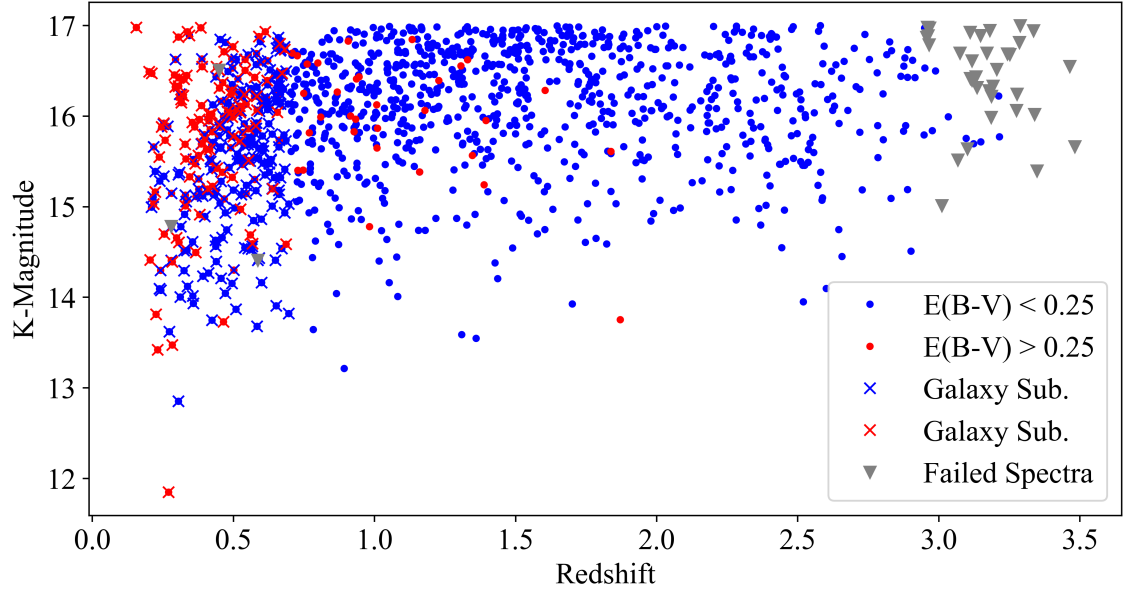


Figure 27: Our Type 1 sample’s redshift distribution against K-magnitude where 12 is brighter and 17 is fainter. The blue circles represent all blue sources with  $E(B - V) < 0.25$ , while the red circles represent all reddened sources with  $E(B - V) > 0.25$ . The sources marked with an ‘x’ have had their host-galaxy subtracted from them. The gray triangle represent spectra that were not able to have their extinction value measured. Red QSOs that have had their host-galaxy subtracted (red circles with an ‘x’) require further investigation.

Glikman et al. (2022) there is a dearth of red QSOs at low redshifts ( $z < 0.1$ ). However, in our sample there are also no blue selected sources at low redshift which does not allow a comparison below this limit. With this in mind, we also consider comparisons between red and blue QSOs restricted to high-redshifts ( $z > 1.0$ ), which amounts to 98% (N=673) blue sources and 2% (N=15) red sources.

Although the red QSO sample is otherwise predominantly low redshift ( $z < 1.0$ ), which may be largely due to the K-band flux limit imposed on our selection, higher-redshift red QSOs appear to be more represented among the red QSOs than in the blue population. This too could point to an evolutionary explanation.

The blue QSOs excluded by this process removes objects that would fall below the flux limit if reddened by  $E(B - V) = 0.25$ . However, the red QSO sample is still incomplete in ways that cannot be easily corrected without knowing the distribution of  $E(B - V)$  as a function of luminosity and redshift. The lower luminosity bins of the red QSO histogram are therefore incomplete and those sources can only be recovered with an even deeper survey still, or it can be explained that there exist no red QSOs beyond  $Z > 3.5$  which is unlikely further justifying an evolutionary scenario.

---

## 6 Initial Results and Further Investigations

In this thesis, we measured the characteristics of a radio, infrared, near-infrared, and optically selected sample of QSOs that serve as the comparison sample to a dust reddened type of these AGN found in the same area of sky. Through a complete spectroscopic analysis we are able to subtract the host-galaxy light from the low-redshift quasar spectra. We analyze the redshift and luminosity distribution for the dust reddening values ( $E(B - V)$ ) of our rigorously constructed sample. We find that from the total low redshift sample of AGN ( $z < 0.7$ ), removing the host-galaxy light from the spectra results in a spectrum with little reddening ( $E(B - V)_{After} < 0.25$ ) in 68% (N=211) of our sample and low-to-zero ( $E(B - V)_{After} < 0.1$ ) reddening in 58% (N=178) of our sample.

As noted in Section 5.2, at lower redshifts red QSOs are much more prevalent requiring host-galaxy subtraction from blue QSOs that may otherwise appear red. We identify heavily reddened sources with intrinsic luminosities consistent with their blue QSO counterparts. As such many of our low redshift sample recover their blue colors, but 32% (N=98) of these sources have  $E(B - V)_{After} > 0.25$ , meeting our red QSO definition, which require further investigation. However, there are few, 3.6% (N=31), sources that are at high redshift ( $z > 0.7$ ) and have  $E(B - V) > 0.25$ , lying in the tail of the reddening distribution.

There is a scarcity of red QSOs with SDSS spectra at high redshifts ( $z > 1.0$ ) that require a deeper survey still to study. With this in mind, we also consider comparisons between red and blue QSOs restricted to  $z > 1.0$ , which amounts to 98% (N=673) blue sources and 2% (N=15) red sources. This trend is well-explained by the fact that higher-redshift sources with even moderate amounts of reddening must be more luminous in order to pass the selection criteria. Although the red QSO sample is otherwise predominantly low redshift ( $z < 1.0$ ) at higher luminosity, higher-redshift red QSOs appear to be more represented among the red QSOs than in the blue lower-luminosity population. This too could point to an evolutionary explanation. In fact, Glikman et al. (2022) also finds that the incidence of red QSOs is strongly luminosity dependent, where red QSOs make up up to 40% of all QSOs at the highest luminosities.

The implications of the differences that could be seen in the radio properties of these red and blue QSOs requires a further study. Following Section 6 from Glikman et al. (2022) could potentially lead to a follow-up on the radio morphologies of our sources, since we require a FIRST detection in our studied sample. A major result from Klindt et al. (2019) was that when categorized by their FIRST morphology among FIRST-detected sources, a much larger fraction of red QSOs had a compact appearance compared to blue QSOs (7% vs 2% of the entire subsample, respectively) while

---

their fractions of extended sources are approximately the same. A similar finding was reported in Fawcett (2022). Additionally, in Glikman et al. (2022), they find that red QSOs have a significantly higher detection fraction and a higher fraction of compact radio morphologies at both frequencies. They also find that red QSOs have significantly brighter radio emission and steeper radio spectral slopes compared with blue QSOs.

If the difference between blue and red QSOs is not due to orientation with respect to our viewing angle, as is suggested by other studies radio results, then we can directly compare the two populations to find a true fraction of each sub group within the Type 1 QSO population (i.e., we can control for viewing angle, as illustrated in Figure 7, while exploring dust-reddening as the variable). With these assumptions, we can compute the fraction of red quasars to be,

$$\frac{N_{redQSO}}{N_{redQSO} + N_{blueQSO}} \quad (30)$$

However, as Figure ?? shows, the fraction of red QSOs appears to have a strong luminosity dependence which must be considered when determining a red QSO fraction. As mentioned previously, red QSOs make up a large percentage of all QSOs at high luminosities. On the lower luminosity end blue QSOs tend to dominate, with some outliers. These identified red sources had their host-galaxy subtracted, with no change in their reddening, requiring the previously mentioned radio-study follow-up. We recommend this project to a fellow student to pick-up either as a semester or summer project.

However, Glikman et al. (2022) depicts a strong luminosity effect, showing that red QSOs dominate the overall QSO populations regardless of radio properties. Their radio detected red QSO fraction is higher at decreasing luminosities, which may be explain the outliers of red QSOs in our sample at low luminosity. However, in both cases, red QSOs make up at least 20% and up to 40% of the overall QSO population at the highest luminosities. We find by equation 30 the low redshift sample after host-galaxy subtraction we find the fraction of red quasars, while noting the luminosity and redshift dependence, to be:  $(98)/(211 + 98)$  or 32%.

We note that these fractions are consistent with the fraction of red quasars estimated in Glikman et al. (2012) for the F2M sample, which extends to fainter magnitudes ( $K < 15.5$  mag, the 2MASS limit). Figure 17 of that paper shows that red quasars dominate at the highest de-reddened absolute K-band magnitudes of a similar range. LaMassa et al. (2017) sees similar behavior for X-ray-selected red QSOs, finding that red QSOs make up a larger fraction of all X-ray-selected QSOs when corrected for absorption. In Glikman et al. (2018), the red QSO sample identified over Stripe 82 is combined with a shallower, mid-infrared red QSO surveys conducted over smaller

---

areas to enable a luminosity function calculation and the comparison of red QSO space density versus blue and Type 2 QSOs (which are more heavily obscured, likely due to orientation). That study, as well as Glikman et al. (2022), finds that red QSOs make up  $\sim 20 - 40\%$  of the overall QSO population at the highest luminosities, which this work further corroborates.

---

## 7 Acknowledgments

This project would not be possible without the support, mentoring, and wisdom of my advisor, Professor Eilat Glikman at Middlebury College, who has introduced the shine of quasars to my career and study. Without her continuous encouragement this project would not be the work that it is today. I look forward to continuing this work post-graduation to peer further into the dusty quasar realm.

I would like to thank my on-campus advisor, Professor Karen Masters at Haverford College, for the support and guidance throughout my undergraduate education. From galaxies to black holes, my passion for studying the Universe has only grown under her teachings and enlightenment. I would also like to recognize Karen's instruction in the Strawbridge Observatory that has been imperative to my studies of the night sky.

Thank you to my peers in the Physics and Astronomy Department at Haverford College for the camaraderie over the past years and especially throughout the writing process of this thesis.

This project makes use of data products from the Wide-field Infrared Survey Explorer, which is a joint project of the University of California, Los Angeles, and the Jet Propulsion Laboratory/California Institute of Technology, funded by the National Aeronautics and Space Administration.

The UKIDSS project is defined in Lawrence et al. (2007). The photometric system is described in Hopkins et al. (2006), and the calibration is described in Hodgkin et al. (2009). The pipeline processing and science archive are described in Hambly et al. (2008).

Funding for SDSS-III has been provided by the Alfred P. Sloan Foundation, the Participating Institutions, the National Science Foundation, and the U.S. Department of Energy Office of Science. The SDSS-III website is <http://www.sdss3.org/>.

SDSS-III is managed by the Astrophysical Research Consortium for the Participating Institutions of the SDSS-III Collaboration including the University of Arizona, the Brazilian Participation Group, Brookhaven National Laboratory, Carnegie Mellon University, University of Florida, the French Participation Group, the German Participation Group, Harvard University, the Instituto de Astrofísica de Canarias, the Michigan State/Notre Dame/JINA Participation Group, Johns Hopkins University, Lawrence Berkeley National Laboratory, Max Planck Institute for Astrophysics, Max Planck Institute for Extraterrestrial Physics, New Mexico State University, New York University, Ohio State University, Pennsylvania State University, University of Portsmouth, Princeton University, the Spanish Participation Group, University of Tokyo, University of Utah, Vanderbilt

---

University, University of Virginia, University of Washington, and Yale University.

## **8 Facilities**

Sloan, Palomar, IRTF, APO, LBT, Lick, VLA

---

## A Matching in SDSS

The query selects from Sky Archive Server (SAS) the SDSS DR18 spectroscopic catalog all sources with Plate-Mjd-FiberID that match the uploaded list of RA/Dec. From this initial search, we download 1134 spectra files. We match the 1134 spectra to the (Glikman et al. 2022) parent sample containing 1463 objects. Of the 1463 parent sample, 1423 sources are valid (hereon “parent sample”). From the 289 failed spectra downloads, we rerun the initial search through the SAS to find 133 spectra within 2 arcseconds search radius. We match these objects to the parent sample via RA/Dec within 2 arcseconds and redshift within 0.001 error. Thus we add the 133 sources to the 1134 matches to find a total of 1267. We continue this method of searching for sources via the SAS to find an additional 53 sources within a 2 arcseconds search radius and 0.001 redshift error to find a total of 1320 sources. From here, we have a list of 159 missing sources to investigate. From my previous matching attempts, we found 106 missing sources and of those, we were able to hand download 85 spectra based either on the Spectra Object ID or the Object ID. Not surprisingly, though reassuringly, 83 of the 106 missing sources matched to the list of 159 missing sources. We verified these sources by the same RA/Dec and redshift parameters as above to find a total of 1403 total sources (the downloaded spectra sample referenced throughout this work).

## B BADASS: Computationally Expensive

The fitting procedure failed to run on the Haverford Jupyter Hub server, and thus we continue with fitting the sources on a local Jupyter Notebook session. The program is computationally expensive; each source takes anywhere between 5 minutes up to 7 hours, at most, to fit on both a local computer server and on the Haverford Jupyter Hub. For these reasons, we do not attempt to run the fitting procedure on moderate-high redshifts as their spectral lines will be redshifted beyond  $H\alpha$  causing the code to break.

## C K-Band Magnitude vs absolute $22\mu\text{m}$ (W4) Magnitude

We include the absolute K-band magnitude from WISE versus absolute 22m (W4) magnitude from UKIDSS for the QSO sample in Figure 28. The unreddened QSOs are shown with blue circles, with the QSOs that had host-galaxy subtraction overplotted with ‘x’s. The red circles are the red QSOs and they lie along the same relation as all the other QSOs, providing further assurance that the reddening analysis of our sample is reliable. A direct relationship is seen across the luminosity

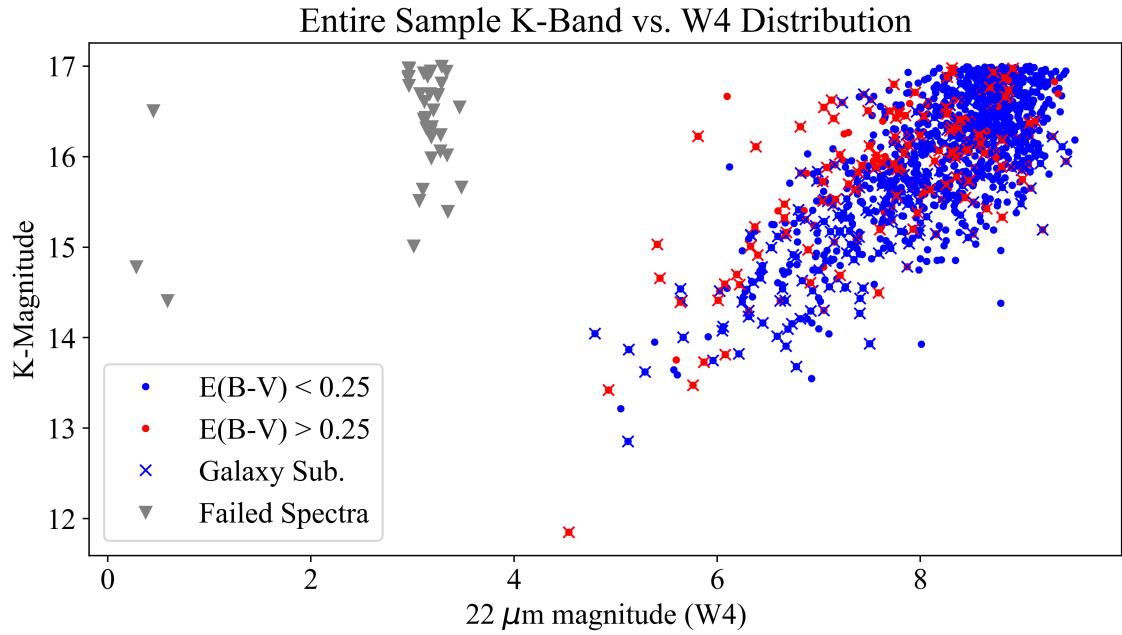


Figure 28: The absolute K-band magnitude from WISE versus absolute 22m (W4) magnitude from UKIDSS for the QSO sample. The blue circles represent the blue QSOs found in our sample, the red circles represent the reddened QSOs found in our sample, the ‘x’s mark sources which have had their host-galaxy subtracted, and the grey triangles represent sources that which the Extinction code failed on. A direct relationship is seen across the luminosity range, except at the highest luminosities where the K-band magnitudes are slightly enhanced compared with W4. Interestingly, the failed spectra are entirely offset from the rest of the sample.

range, except at the highest luminosities where the K-band magnitudes are slightly enhanced compared with W4. The blue QSOs appear to dominate this region at the highest luminosities. The spread of red QSOs at fainter magnitudes  $K < 17$  gives justification to fainter surveys than those that have been previously used in order to improve the hunt for these elusive objects.

---

## References

- Abazajian, Kevork et al. (Oct. 2003). ‘The First Data Release of the Sloan Digital Sky Survey’. In: 126.4, pp. 2081–2086. DOI: 10.1086/378165. arXiv: astro-ph/0305492 [astro-ph].
- Abazajian, Kevork et al. (July 2004). ‘The Second Data Release of the Sloan Digital Sky Survey’. In: 128.1, pp. 502–512. DOI: 10.1086/421365. arXiv: astro-ph/0403325 [astro-ph].
- Abazajian, Kevork et al. (Mar. 2005). ‘The Third Data Release of the Sloan Digital Sky Survey’. In: 129.3, pp. 1755–1759. DOI: 10.1086/427544. arXiv: astro-ph/0410239 [astro-ph].
- Abazajian, Kevork N. et al. (June 2009). ‘The Seventh Data Release of the Sloan Digital Sky Survey’. In: 182.2, pp. 543–558. DOI: 10.1088/0067-0049/182/2/543. arXiv: 0812.0649 [astro-ph].
- Abbott, B. P. et al. (2016). ‘Observation of Gravitational Waves from a Binary Black Hole Merger’. In: *Phys. Rev. Lett.* 116 (6), p. 061102. DOI: 10.1103/PhysRevLett.116.061102. URL: <https://link.aps.org/doi/10.1103/PhysRevLett.116.061102>.
- Abramowicz, Marek A. and P. Chris Fragile (Jan. 2013). ‘Foundations of Black Hole Accretion Disk Theory’. In: *Living Reviews in Relativity* 16.1, 1, p. 1. DOI: 10.12942/lrr-2013-1. arXiv: 1104.5499 [astro-ph.HE].
- Adelman-McCarthy, Jennifer K. et al. (Jan. 2006). ‘The Fourth Data Release of the Sloan Digital Sky Survey’. In: 162.1, pp. 38–48. DOI: 10.1086/497917. arXiv: astro-ph/0507711 [astro-ph].
- Adelman-McCarthy, Jennifer K. et al. (Oct. 2007). ‘The Fifth Data Release of the Sloan Digital Sky Survey’. In: 172.2, pp. 634–644. DOI: 10.1086/518864. arXiv: 0707.3380 [astro-ph].
- Adelman-McCarthy, Jennifer K. et al. (Apr. 2008). ‘The Sixth Data Release of the Sloan Digital Sky Survey’. In: 175.2, pp. 297–313. DOI: 10.1086/524984. arXiv: 0707.3413 [astro-ph].
- Aird, J. et al. (Feb. 2010). ‘The evolution of the hard X-ray luminosity function of AGN’. In: 401.4, pp. 2531–2551. DOI: 10.1111/j.1365-2966.2009.15829.x. arXiv: 0910.1141 [astro-ph.CO].
- Almeida, Andrés et al. (Jan. 2023). ‘The Eighteenth Data Release of the Sloan Digital Sky Surveys: Targeting and First Spectra from SDSS-V’. In: *arXiv e-prints*, arXiv:2301.07688, arXiv:2301.07688. DOI: 10.48550/arXiv.2301.07688. arXiv: 2301.07688 [astro-ph.GA].
- Assef, R. J. et al. (July 2013). ‘Mid-infrared Selection of Active Galactic Nuclei with the Wide-field Infrared Survey Explorer. II. Properties of WISE-selected Active Galactic Nuclei in the NDWFS Boötes Field’. In: 772.1, 26, p. 26. DOI: 10.1088/0004-637X/772/1/26. arXiv: 1209.6055 [astro-ph.CO].
- Assef, R. J. et al. (Feb. 2018). ‘The WISE AGN Catalog’. In: 234.2, 23, p. 23. DOI: 10.3847/1538-4365/aaa00a. arXiv: 1706.09901 [astro-ph.GA].
- Becker, Robert H., Richard L. White and David J. Helfand (Sept. 1995). ‘The FIRST Survey: Faint Images of the Radio Sky at Twenty Centimeters’. In: 450, p. 559. DOI: 10.1086/176166.

- 
- Bolton, Adam S. et al. (Nov. 2012). ‘Spectral Classification and Redshift Measurement for the SDSS-III Baryon Oscillation Spectroscopic Survey’. In: 144.5, 144, p. 144. DOI: 10.1088/0004-6256/144/5/144. arXiv: 1207.7326 [astro-ph.CO].
- Bondi, H. and F. Hoyle (Jan. 1944). ‘On the mechanism of accretion by stars’. In: 104, p. 273. DOI: 10.1093/mnras/104.5.273.
- Boyle, B. J., T. Shanks and B. A. Peterson (Dec. 1988). ‘The evolution of optically selected QSOs - II.’ In: 235, pp. 935–948. DOI: 10.1093/mnras/235.3.935.
- Calderone, G. et al. (Dec. 2017). ‘QSFIT: automatic analysis of optical AGN spectra’. In: 472.4, pp. 4051–4080. DOI: 10.1093/mnras/stx2239. arXiv: 1612.01580 [astro-ph.HE].
- Cappellari, Michele (Apr. 2017). ‘Improving the full spectrum fitting method: accurate convolution with Gauss-Hermite functions’. In: 466.1, pp. 798–811. DOI: 10.1093/mnras/stw3020. arXiv: 1607.08538 [astro-ph.GA].
- Council, National Research (2000). *Federal Funding of Astronomical Research*. Washington, DC: The National Academies Press. ISBN: 978-0-309-07139-0. DOI: 10.17226/9954. URL: <https://nap.nationalacademies.org/catalog/9954/federal-funding-of-astronomical-research>.
- Croom, S. et al. (Oct. 2004). ‘The 2DF QSO Redshift Survey’. In: *Multiwavelength AGN Surveys*. Ed. by Raúl Mújica and Roberto Maiolino, pp. 57–62. DOI: 10.1142/9789812702432\_0015.
- Cutri, R. M. et al. (Feb. 2021). ‘VizieR Online Data Catalog: AllWISE Data Release (Cutri+ 2013)’. In: *VizieR Online Data Catalog*, II/328, pp. II/328.
- Delvecchio, I. et al. (Apr. 2014). ‘Tracing the cosmic growth of supermassive black holes to  $z \sim 3$  with Herschel’. In: 439.3, pp. 2736–2754. DOI: 10.1093/mnras/stu130. arXiv: 1401.4503 [astro-ph.GA].
- Donley, J. L. et al. (Apr. 2012). ‘Identifying Luminous Active Galactic Nuclei in Deep Surveys: Revised IRAC Selection Criteria’. In: 748.2, 142, p. 142. DOI: 10.1088/0004-637X/748/2/142. arXiv: 1201.3899 [astro-ph.CO].
- Dreyer, J. L. E. (Jan. 1888). ‘A New General Catalogue of Nebulæ and Clusters of Stars, being the Catalogue of the late Sir John F. W. Herschel, Bart, revised, corrected, and enlarged’. In: 49, p. 1.
- Einstein, A. (1905). ‘Does the Inertia of a Body Depend on Its Energy Content?’ In: 17, p. 891. DOI: 10.21203/rs.3.rs-426760/v1.
- Einstein, Albert (1905). ‘On the Electrodynamics of Moving Bodies’. In: *The Principle of Relativity*. Dover Publications, pp. 35–65.
- Einstein, Albert (Jan. 1915). ‘Die Feldgleichungen der Gravitation’. In: *Sitzungsberichte der Königlich Preussischen Akademie der Wissenschaften*, pp. 844–847.
-

- 
- Event Horizon Telescope Collaboration et al. (Apr. 2019). ‘First M87 Event Horizon Telescope Results. I. The Shadow of the Supermassive Black Hole’. In: 875.1, L1, p. L1. DOI: 10.3847/2041-8213/ab0ec7. arXiv: 1906.11238 [astro-ph.GA].
- Fabian, A. C. (Sept. 2012). ‘Observational Evidence of Active Galactic Nuclei Feedback’. In: 50, pp. 455–489. DOI: 10.1146/annurev-astro-081811-125521. arXiv: 1204.4114 [astro-ph.CO].
- Fan, Xiaohui et al. (Apr. 2003). ‘A Survey of  $z_{i}5.7$  Quasars in the Sloan Digital Sky Survey. II. Discovery of Three Additional Quasars at  $z_{i}6$ ’. In: 125.4, pp. 1649–1659. DOI: 10.1086/368246. arXiv: astro-ph/0301135 [astro-ph].
- Fath, E. A. (June 1909). ‘The Spectra of Some Spiral Nebulæ and Globular Star Clusters’. In: 21.126, pp. 138–143. DOI: 10.1086/121907.
- Fawcett, Victoria (Sept. 2022). ‘How are red and blue quasars different?’ In: *Hypatia Colloquium 2022*, 38, p. 38. DOI: 10.5281/zenodo.7104579.
- Ferrarese, Laura and David Merritt (Aug. 2000). ‘A Fundamental Relation between Supermassive Black Holes and Their Host Galaxies’. In: 539.1, pp. L9–L12. DOI: 10.1086/312838. arXiv: astro-ph/0006053 [astro-ph].
- Fitzpatrick, Edward L. (Jan. 1999). ‘Correcting for the Effects of Interstellar Extinction’. In: 111.755, pp. 63–75. DOI: 10.1086/316293. arXiv: astro-ph/9809387 [astro-ph].
- Foreman-Mackey, Daniel et al. (Mar. 2013). ‘emcee: The MCMC Hammer’. In: 125.925, p. 306. DOI: 10.1086/670067. arXiv: 1202.3665 [astro-ph.IM].
- Frieman, Joshua A. et al. (Jan. 2008). ‘The Sloan Digital Sky Survey-II Supernova Survey: Technical Summary’. In: 135.1, pp. 338–347. DOI: 10.1088/0004-6256/135/1/338. arXiv: 0708.2749 [astro-ph].
- Frogel, Jay A (2010). ‘Astronomy’s Greatest Hits: The 100 Most Cited Papers in Each Year of the First Decade of the 21st Century (2000–2009)’. In: *Publications of the Astronomical Society of the Pacific* 122.896, p. 1214. DOI: 10.1086/656515. URL: <https://dx.doi.org/10.1086/656515>.
- Garcia, Michael R. et al. (2001). ‘New Evidence for Black Hole Event Horizons from Chandra’. In: *The Astrophysical Journal* 553.1, p. L47. DOI: 10.1086/320494. URL: <https://dx.doi.org/10.1086/320494>.
- Gebhardt, Karl et al. (Aug. 2000). ‘A Relationship between Nuclear Black Hole Mass and Galaxy Velocity Dispersion’. In: 539.1, pp. L13–L16. DOI: 10.1086/312840. arXiv: astro-ph/0006289 [astro-ph].
- Gillette, Jarred, Marie Wingyee Lau and Frederick Hamann (Jan. 2023). ‘Characterizing Extremely Red Quasars and Quasar Outflows Using Rest-UV Spectroscopy’. In: *American Astronomical Society Meeting Abstracts*. Vol. 55. American Astronomical Society Meeting Abstracts, 138.01, p. 138.01.

- 
- Glikman, E. et al. (July 2018). ‘Luminous WISE-selected Obscured, Unobscured, and Red Quasars in Stripe 82’. In: 861.1, 37, p. 37. DOI: 10.3847/1538-4357/aac5d8. arXiv: 1805.06961 [astro-ph.GA].
- Glikman, E. et al. (Aug. 2022). ‘The WISE-2MASS Survey: Red Quasars Into the Radio Quiet Regime’. In: 934.2, 119, p. 119. DOI: 10.3847/1538-4357/ac6bee. arXiv: 2204.13745 [astro-ph.GA].
- Glikman, Eilat (2020). ‘EG NSF Project Description’. In.
- Glikman, Eilat et al. (May 2004). ‘FIRST-2Mass Sources below the APM Detection Threshold: A Population of Highly Reddened Quasars’. In: 607.1, pp. 60–75. DOI: 10.1086/383305. arXiv: astro-ph/0402386 [astro-ph].
- Glikman, Eilat et al. (Oct. 2007). ‘The FIRST-2MASS Red Quasar Survey’. In: 667.2, pp. 673–703. DOI: 10.1086/521073. arXiv: 0706.3222 [astro-ph].
- Glikman, Eilat et al. (Sept. 2012). ‘FIRST-2MASS Red Quasars: Transitional Objects Emerging from the Dust’. In: 757.1, 51, p. 51. DOI: 10.1088/0004-637X/757/1/51. arXiv: 1207.2175 [astro-ph.CO].
- Glikman, Eilat et al. (Dec. 2013). ‘Dust Reddened Quasars in FIRST and UKIDSS: Beyond the Tip of the Iceberg’. In: 778.2, 127, p. 127. DOI: 10.1088/0004-637X/778/2/127. arXiv: 1309.6626 [astro-ph.CO].
- Glikman, Eilat et al. (June 2015). ‘Major Mergers Host the Most-luminous Red Quasars at  $z \sim 2$ : A Hubble Space Telescope WFC3/IR Study’. In: 806.2, 218, p. 218. DOI: 10.1088/0004-637X/806/2/218. arXiv: 1504.02111 [astro-ph.GA].
- Goldschmidt, Pippa et al. (1999). ‘A Comparison of the Optical Properties of Radio-loud and Radio-quiet Quasars’. In: *The Astrophysical Journal* 511, pp. 612–624.
- Greenstein, Jesse L. and Maarten Schmidt (July 1964). ‘The Quasi-Stellar Radio Sources 3C 48 and 3C 273.’ In: 140, p. 1. DOI: 10.1086/147889.
- Gregg, Michael D. et al. (Aug. 1996). ‘The First Bright QSO Survey’. In: 112, p. 407. DOI: 10.1086/118024. arXiv: astro-ph/9604148 [astro-ph].
- Guo, Hengxiao, Yue Shen and Shu Wang (Sept. 2018). *PyQSOFit: Python code to fit the spectrum of quasars*. Astrophysics Source Code Library, record ascl:1809.008. ascl: 1809.008.
- Hamann, Fred et al. (Jan. 2017). ‘Extremely red quasars in BOSS’. In: 464.3, pp. 3431–3463. DOI: 10.1093/mnras/stw2387. arXiv: 1609.07241 [astro-ph.GA].
- Hambly, N. C. et al. (Feb. 2008). ‘The WFCAM Science Archive’. In: 384.2, pp. 637–662. DOI: 10.1111/j.1365-2966.2007.12700.x. arXiv: 0711.3593 [astro-ph].
- Hayward, Sean A (1998). ‘Unified first law of black-hole dynamics and relativistic thermodynamics’. In: *Classical and Quantum Gravity* 15.10, p. 3147. DOI: 10.1088/0264-9381/15/10/017. URL: <https://dx.doi.org/10.1088/0264-9381/15/10/017>.
-

- 
- Hewett, Paul C. and Vivienne Wild (July 2010). ‘Improved redshifts for SDSS quasar spectra’. In: 405.4, pp. 2302–2316. DOI: 10.1111/j.1365-2966.2010.16648.x. arXiv: 1003.3017 [astro-ph.CO].
- Hodgkin, S. T. et al. (Apr. 2009). ‘The UKIRT wide field camera ZYJHK photometric system: calibration from 2MASS’. In: 394.2, pp. 675–692. DOI: 10.1111/j.1365-2966.2008.14387.x. arXiv: 0812.3081 [astro-ph].
- Hopkins, Philip F. et al. (Sept. 2005). ‘Black Holes in Galaxy Mergers: Evolution of Quasars’. In: 630.2, pp. 705–715. DOI: 10.1086/432438. arXiv: astro-ph/0504190 [astro-ph].
- Hopkins, Philip F. et al. (Mar. 2006). ‘A Unified, Merger-driven Model of the Origin of Starbursts, Quasars, the Cosmic X-Ray Background, Supermassive Black Holes, and Galaxy Spheroids’. In: 163.1, pp. 1–49. DOI: 10.1086/499298. arXiv: astro-ph/0506398 [astro-ph].
- Hoyle, F. and W. A. Fowler (Jan. 1963). ‘On the nature of strong radio sources’. In: 125, p. 169. DOI: 10.1093/mnras/125.2.169.
- Hubber, David and Giovanni Rosotti (Feb. 2016). *GANDALF: Graphical Astrophysics code for N-body Dynamics And Lagrangian Fluids*. Astrophysics Source Code Library, record ascl:1602.015. ascl: 1602.015.
- Hubble, E. P. (May 1925). ‘Cepheids in spiral nebulae’. In: *The Observatory* 48, pp. 139–142.
- Hubble, Edwin (Mar. 1929). ‘A Relation between Distance and Radial Velocity among Extra-Galactic Nebulae’. In: *Proceedings of the National Academy of Science* 15.3, pp. 168–173. DOI: 10.1073/pnas.15.3.168.
- Irwin, Mike, Richard G. McMahon and Cyril Hazard (Jan. 1991). ‘APM optical surveys for high redshift quasars.’ In: *The Space Distribution of Quasars*. Ed. by David Crampton. Vol. 21. Astronomical Society of the Pacific Conference Series, pp. 117–126.
- Jarrett, T. H. et al. (July 2011). ‘The Spitzer-WISE Survey of the Ecliptic Poles’. In: 735.2, 112, p. 112. DOI: 10.1088/0004-637X/735/2/112.
- Karhunen, K. et al. (June 2014). ‘Low-redshift quasars in the SDSS Stripe 82. The local environments’. In: 441.2, pp. 1802–1816. DOI: 10.1093/mnras/stu688. arXiv: 1404.1642 [astro-ph.GA].
- Kellermann, K. I., I. I. K. Pauliny-Toth and P. J. S. Williams (July 1969). ‘The Spectra of Radio Sources in the Revised 3c Catalogue’. In: 157, p. 1. DOI: 10.1086/150046.
- Kellermann, K. I. et al. (Nov. 2016). ‘Radio-loud and Radio-quiet QSOs’. In: 831.2, 168, p. 168. DOI: 10.3847/0004-637X/831/2/168. arXiv: 1608.04586 [astro-ph.GA].
- Kessler, Richard et al. (Nov. 2009). ‘First-Year Sloan Digital Sky Survey-II Supernova Results: Hubble Diagram and Cosmological Parameters’. In: 185.1, pp. 32–84. DOI: 10.1088/0067-0049/185/1/32. arXiv: 0908.4274 [astro-ph.CO].
- Kim, Dohyeong et al. (Oct. 2015). ‘Accretion Rates of Red Quasars from the Hydrogen P $\beta$  Line’. In: 812.1, 66, p. 66. DOI: 10.1088/0004-637X/812/1/66. arXiv: 1510.03887 [astro-ph.GA].
-

- 
- Klawitter, Jack (2023). *Quasar\_unred : A Python Package for Quasar Reddening Correction*. [https://github.com/jackklawitter/quasar\\_unred](https://github.com/jackklawitter/quasar_unred). Accessed: April 22, 2023.
- Klindt, L. et al. (Sept. 2019). ‘Fundamental differences in the radio properties of red and blue quasars: evolution strongly favoured over orientation’. In: 488.3, pp. 3109–3128. DOI: 10.1093/mnras/stz1771. arXiv: 1905.12108 [astro-ph.GA].
- Loizides, Fernando and Birgit Schmidt, eds. (2016). *Jupyter Notebooks ? a publishing format for reproducible computational workflows*. IOS Press, pp. 87–90. URL: <https://eprints.soton.ac.uk/403913/>.
- Kormendy, John and Luis C. Ho (Aug. 2013). ‘Coevolution (Or Not) of Supermassive Black Holes and Host Galaxies’. In: 51.1, pp. 511–653. DOI: 10.1146/annurev-astro-082708-101811. arXiv: 1304.7762 [astro-ph.CO].
- Kormendy, John and Douglas Richstone (Jan. 1995). ‘Inward Bound—The Search For Supermassive Black Holes In Galactic Nuclei’. In: 33, p. 581. DOI: 10.1146/annurev.aa.33.090195.003053.
- Kovačević, Jelena, Luka Č. Popović and Milan S. Dimitrijević (Jan. 2010). ‘The optical Fe II emission lines in Active Galactic Nuclei’. In: *Memorie della Societa Astronomica Italiana Supplementi* 15, p. 176.
- Lacy, M. et al. (Nov. 2005). ‘The Infrared Array Camera Component of the Spitzer Space Telescope Extragalactic First Look Survey’. In: 161.1, pp. 41–52. DOI: 10.1086/432894. arXiv: astro-ph/0507143 [astro-ph].
- LaMassa, Stephanie M., Tahir Yaqoob and Roy Kilgard (May 2017). ‘Insight into “Changing-look” AGN Mrk 1018 from the Fe K $\alpha$  Line: The Reprocessing Gas Has Yet to Fully Respond to the Fading of the AGN’. In: 840.1, 11, p. 11. DOI: 10.3847/1538-4357/aa68df. arXiv: 1703.07410 [astro-ph.HE].
- Lawrence, A. et al. (Aug. 2007). ‘The UKIRT Infrared Deep Sky Survey (UKIDSS)’. In: 379.4, pp. 1599–1617. DOI: 10.1111/j.1365-2966.2007.12040.x. arXiv: astro-ph/0604426 [astro-ph].
- Leavitt, Henrietta S. and Edward C. Pickering (Mar. 1912). ‘Periods of 25 Variable Stars in the Small Magellanic Cloud.’ In: *Harvard College Observatory Circular* 173, pp. 1–3.
- Lister, M. L. et al. (Feb. 2003). ‘4C +12.50: A Superluminal Precessing Jet in the Recent Merger System IRAS 13451+1232’. In: 584.1, pp. 135–146. DOI: 10.1086/345666. arXiv: astro-ph/0210372 [astro-ph].
- Lupton, Robert et al. (Feb. 2004). ‘Preparing Red-Green-Blue Images from CCD Data’. In: 116.816, pp. 133–137. DOI: 10.1086/382245. arXiv: astro-ph/0312483 [astro-ph].
- Madau, Piero (2014). *Cosmic Star-Formation History*. URL: <https://ned.ipac.caltech.edu/level5/March14/Madau/Madau5.html> (visited on 25th Apr. 2023).
-

- 
- Madau, Piero and Mark Dickinson (Aug. 2014). ‘Cosmic Star-Formation History’. In: 52, pp. 415–486. DOI: 10.1146/annurev-astro-081811-125615. arXiv: 1403.0007 [astro-ph.CO].
- Maddox, Natasha et al. (2008). ‘Luminous K-band selected quasars from UKIDSS’. In: *Monthly Notices of the Royal Astronomical Society* 386.3, pp. 1605–1624. ISSN: 0035-8711. DOI: 10.1111/j.1365-2966.2008.13138.x. eprint: [https://academic.oup.com/mnras/article-pdf/386/3/1605/40636267/mnras\\_386\\_3\\_1605.pdf](https://academic.oup.com/mnras/article-pdf/386/3/1605/40636267/mnras_386_3_1605.pdf). URL: <https://doi.org/10.1111/j.1365-2966.2008.13138.x>.
- Magorrian, John et al. (June 1998). ‘The Demography of Massive Dark Objects in Galaxy Centers’. In: 115.6, pp. 2285–2305. DOI: 10.1086/300353. arXiv: astro-ph/9708072 [astro-ph].
- Marconi, Alessandro and Leslie K. Hunt (May 2003). ‘The Relation between Black Hole Mass, Bulge Mass, and Near-Infrared Luminosity’. In: 589.1, pp. L21–L24. DOI: 10.1086/375804. arXiv: astro-ph/0304274 [astro-ph].
- Masci, F. J., R. L. Webster and P. J. Francis (Dec. 1998). ‘Host galaxy contribution to the colours of ‘red’ quasars’. In: 301.4, pp. 975–984. DOI: 10.1046/j.1365-8711.1998.02088.x. arXiv: astro-ph/9808337 [astro-ph].
- Masters, Karen L. (Mar. 2013). ‘A Zoo of Galaxies’. In: *arXiv e-prints*, arXiv:1303.7118, arXiv:1303.7118. DOI: 10.48550/arXiv.1303.7118. arXiv: 1303.7118 [astro-ph.CO].
- Mateos, S. et al. (Nov. 2012). ‘Using the Bright Ultrahard XMM-Newton survey to define an IR selection of luminous AGN based on WISE colours’. In: 426.4, pp. 3271–3281. DOI: 10.1111/j.1365-2966.2012.21843.x. arXiv: 1208.2530 [astro-ph.CO].
- McLure, R. J. and J. S. Dunlop (Apr. 2002). ‘On the black hole-bulge mass relation in active and inactive galaxies’. In: 331.3, pp. 795–804. DOI: 10.1046/j.1365-8711.2002.05236.x. arXiv: astro-ph/0108417 [astro-ph].
- Meyer, Martin J. et al. (June 2001). ‘Quasars from a complete spectroscopic survey’. In: 324.2, pp. 343–354. DOI: 10.1046/j.1365-8711.2001.04265.x.
- Mullaney, J. R. et al. (July 2013). ‘Narrow-line region gas kinematics of 24 264 optically selected AGN: the radio connection’. In: 433.1, pp. 622–638. DOI: 10.1093/mnras/stt751. arXiv: 1305.0263 [astro-ph.CO].
- Pâris, Isabelle et al. (Jan. 2017). ‘The Sloan Digital Sky Survey Quasar Catalog: Twelfth data release’. In: 597, A79, A79. DOI: 10.1051/0004-6361/201527999. arXiv: 1608.06483 [astro-ph.GA].
- Pasetto, Alice et al. (2021). ‘Reading M87’s DNA: A Double Helix Revealing a Large-scale Helical Magnetic Field’. In: *The Astrophysical Journal Letters* 923.1, p. L5. DOI: 10.3847/2041-8213/ac3a88. URL: <https://dx.doi.org/10.3847/2041-8213/ac3a88>.
- Perucho, M. et al. (Apr. 2012). ‘Anatomy of Helical Extragalactic Jets: The Case of S5 0836+710’. In: 749.1, 55, p. 55. DOI: 10.1088/0004-637X/749/1/55. arXiv: 1202.1182 [astro-ph.CO].
-

- 
- Pettini, M. (Oct. 2011). ‘The First Stars: clues from quasar absorption systems’. In: *Proceedings of the Royal Society of London Series A* 467.2134, pp. 2735–2751. DOI: 10.1098/rspa.2011.0117.
- Reines, Amy E. and Marta Volonteri (Nov. 2015). ‘Relations between Central Black Hole Mass and Total Galaxy Stellar Mass in the Local Universe’. In: 813.2, 82, p. 82. DOI: 10.1088/0004-637X/813/2/82. arXiv: 1508.06274 [astro-ph.GA].
- Rhoads, James E. (Aug. 2001). ‘Snapshot Identification of Gamma-Ray Burst Optical Afterglows’. In: 557.2, pp. 943–948. DOI: 10.1086/321664. arXiv: astro-ph/0008461 [astro-ph].
- Richards, Gordon T. et al. (June 2002). ‘Spectroscopic Target Selection in the Sloan Digital Sky Survey: The Quasar Sample’. In: 123.6, pp. 2945–2975. DOI: 10.1086/340187. arXiv: astro-ph/0202251 [astro-ph].
- Richards, Gordon T. et al. (Sept. 2003). ‘Red and Reddened Quasars in the Sloan Digital Sky Survey’. In: 126.3, pp. 1131–1147. DOI: 10.1086/377014. arXiv: astro-ph/0305305 [astro-ph].
- Richards, Gordon T. et al. (Oct. 2006). ‘Spectral Energy Distributions and Multiwavelength Selection of Type 1 Quasars’. In: 166.2, pp. 470–497. DOI: 10.1086/506525. arXiv: astro-ph/0601558 [astro-ph].
- Rigby, Jane et al. (July 2022). ‘The Science Performance of JWST as Characterized in Commissioning’. In: *arXiv e-prints*, arXiv:2207.05632, arXiv:2207.05632. arXiv: 2207.05632 [astro-ph.IM].
- Ross, Nicholas P. et al. (Nov. 2015). ‘Extremely red quasars from SDSS, BOSS and WISE: classification of optical spectra’. In: 453.4, pp. 3932–3952. DOI: 10.1093/mnras/stv1710. arXiv: 1405.1047 [astro-ph.GA].
- Ryden, Barbara and Bradley M. Peterson (2020). *Foundations of Astrophysics*. Cambridge University Press. DOI: 10.1017/9781108933001.
- Safronov, V. S. (1972). *Evolution of the protoplanetary cloud and formation of the earth and planets*.
- Sanders, D. B. et al. (Feb. 1988). ‘Ultraluminous Infrared Galaxies and the Origin of Quasars’. In: 325, p. 74. DOI: 10.1086/165983.
- Sarzi, Marc et al. (Mar. 2006). ‘The SAURON project - V. Integral-field emission-line kinematics of 48 elliptical and lenticular galaxies’. In: 366.4, pp. 1151–1200. DOI: 10.1111/j.1365-2966.2005.09839.x. arXiv: astro-ph/0511307 [astro-ph].
- Sarzi, Marc et al. (Aug. 2017). *GANDALF: Gas AND Absorption Line Fitting*. Astrophysics Source Code Library, record ascl:1708.012. ascl: 1708.012.
- Schawinski, Kevin et al. (Dec. 2007). ‘Observational evidence for AGN feedback in early-type galaxies’. In: 382.4, pp. 1415–1431. DOI: 10.1111/j.1365-2966.2007.12487.x. arXiv: 0709.3015 [astro-ph].
- Schmidt, M. (Mar. 1963). ‘3C 273 : A Star-Like Object with Large Red-Shift’. In: 197.1040, p. 2. DOI: <https://doi.org/10.1038/1971040a0>.
-

- 
- Schmidt, Maarten and Thomas A. Matthews (Feb. 1964). ‘Redshift of the Quasi-Stellar Radio Sources 3c 47 and 3c 147.’ In: 139, p. 781. DOI: 10.1086/147815.
- Schmidt, O. and A. Lebedinsky (2001). *A Theory of Earth’s Origin: Four Lectures*. University Press of the Pacific. ISBN: 9780898754247. URL: <https://books.google.com/books?id=E1Ast8BJQl8C>.
- Schneider, Donald P. et al. (Dec. 2003). ‘The Sloan Digital Sky Survey Quasar Catalog. II. First Data Release’. In: 126.6, pp. 2579–2593. DOI: 10.1086/379174. arXiv: astro-ph/0308443 [astro-ph].
- Serjeant, Stephen (Jan. 1996). ‘Hidden quasars reddened by dust?’ In: 379.6563, p. 304. DOI: 10.1038/379304a0.
- Serjeant, Stephen et al. (Mar. 1998). ‘The radio-optical correlation in steep-spectrum quasars’. In: 294.3, pp. 494–504. DOI: 10.1046/j.1365-8711.1998.01303.x. arXiv: astro-ph/9710106 [astro-ph].
- Seth, Anil et al. (2009). ‘Employment and Funding in Astronomy’. In:
- Sexton, Remington (2021). *Bayesian AGN Decomposition Analysis for SDSS Spectra*. <https://github.com/remingtonsexton/BADASS3>. Accessed: 4th May 2023.
- Sexton, Remington et al. (Jan. 2023). ‘The Newest Version of Bayesian AGN Decomposition Analysis for SDSS Spectra (BADASS)’. In: *American Astronomical Society Meeting Abstracts*. Vol. 55. American Astronomical Society Meeting Abstracts, 105.25, p. 105.25.
- Sexton, Remington O et al. (2020). ‘Bayesian AGN Decomposition Analysis for SDSS spectra: a correlation analysis of [O III] 5007 outflow kinematics with AGN and host galaxy properties’. In: *Monthly Notices of the Royal Astronomical Society* 500.3, pp. 2871–2895. DOI: 10.1093/mnras/staa3278. URL: <https://doi.org/10.1093/mnras/staa3278>.
- Sexton, Remington O. et al. (Jan. 2021). ‘Bayesian AGN Decomposition Analysis for SDSS spectra: a correlation analysis of [O III]  $\lambda$ 5007 outflow kinematics with AGN and host galaxy properties’. In: 500.3, pp. 2871–2895. DOI: 10.1093/mnras/staa3278. arXiv: 2010.09748 [astro-ph.GA].
- Seyfert, Carl K. (Jan. 1943). ‘Nuclear Emission in Spiral Nebulae.’ In: 97, p. 28. DOI: 10.1086/144488.
- Shankar, Francesco, David H. Weinberg and Jordi Miralda-Escudé (Jan. 2009). ‘Self-Consistent Models of the AGN and Black Hole Populations: Duty Cycles, Accretion Rates, and the Mean Radiative Efficiency’. In: 690.1, pp. 20–41. DOI: 10.1088/0004-637X/690/1/20. arXiv: 0710.4488 [astro-ph].
- Shen, Yue and Brandon C. Kelly (Feb. 2012). ‘The Demographics of Broad-line Quasars in the Mass-Luminosity Plane. I. Testing FWHM-based Virial Black Hole Masses’. In: 746.2, 169, p. 169. DOI: 10.1088/0004-637X/746/2/169. arXiv: 1107.4372 [astro-ph.CO].

- 
- Silk, Joseph and Martin J. Rees (Mar. 1998). ‘Quasars and galaxy formation’. In: 331, pp. L1–L4. arXiv: astro-ph/9801013 [astro-ph].
- Simmons, B. D. et al. (June 2011). ‘Obscured GOODS Active Galactic Nuclei and Their Host Galaxies at  $z \lesssim 1.25$ : The Slow Black Hole Growth Phase’. In: 734.2, 121, p. 121. DOI: 10.1088/0004-637X/734/2/121. arXiv: 1104.2619 [astro-ph.CO].
- Simmons, Brooke D. et al. (Mar. 2013). ‘Galaxy Zoo: bulgeless galaxies with growing black holes’. In: 429.3, pp. 2199–2211. DOI: 10.1093/mnras/sts491. arXiv: 1207.4190 [astro-ph.CO].
- Skrutskie, M. F. et al. (Feb. 2006). ‘The Two Micron All Sky Survey (2MASS)’. In: 131.2, pp. 1163–1183. DOI: 10.1086/498708.
- Slipher, V. M. (Jan. 1913). ‘The radial velocity of the Andromeda Nebula’. In: *Lowell Observatory Bulletin* 2.8, pp. 56–57.
- Smethurst, R. J. et al. (Nov. 2022). ‘Evidence for non-merger co-evolution of galaxies and their supermassive black holes’. In: *arXiv e-prints*, arXiv:2211.13677, arXiv:2211.13677. arXiv: 2211.13677 [astro-ph.GA].
- Soltan, A. (July 1982). ‘Masses of quasars.’ In: 200, pp. 115–122. DOI: 10.1093/mnras/200.1.115.
- Stern, Daniel et al. (Sept. 2005). ‘Mid-Infrared Selection of Active Galaxies’. In: 631.1, pp. 163–168. DOI: 10.1086/432523. arXiv: astro-ph/0410523 [astro-ph].
- Stern, Daniel et al. (July 2012). ‘Mid-infrared Selection of Active Galactic Nuclei with the Wide-Field Infrared Survey Explorer. I. Characterizing WISE-selected Active Galactic Nuclei in COSMOS’. In: 753.1, 30, p. 30. DOI: 10.1088/0004-637X/753/1/30. arXiv: 1205.0811 [astro-ph.CO].
- Stoughton, Chris et al. (Jan. 2002). ‘Sloan Digital Sky Survey: Early Data Release’. In: 123.1, pp. 485–548. DOI: 10.1086/324741.
- Tremaine, Scott et al. (Aug. 2002). ‘The Slope of the Black Hole Mass versus Velocity Dispersion Correlation’. In: 574.2, pp. 740–753. DOI: 10.1086/341002. arXiv: astro-ph/0203468 [astro-ph].
- Trumpler, Robert J. (Mar. 1940). ‘Galactic Star Clusters.’ In: 91, p. 186. DOI: 10.1086/144156.
- Urrutia, Tanya, Mark Lacy and Robert H. Becker (Feb. 2008). ‘Evidence for Quasar Activity Triggered by Galaxy Mergers in HST Observations of Dust-reddened Quasars’. In: 674.1, pp. 80–96. DOI: 10.1086/523959. arXiv: 0709.2805 [astro-ph].
- Urrutia, Tanya et al. (June 2009). ‘The FIRST-2MASS Red Quasar Survey. II. An Anomalously High Fraction of LoBALs in Searches for Dust-Reddened Quasars’. In: 698.2, pp. 1095–1109. DOI: 10.1088/0004-637X/698/2/1095. arXiv: 0808.3668 [astro-ph].
- Urrutia, Tanya et al. (Oct. 2012). ‘Spitzer Observations of Young Red Quasars’. In: 757.2, 125, p. 125. DOI: 10.1088/0004-637X/757/2/125. arXiv: 1208.4585 [astro-ph.CO].
-

- 
- Urry, C. Megan and Paolo Padovani (Sept. 1995). ‘Unified Schemes for Radio-Loud Active Galactic Nuclei’. In: 107, p. 803. DOI: 10.1086/133630. arXiv: astro-ph/9506063 [astro-ph].
- Valdes, Francisco et al. (June 2004). ‘The Indo-US Library of Coudé Feed Stellar Spectra’. In: 152.2, pp. 251–259. DOI: 10.1086/386343. arXiv: astro-ph/0402435 [astro-ph].
- Venemans, B. P. et al. (Mar. 2007). ‘The discovery of the first luminous  $z \sim 6$  quasar in the UKIDSS Large Area Survey’. In: 376.1, pp. L76–L80. DOI: 10.1111/j.1745-3933.2007.00290.x. arXiv: astro-ph/0612162 [astro-ph].
- Véron-Cetty, M. P., M. Joly and P. Véron (Apr. 2004). ‘The unusual emission line spectrum of I Zw 1’. In: 417, pp. 515–525. DOI: 10.1051/0004-6361:20035714. arXiv: astro-ph/0312654 [astro-ph].
- Vestergaard, M. and B. J. Wilkes (May 2001). ‘An Empirical Ultraviolet Template for Iron Emission in Quasars as Derived from I Zwicky 1’. In: 134.1, pp. 1–33. DOI: 10.1086/320357. arXiv: astro-ph/0104320 [astro-ph].
- Warren, S. J., P. C. Hewett and C. B. Foltz (Mar. 2000). ‘The KX method for producing K-band flux-limited samples of quasars’. In: 312.4, pp. 827–832. DOI: 10.1046/j.1365-8711.2000.03206.x. arXiv: astro-ph/9911064 [astro-ph].
- Weaver, Harold and Paul Weaver (Aug. 1957). ‘Robert Julius Trumpler, 1886-1956’. In: 69.409, p. 304. DOI: 10.1086/127076.
- Webster, Rachel L. et al. (June 1995). ‘Evidence for a large undetected population of dust-reddened quasars’. In: 375.6531, pp. 469–471. DOI: 10.1038/375469a0.
- Whiting, M. T., R. L. Webster and P. J. Francis (May 2001). ‘Red synchrotron jets in Parkes quasars’. In: 323.3, pp. 718–732. DOI: 10.1046/j.1365-8711.2001.04287.x. arXiv: astro-ph/0101502 [astro-ph].
- Willott, Chris J. et al. (2010). ‘EDDINGTON-LIMITED ACCRETION AND THE BLACK HOLE MASS FUNCTION AT REDSHIFT 6’. In: *The Astronomical Journal* 140.2, p. 546. DOI: 10.1088/0004-6256/140/2/546. URL: <https://dx.doi.org/10.1088/0004-6256/140/2/546>.
- Wright, Edward L. et al. (Dec. 2010). ‘The Wide-field Infrared Survey Explorer (WISE): Mission Description and Initial On-orbit Performance’. In: 140.6, pp. 1868–1881. DOI: 10.1088/0004-6256/140/6/1868. arXiv: 1008.0031 [astro-ph.IM].
- Wu, Q., H. Yu and F. Y. Wang (May 2020). ‘A New Method to Measure Hubble Parameter  $H(z)$  Using Fast Radio Bursts’. In: 895.1, 33, p. 33. DOI: 10.3847/1538-4357/ab88d2. arXiv: 2004.12649 [astro-ph.CO].
- Yanny, Brian et al. (May 2009). ‘SEGUE: A Spectroscopic Survey of 240,000 Stars with  $g = 14-20$ ’. In: 137.5, pp. 4377–4399. DOI: 10.1088/0004-6256/137/5/4377. arXiv: 0902.1781 [astro-ph.GA].

- 
- Yi, Weimin et al. (May 2022). ‘A Quasar Shedding Its Dust Cocoon at Redshift 2’. In: 930.1, 5, p. 5. DOI: 10.3847/1538-4357/ac6109. arXiv: 2203.07570 [astro-ph.GA].
- York, Donald G. et al. (Sept. 2000). ‘The Sloan Digital Sky Survey: Technical Summary’. In: 120.3, pp. 1579–1587. DOI: 10.1086/301513. arXiv: astro-ph/0006396 [astro-ph].
- Yu, Qingjuan and Scott Tremaine (Oct. 2002). ‘Observational constraints on growth of massive black holes’. In: *Monthly Notices of the Royal Astronomical Society* 335.4, pp. 965–976. ISSN: 0035-8711. DOI: 10.1046/j.1365-8711.2002.05532.x. eprint: <https://academic.oup.com/mnras/article-pdf/335/4/965/2867327/335-4-965.pdf>. URL: <https://doi.org/10.1046/j.1365-8711.2002.05532.x>.
- Zhang, Tong-Jie, Cong Ma and Tian Lan (Jan. 2010). ‘Constraints on the Dark Side of the Universe and Observational Hubble Parameter Data’. In: *Advances in Astronomy* 2010, 184284, p. 184284. DOI: 10.1155/2010/184284. arXiv: 1010.1307 [astro-ph.CO].